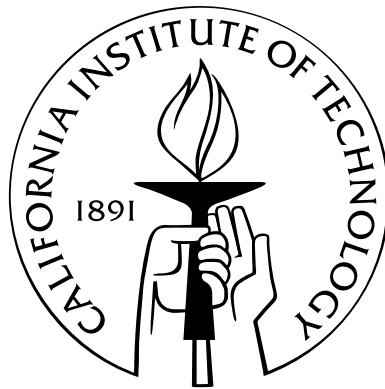# PHOTON CONFINEMENT IN PHOTONIC CRYSTAL CAVITIES

Thesis by

Uday Kiran Khankhoje

In Partial Fulfillment of the Requirements

for the Degree of

Doctor of Philosophy

California Institute of Technology

Pasadena, California

2010

(Defended May 19, 2010)

This thesis is dedicated to the memory of my grandfather Narayan "Nana" Khankhoje.

*04.17.1923 - 09.09.2009*

# Acknowledgements

Graduate school has by far been the most enriching experience of my life. I am humbled when I think of all the wonderful people whose lives have touched mine in some way or the other, making this experience possible, enjoyable, and satisfying.

I owe the deepest gratitude to my advisor, Professor Axel Scherer, for guiding me through my thesis work. His patience, unconditional support, and generosity formed a scaffolding on which I could go wherever my curiosity took me. In addition to Axel, I was fortunate enough to have had Professors Hyatt Gibbs and Galina Khitrova[1] as my "unofficial" advisors. With the constant encouragement that I received from the three of them, I learned a tremendous lot, traveled to many conferences, and broadened my scientific horizon.

My introduction to the mind-expanding world of science was largely due to three very inspiring teachers at my undergraduate school[2]: Professor Vikram Gadre introduced me to the joy of research at a very early stage; Professor Gopal Srinivasan's love for mathematics was deeply inspiring and infectious; and Professor R. Shevgaonkar revealed the beautiful theory of electrodynamics, encouraging me to go deeper into the subject in graduate school. And what greater privilege could there have been, but to have taken further courses in electrodynamics from Professor Amnon Yariv himself! Interacting with him over the last few years has truly been a stimulating experience.

I would also like to thank my thesis committee members, Professors Amnon Yariv, Changhuei Yang, Jakob van Zyl, and Dr. Se-Heon Kim, for their graciousness in serving on the committee and for their overall guidance.

The lab environment in the Scherer group has been very genial and collaborative. I am grateful to all my officemates who have tolerated and kept me in good humor over these past years: Sven, Mike, Dave, Se-Heon, and Zhenyu. Along with them, it has been great fun to work with some of the other group members: Andrew, Sameer, Aditya, Joyce, and Jingqing. Jingqing, who has been a great sounding board and friend all along, went through various versions of the thesis very patiently and diligently, and her insightful comments greatly contributed to its evolution. It has been a fruitful experience to interact with Se-Heon, a person whose breadth and depth of knowledge about photonic crystals is enormous; from helping me with device simulations, to fixing a vacuum system (where

---

[1] Both at the Optical Sciences Center, University of Arizona (UA), Tucson.
[2] Indian Institute of Technology, Bombay.

# Abstract

In this thesis, the use of photonic crystal cavities for experiments in cavity quantum-electrodynamics is described. To this end, the propagation of light in photonic crystals, and the creation of cavities by making defects in the photonic crystal lattice, is discussed. By drawing an analogy with Fabry-Perot etalons, the mechanism of light confinement in these cavities is explained. It is shown that by engineering the immediate cavity neighborhood, the mirror reflectivities can be increased, resulting in a very high quality factor ($Q$) and low mode volume. Photonic crystal cavity designs used in this thesis are introduced, along with numerically computed data of their performance.

Device fabrication in gallium arsenide wafers is described in detail, with special attention to address factors that lead to a lack of reproducibility. Over the course of this thesis effort, several thousand cavities were fabricated, and a wide range of $Q$s were recorded. Careful experiments were performed to determine the causes of low $Q$s, both at the wafer growth level, and at the fabrication level. Technological improvements in wafer growth are reported, as well as fabrication techniques to improve cavity $Q$.

These cavities contain indium arsenide quantum dots (QDs) as internal light sources. Cavity-induced enhancement of QD light emission is discussed, along with interferometric measurements of photon correlations. It is found that light emission from coupled QD-cavity systems is highly non-classical, and this quantum nature is characterized by means of a second order correlation function.

To conclude, a novel application of high-$Q$ cavities is discussed, that of an electrically-pumped laser fabricated in a 1D nanobeam cavity. The salient feature of such a geometry is that a high $Q$ is retained even with the introduction of gold in the cavity vicinity. Finally, approaches to improve cavity $Q$ by material system optimizations are explored. In the first approach, QD growth in III-V material systems with light emission wavelengths in the telecommunications wavelength range ($\lambda \approx 1.55\,\mu\text{m}$) is discussed, and in the second, the growth of III-V-based active media in silicon structures is considered.

# Contents

# List of Figures

# List of Tables

# Chapter 1

# Light in a Cavity

From the very early days of quantum mechanics, physicists have tried to understand the properties of atomic spectral lines. Albert Einstein's seminal work in 1916–17 formalized a quantum theory of radiation and proposed three basic generators of spectral lines - spontaneous emission, stimulated emission, and photo-absorption, each of which was phenomenologically described with an appropriate probability of the event's occurrence[1].

Spontaneous emission refers to the phenomenon of emission of a photon by an atom in an excited state making a transition to its ground state. The word "spontaneous" came from the initial observation that the transition would happen without any external influence. The notion of "external" influence got substantially revised with the full quantum treatment of particles *and* fields. This physics came to be formally studied in the field of quantum-electrodynamics (QED), which, along with being a template for other field theories, is to date one of the most precise physical theories worked out by humankind[2].

It was soon recognized that the rate of spontaneous emission from an atom was greatly dependent on the electromagnetic environment. Naturally, it became interesting and important to consider structures with controllable electromagnetic environments such as resonators. A well designed resonator can trap light for substantial periods of time, and thus allows the study of interactions between trapped light and matter (corresponding to different atomic states). Light emitted by an atom in a resonator faces a drastically different electromagnetic environment compared to free space, which has a continuum of electromagnetic states. Further, the electromagnetic environment (i.e., the density of optical states) in a resonator can be modified by altering the cavity geometry, making it possible to create light-matter coupled states that might be otherwise hard or impossible to find in nature.

It is beyond the scope of this thesis to present the full formalism and theory of cavity QED

---

[1]Later called the "Einstein coefficients."

[2]Figures often quoted in support of this argument pertain to very precise measurements of the anomalous magnetic dipole moments, hyperfine splitting, and the Lamb shift in hydrogen, among others, that are matched spectacularly by QED predictions [1].

(cQED), and there are many elegant, scholarly works that the readers can refer to for this purpose [2, 3, 4, 5]. In order to explain the physics behind experimentally observed data, some of the relevant aspects of cQED are presented without derivation in this chapter. Practical implementations and related issues are also sketched.

## 1.1 Spontaneous Emission

To understand and calculate the rate at which spontaneous emission happens requires a careful consideration of the interaction between the atom (treated as a two-level system) and the (quantized) electromagnetic fields in which the atom finds itself.

For the sake of simplicity, it is first assumed that the electromagnetic environment is composed of a single mode[3]. A useful tensor-product notation for a atom-field state is of the form $|s, n\rangle$, where $s$ is the state of the atom (either excited $s_e$ or ground $s_g$), and $n$ is the number of photons in the electromagnetic mode. The interaction energy between an atom and a single electromagnetic mode is equal to the dot product of the atomic dipole moment and the electric field at the atom's position. This, along with the energy of the field and atom, allows the total atom-field Hamiltonian to be written down, as was first done in the Jaynes-Cummings [6] model. Most physical situations justify the use of the rotating wave approximation in the solution of this Hamiltonian. It is found that the atom-field interaction leads to a coupling between states of the form $|s_e, n\rangle$ and $|s_g, n+1\rangle$, and that the energy eigenvectors of the coupled system are superpositions of these states. The atomic levels are said to have been "dressed" by the electromagnetic field. The time evolution of the system is worked out using Schrödinger's equation, revealing that the atom flops between the excited and ground states with the characteristic "Rabi" frequency, $R_0 = -2g\sqrt{n+1}$, where $g$ is the atomic-dipole matrix element. An interesting observation at this point is that in the full quantum treatment described here, an initially excited atom "Rabi-flops" even if there are no photons in the cavity. This is because while the expectation value of the vacuum electric field vanishes, the expectation value of the field intensity does not, and in effect, vacuum fluctuations cause the atom to spontaneously emit[4].

Now, instead of a single electromagnetic mode, the coupling between an atom and a number of modes can be considered. By applying Fermi's Golden Rule, the probability of transition to a single mode can be computed, and by summing over these probabilities for multiple modes, it is found that the rate of spontaneous emission $\Gamma$ is proportional to the optical density of states, $D(\omega)$, as $\Gamma = 2\pi g^2(\omega)D(\omega)$. The story in the case of free space is slightly different, since a continuum of modes is available for the atom to couple to. The situation is now considerably complicated, since

---

[3]A simple analogy to understand a single mode is to think of an air pipe that is blown "gently" into so as to excite only a single frequency.

[4]This behavior is not predicted by semi-classical theory.

the coupling between the atom and a large number of states must be considered, and, as noted earlier, the interaction energy for each mode depends on the orientation of the atomic dipole with the field polarization. The Weisskopf-Wigner theory takes these factors into account and an elegant expression for the spontaneous emission rate in free space is obtained [3],

$$\Gamma = \frac{1}{4\pi\epsilon_0} \frac{4\omega^3 |\mu|^2}{3c^3\hbar} \tag{1.1}$$

where $\omega$ and $\mu$ are the atomic transition frequency and dipole moment, respectively. It must be noted that the Weisskopf-Wigner theory predicts an irreversible exponential decay of the excited state of the atom, and is valid in the presence of a continuum of electromagnetic modes.

## 1.2 Atom in a Cavity

While deriving the rate of spontaneous emission in free space, it was observed that this rate was proportional to the optical density of states. Purcell [7] realized that this rate can be enhanced by placing an atom in a cavity resonant with the atomic transition, and subsequently Kleppner [8, 9] discussed the inhibition of spontaneous emission of a Rydberg atom by eliminating vacuum modes at the transition frequency.

To understand the physics better, the Hamiltonian describing the coupling between an atomic transition and a single electromagnetic mode is revisited. As seen earlier, the Hamiltonian evolution of the system led to Rabi-flopping between the atomic states. Two important dissipative processes must be noted at this point. First, mirror imperfections lead to an irreversible loss of photons from the cavity (at a rate $\kappa$, simply related to the cavity quality factor, $Q$, and resonant frequency, $\Omega$, as $\kappa \equiv \Omega/Q$). Second, a coupling between the atom and electromagnetic modes outside the cavity modifies the spontaneous emission rate, $\Gamma$. The latter is easily seen in the case of a 1D or 2D photonic crystal, where the atom can couple to the continuum of electromagnetic modes (radiation modes) in the dimensions lacking a photonic band-gap. Using the formalism of system-reservoir interactions, the atom-cavity system is modeled as being coupled to thermal reservoirs (corresponding to mirror losses and the electromagnetic continuum), and a new "master equation" that incorporates these effects is used to model the system's dynamics.

Depending on the relative strengths of the coupling and decay mechanisms, two different regimes of interaction emerge at this point. In the first regime, the cavity and atomic decay rates ($\kappa$ and $\Gamma$, respectively) exceed the coupling rate ($g$) between the atom and the cavity, i.e., $\Gamma, \kappa >> g$, and is known as the weak coupling (or "bad cavity") regime. The second regime of strong coupling (or "good cavity" regime) is the reverse, with the coupling rate exceeding the decay rates, i.e., $\Gamma, \kappa << g$. It must be noted that the coupling rate, $g$, can be expressed [10] in terms of the dipole moment $\vec{\mu}$,

vacuum field strength $\vec{E}_0$ and mode volume $V$, as

$$g = \vec{\mu} \cdot \vec{E}_0/\hbar$$

$$\text{where } E_0 \text{ satisfies } \epsilon_r \epsilon_0 \left| E_0 \right|^2 V = \hbar\omega/2$$

(1.2)

This expression also highlights the importance of the alignment between the dipole moment and vacuum field for good coupling. The two regimes will now be elaborated upon.

## 1.2.1   Weak Coupling

In this regime, where dissipation exceeds coupling, it is found that the excited atomic state decays exponentially at the rate $\Gamma = \Gamma' + \Gamma_c$, where $\Gamma'$ is the decay rate into the electromagnetic continuum [4], and $\Gamma_c$ is the decay rate to the cavity, given [3] by

$$\Gamma_c = \frac{2g^2/\kappa}{1 + 8\delta^2/\kappa^2}$$

(1.3)

where $\delta = \Omega - \omega$, is the atom-cavity detuning. The previously alluded to effect of the enhancement or inhibition of the spontaneous emission rate can now be readily understood. For a given coupling strength, the decay rate $\Gamma_c$ increases[5] by increasing the cavity $Q$ and reducing the detuning $\delta$. Similarly, rearrangement of the $\kappa$ terms in $\Gamma_c$ shows that inhibition is observed by increasing the cavity $Q$ and detuning $\delta$. To have these effects dominate, the trick of course lies in reducing, to whatever extent possible, the decay to the electromagnetic continuum such that $\Gamma' \to \Gamma_c$. Additionally, under the simplifying assumptions of $\Gamma' = 0$, $\delta = 0$, and atom placement at the field antinode, it is found that the enhancement in the spontaneous emission rate due to the cavity is proportional to $Q/V$, where $V$ is the cavity mode volume. Thus high $Q/V$ cavities provide an ideal method of exploring these effects. The fraction of spontaneous emission from an atom that gets coupled to the cavity mode is commonly referred to as its "$\beta$" factor.

## 1.2.2   Strong Coupling

In this regime, an excited atom emits a photon and it is more likely that this photon is reabsorbed by the atom, rather than decaying incoherently. Thus, a reversible exchange of energy between the atom and cavity mode continues for several cycles before the eventual decoherence sets in.

While the spectrum of spontaneous emission in the weak coupling case is a Lorentzian, here two partially overlapping Lorentzians are observed, separated by the vacuum Rabi frequency $2g$ and each having an equal full-width-at-half-maximum (FWHM) of $(\Gamma + \kappa)/4$. As was seen in the Jaynes-Cummings model, the eigenstates of the coupled system are superpositions of the states

---

[5]Known as Purcell enhancement.
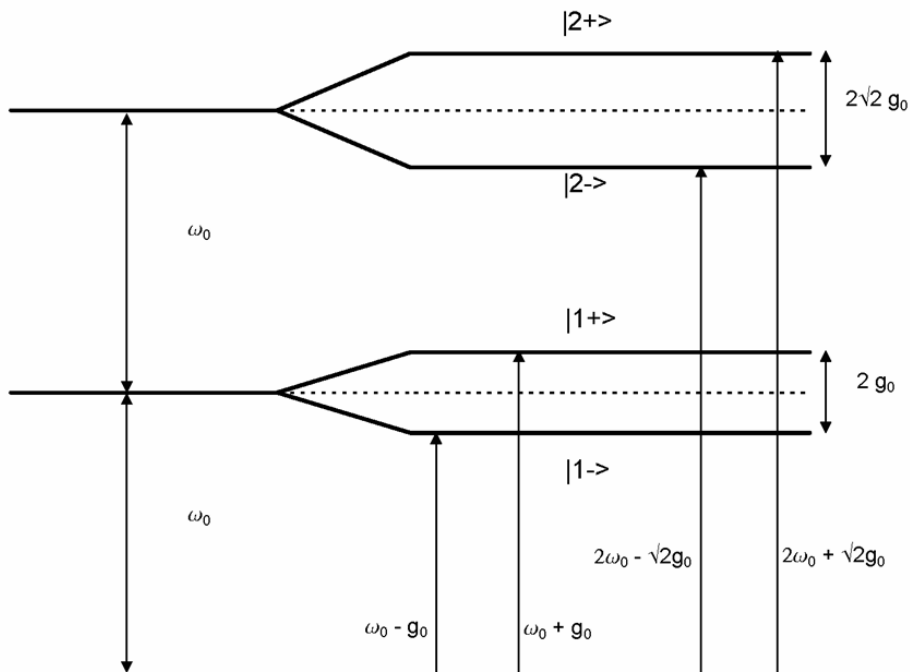
Figure 1.1: Dressed atomic states.

$|s_e, n\rangle$ and $|s_g, n+1\rangle$. In the special case of zero-detuning, this translates into states of the form $(\frac{1}{\sqrt{2}})(|s_e, n\rangle \pm |s_g, n+1\rangle)$, each separated in frequency by $\Delta f = 2g\sqrt{n+1}$. Figure 1.1 shows the "dressed" states and frequency splittings till $n = 1$, and Figure 1.2 graphically shows the emergence of the double-peaked spectrum in the strong coupling regime at zero-detuning by varying the cavity and QD decay rates, while keeping the coupling strength constant for the $n = 0$ eigenstates.
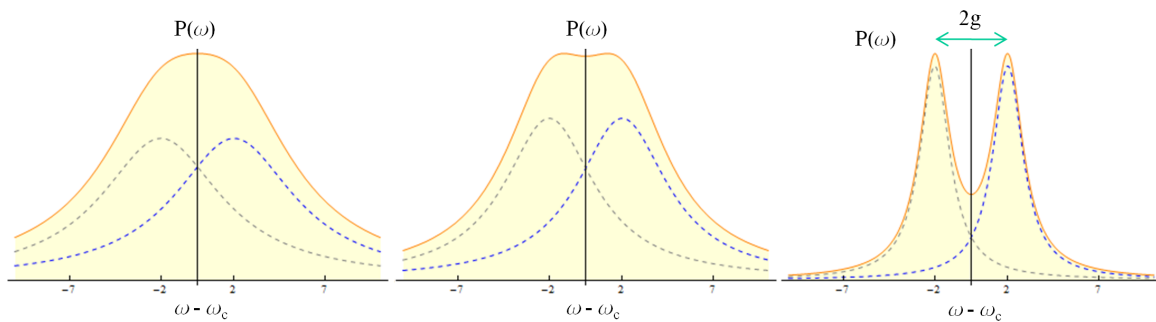


Figure 1.2: Emergence of the double-peaked spectrum in the strong coupling regime (left to right) by decreasing the QD and cavity decay rates, as a function of (normalized) frequency difference, $\omega - \omega_c$, from the cavity frequency, $\omega_c$, at zero detuning, $\delta = 0$. Solid line indicates coupled-system spectrum and dashed lines indicate (Lorentzian) spectra of individual eigenstates for the case of a single photon in the cavity. Individual Lorentzians are centered at $\omega = \omega_c \pm 2$, and have decreasing FWHM - from 4 (left) to 3 (middle) to 1 (right).

These graphs help explain one of the many elegant physical effects seen in strong coupling,

namely that of optical nonlinearity at the single-photon level. Consider an atom strongly coupled to a cavity with a single photon bouncing back and forth. For sake of simplicity, assume that the individual atomic and cavity resonances have no detuning. In this case, the spectrum of the coupled system shows two resonances at $\omega_0 \pm g$, and *no* resonance at $\omega_0$ . Hence, a photon stream incident on the cavity at a frequency $\omega_0$ will get reflected back as long as the cavity has the single photon in it (photon blockade). Once the single photon within decays, the cavity will allow the $\omega_0$ photon stream. Thus a single photon within the cavity can dramatically alter the transmission through the cavity. As noted previously, $|E_0| \propto \sqrt{\omega/V}$, which leads to $g/\kappa \propto Q\sqrt{(\omega/V)}$, once again pointing to high $Q/V$ cavities for exploring these effects.

## 1.3   Atom-Optics to Semiconductor Cavity QED

The physics that has been presented so far has traditionally been studied in the atom-optics community. Certain atomic transitions in cesium or rubidium atoms are typically used, along with micrometer-sized cavities with very-high-reflectivity mirrors. The technical challenges faced are enormous, both in creating the experimental setup and in collecting data. Sophisticated trapping techniques such as magneto-optic-traps are used to hold an atom precisely over a cavity. The atom is then allowed to fall into the cavity region, and it interacts with the cavity for a very short period of time (order of $\mu s$). In this time, a laser pulse must excite the atom, while other laser beams interrogate the state of the coupled atom-cavity system[6]. While these experimental setups are important in understanding physics and demonstrating concept, it is hard to imagine their use in more complicated configurations (e.g., coupling between several cavities), or their portability to industry.

In this context, semiconductor-based cavity-QED presents a refreshing alternative, albeit (understandably) with its own set of complications. Here, cavities can be formed by creating defects in otherwise-periodic dielectric structures (photonic crystals), and Chapter 2 deals extensively with the theory of light confinement in these structures. It must be noted that semiconductor-based, non-periodic structures such as ring resonators can also be used. The counterpart of the atom is the quantum dot (QD). A QD is a small-sized semiconductor structure (several times smaller than the wavelength), which is surrounded in all three dimensions by higher electronic band-gap material. This spatial and energetic confinement leads to a quantized spectrum of the QD transitions, thus making the analogy with discrete atomic transitions apparent. These QD transitions correspond to different exciton[7] configurations (excitons, charged-excitons, bi-excitons).

Since these quasi-atoms are stationary, a big technological challenge has been side-stepped. Of course, such a setup has its own issues[8]. One of them is that the QD embedded devices need to

---

[6]The atomic motion introduces further complications such as velocity-dependent modifications to the spontaneous emission rate, among others.

[7]A bound electron-hole pair.

[8]Since there are no free lunches!

be cooled down to liquid helium temperatures (4-40 K) to narrow the (QD) transition linewidth and reduce non-radiative recombination. Secondly, the QD transition wavelengths are dependent on the QD size, and so, instead of a unique transition frequency, there exists an ensemble of transition frequencies on any given wafer containing QDs. Rapid progress in the design of photonic crystal cavities has led to the development of cavities with $Q$s in excess of $1,000,000$ while maintaining a mode-volume comparable to a cubic wavelength. Design and fabrication of these devices is detailed in chapters 2 and 3, respectively.

## 1.3.1   Quantum Dot Dynamics

After the initial observation of strong coupling [11, 12, 13, 14] between a semiconductor-based cavity and embedded QDs, further experimental work in recent years has revealed some rather unexpected physics. The first is QD-cavity coupling for large values of spectral detuning between QD and cavity resonances [15]. The second is the observation of a third peak [16] in between the two peaks predicted by the Jaynes-Cummings model in the strong coupling regime (see right pane of Figure 1.2). These observations have led to intense work within a relatively short period of time to better model QDs and their coupling to cavities. At the time of writing (April 2010), there is no clear consensus in the physics community about the explanation of these experimental observations, and some leading ideas on the generalization of the two-level-system approximation of the QD are as follows:

- In addition to the decay mechanisms already identified (photon decay from the cavity, and spontaneous emission into free space by the QD), pure dephasing [17, 18, 19, 20, 21] of the QD holes and electrons (potentially at different rates [17]) is taken into account, and is believed to be responsible for non-resonant QD-cavity coupling via phonon mediation [21], as well as the spectral triplet. An alternate [22] explanation attributes the triplet to a quantum interference effect between the different decay channels available for a cavity photon.

- Exciton injection [17, 23] and incoherent cavity-mode pumping [19, 23] rates are also taken into account in computing the spectrum of the coupled system.

- The role of QD hyperfine interactions in the cavity-mediated mixing of different exciton states is also being investigated [17, 24].

Interestingly, some of these different models [17, 19, 22, 23] have shown a good fit with experimental data [16]. Finally, there are strong indications [19] that the signature of being in the strongly-coupled regime is more complex than the observation of a spectral doublet/triplet. As Laussy et al. [23] pointed out, depending on the rate of incoherent cavity pumping, one or two peaks can be observed in the weak *and* strong coupling regimes at zero QD-cavity detuning. Rich theoretical and experimental work in the field of semiconductor cavity-QED is in rapid progress.

## 1.4 Thesis Organization

In this chapter, starting with the intent of controlling the spontaneous emission rate from an atom, the different regimes of light-matter interaction have been touched upon. The following chapters discuss the various aspects of practical devices that allow the exploration of these regimes.

Chapter 2 introduces the theory of light propagation in photonic crystals, using which, the presence of a photonic band-gap in such structures is explained. Methods of numerical computation, and the creation of cavities (resonators) by introducing defects in the photonic crystal lattice is discussed. By modeling a photonic crystal cavity as a Fabry-Perot etalon, the principles of photon confinement in these cavities are illustrated. Finally, an analysis of the cavity geometries fabricated in this thesis is presented.

Chapter 3 discusses the composition of the wafers in which the devices are fabricated. Subsequently, the fabrication sequence is elaborated upon.

In Chapter 4, the experimental measurement of cavity $Q$ is taken up, followed by an analysis of the factors that degrade the $Q$. Wherever possible, improvements are suggested.

Chapter 5 explores the properties of light emission from QDs coupled to photonic crystal cavities. Cavity-induced enhancement of QD luminosity, along with the non-classical nature of the light emission from the QDs is discussed.

Finally, Chapter 6 looks into a proposal of an electrically pumped laser based on a 1D nanobeam cavity. Numerical computations of device performance are presented, along with the fabrication sequence. To conclude the thesis, material system optimizations for increasing cavity $Q$s are presented. Two approaches are discussed, the first involves tailoring QD emission to telecommunication wavelengths ($\lambda \approx 1.55\,\mu$m) in III-V material systems, and the second involves the growth of III-V based QDs on silicon substrates.

# Chapter 2

# Light Trapping Structures - Theory

A photonic crystal[1] is a structure whose dielectric constant has spatial periodicity in one or more dimensions [26, 27]. Two distinct features of photonic crystals distinguish them from bulk dielectric media: the presence of a photonic band-gap, and optical modes with group velocities that can be much lower than the velocity of light in bulk media. In this chapter, the formalism used to quantify light propagation in photonic crystals is described, by means of which, the presence of a photonic band-gap in such structures is explained. Computational tools are then introduced and used to calculate dispersion relations for photonic crystals. After noting practical issues pertaining to viable geometries, cavity construction using photonic crystals is outlined. A discussion of the mechanisms for cavity-$Q$ enhancement follows, and finally the cavity geometries studied in this thesis are described.

## 2.1  General Notions

The presence of a photonic band-gap can be understood by invoking an analogy with crystals that exhibit an electronic band-gap. The periodic arrangement of atoms in a crystal leads to a periodicity in atomic potentials that an electron wave traveling through the lattice experiences. Depending on the frequency, the scattering of the electron wave can be constructive or destructive. The latter case is readily seen in semiconductor crystals, where complete destructive interference causes an electronic band-gap between valence and conduction energy bands. Analogously, a structure that has a periodicity in its dielectric constant can exhibit a photonic band-gap, i.e., a region of frequencies where light propagation is inhibited due to destructive interference between light waves scattering off of dielectric-boundary interfaces. The band-gap is called complete if the inhibition takes place in all directions. The property of modes displaying "unusual" group velocities is also rooted in the scattering mechanism alluded to above. Both of the above properties will become clear once the

---

[1]The first half of this chapter is inspired by the elegant exposition on the subject by J. D. Joannopoulos in his book [25].

dispersion relation for light in a photonic crystal is computed.

The usual method of studying light propagation in photonic crystals is to recast Maxwell's equations into an eigenvalue problem. Starting from the general form of Maxwell's equations, and making the assumption of a source-free, linear, isotropic, and frequency-independent dielectric constant, one gets the following:

$$\nabla \times \vec{E}(\vec{r}, t) = -\mu_0 \frac{\partial \vec{H}(\vec{r}, t)}{\partial t} \tag{2.1}$$

$$\nabla \times \vec{H}(\vec{r}, t) = -\epsilon_0 \epsilon_r(\vec{r}) \frac{\partial \vec{E}(\vec{r}, t)}{\partial t} \tag{2.2}$$

$$\nabla \cdot \vec{H}(\vec{r}, t) = 0 \tag{2.3}$$

$$\nabla \cdot [\epsilon_0 \epsilon_r(\vec{r}) \vec{E}(\vec{r}, t)] = 0 \tag{2.4}$$

where $\vec{E}(\vec{r}, t)$, $\vec{H}(\vec{r}, t)$ represent the electric and magnetic fields, respectively, and $\mu_0$ the permeability of free space. The permittivity, $\epsilon(\vec{r})$, is given by $\epsilon(\vec{r}) = \epsilon_0 \, \epsilon_r(\vec{r})$, where $\epsilon_0$, $\epsilon_r(\vec{r})$ represent the permittivity of free space, and the relative permittivity, respectively.

A justification of the assumptions made is in order:

- Source free - The devices considered here do not have a direct current injection mechanism.

- Linearity - The optical nonlinearities encountered in the material systems considered here (GaAs, Si) are small enough to be treated perturbatively.

- Isotropic - This is really a simplifying assumption, and not a restriction. The generalization to the tensor form of the permittivity is straight-forward, giving the relation between the displacement field $\vec{D}(\vec{r}, t)$ and electric field $\vec{E}(\vec{r}, t)$ as $\vec{D}(\vec{r}, t) = \epsilon_0 \, \overline{\epsilon_r(\vec{r})} \, \vec{E}(\vec{r}, t)$.

- Frequency independence is justified since the goal is to design resonators, which by definition operate in a narrow frequency range where the permittivity is nearly constant. This implies that care must be taken in calculating dispersion relations that involve large wavelength ranges, and it might be necessary to iterate the calculations a few times with the updated permittivity in the frequencies of interest.

The eigenvalue recasting follows from taking the curl of equation 2.2, and choosing a harmonic time dependence of the electric and magnetic fields $(\{\vec{E}, \vec{H}\}(\vec{r}, t)) = \{\vec{E}, \vec{H}\}(\vec{r}) \, e^{-j\omega t})$ leads to

$$\nabla \times \left( \frac{1}{\epsilon(\vec{r})} \nabla \times \vec{H}(\vec{r}) \right) = \left( \frac{\omega}{c} \right)^2 \vec{H}(\vec{r}), \text{ or} \tag{2.5}$$

$$\Theta \vec{H}(\vec{r}) = \left( \frac{\omega}{c} \right)^2 \vec{H}(\vec{r}) \tag{2.6}$$

where the eigen operator, $\Theta$, is defined as $\Theta \equiv \nabla \times \left( \frac{1}{\epsilon(\vec{r})} \nabla \times \right)$, and $\left( \frac{\omega}{c} \right)^2$ are the eigenvalues. The above equation is commonly referred to as the **master equation** [25]. The Hermitian[2] nature of the operator $\Theta$ leads to real eigenvalues. Further, since $\epsilon(\vec{r}) > 0$ everywhere, $\Theta$ is positive semi-definite, and therefore all the eigenvalues are nonnegative. Further, any two eigenmodes with different eigenvalues are orthogonal.

As defined above, a photonic crystal has a spatially periodic permittivity, $\epsilon(\vec{r})$. Consider a spatial direction $\hat{s}$ in which the permittivity is periodic such that

$$\epsilon(\vec{r}) = \epsilon(\vec{r} + n\,S\,\hat{s}) \tag{2.7}$$

where $S$ is the period, and $n \in \mathbb{Z}$. The above equation describes a discrete translation, and must be a symmetry of the system. Stated differently, the (discrete) translation operator $\hat{T}_{\vec{S}}$ must commute with the operator $\Theta$ in the master equation (equation 2.5). As a result, one can construct simultaneous eigenfunctions of both operators. $\hat{T}_{\vec{S}}$, which acts in the following way:

$$\hat{T}_{\vec{S}}\,\epsilon(\vec{r}) = \epsilon(\vec{r} + \vec{S}) = \epsilon(\vec{r}) \tag{2.8}$$

admits exponential-type eigenfunctions, since

$$\hat{T}_{n\vec{S}}\,e^{j\vec{K}\cdot\vec{r}} = \left( e^{jnS\,\vec{K}\cdot\hat{s}} \right) e^{j\vec{K}\cdot\vec{r}} \tag{2.9}$$

Note that if $\vec{K}$ in the above equation (2.9) is replaced by $\vec{K} + (2\pi/S)\hat{s}$, a degenerate eigenfunction is generated whose eigenvalue, by definition, is the same. This vector $(2\pi/S)\hat{s}$ is referred to as the reciprocal lattice vector.

It is worth noting the special case of a medium showing continuous translational symmetry, such as a bulk medium. In this case, the translational operator $T_{\vec{t}}$ will commute with the operator $\Theta$ for any value of translation, $\vec{t}$.

By the property of simultaneous eigenfunctions, the eigenmodes of the master equation (2.5) can be expressed in the following plane wave form:

$$\vec{H}(\vec{r}) = e^{j\vec{K}_x \cdot \vec{r}(x_i,..)}\,\vec{H}_0(\vec{r}(y_i,..)) \tag{2.10}$$

where $\{x_i\}$ denotes the spatial dimensions in which the permittivity is periodic, while $\{y_i\}$ denotes the remaining dimensions such that $\vec{r} = \vec{r}(x_i,..) + \vec{r}(y_i,..)$, $\vec{K}_x$ is any vector in the sub-space denoted by $\{x_i\}$, and $\vec{H}_0(\vec{r}(y_i,..))$ is an arbitrary function in the subspace denoted by $\{y_i\}$. For instance, if the permittivity $\epsilon(\vec{r})$ was periodic in the $x$ direction, the form that $\vec{H}(\vec{r})$ takes would be

---

[2] An operator $\Phi$ is said to be Hermitian if for any vector fields $\vec{X}(\vec{r}), \vec{Y}(\vec{r})$, the following inner product relation holds: $(\vec{X}, \Phi\vec{Y}) = (\Phi\vec{X}, \vec{Y})$.

$$\vec{H}(x, y, z) = e^{jK_x x} \vec{H}_0(y, z) \tag{2.11}$$

Instead of the simple form of $\vec{H}(\vec{r})$ in equation 2.10, a linear combination of degenerate eigenmodes can be used to construct a more general solution of the form

$$\vec{H}(\vec{r}) = \vec{H}_0(\vec{r}(y_i, ..)) \sum_{m \in Z} c_{m, \vec{K}_x}(y_i, ..) \, e^{j(\vec{K}_x + m\frac{2\pi}{S_x}\hat{s}_x) \cdot \vec{r}(x_i, ..)} \tag{2.12}$$

$$= \left( e^{j\vec{K}_x \cdot \vec{r}(x_i, ..)} \vec{H}_0(\vec{r}(y_i, ..)) \right) u_{\vec{K}_x}(x_i, ..) \tag{2.13}$$

where $c_{m, \vec{K}_x}(y_i, ..)$ are constants w.r.t $(x_i, ..)$, $\frac{2\pi}{S_x}\hat{s}_x$ is the reciprocal lattice vector, and by construction $u_{\vec{K}_x}(x_i, ..)$ is periodic in the $\hat{s}_x$ direction with period $S_x$. Thus we have arrived at the well known Bloch's theorem and have expressed the eigenmodes of the system in terms of a plane wave expansion modulated by a periodic function, also known as Bloch states.

As has already been noted, modulo the reciprocal lattice vectors, all Bloch states are identical, which means that it suffices to specify $\vec{K}_x \in [0, \frac{2\pi}{S_x}\hat{s}_x]$. This restricted space of reciprocal lattice vectors is referred to as the Brillouin zone. Analogous to the manner in which the discrete translational symmetry of the dielectric structure reduced the set of reciprocal wave vectors, $\vec{K}_x$ to the Brillouin zone, additional symmetries that might exist in the structure (rotations, reflections, or inversions) further reduce the Brillouin zone to what is known as the irreducible Brillouin zone.

A situation often encountered in practical structures is that of a combination of discrete and continuous periodicity in the permittivity; for instance, in a bulk medium with periodically drilled holes. In such a case, equation 2.12 takes a special form, with $(x_i, ..)$ denoting the dimensions of discrete periodicity, and $(y_i, ..)$ denoting the dimensions of continuous periodicity;

$$\vec{H}(\vec{r}) = \left( e^{j\vec{K}_x \cdot \vec{r}(x_i, ..)} e^{j\vec{K}_y \cdot \vec{r}(y_i, ..)} \right) u_{\vec{K}_x}(x_i, ..) \tag{2.14}$$

where $\vec{K}_x$ is restricted to the irreducible Brilluoin zone and $\vec{K}_y$ is unrestricted.

Given the dielectric structure $\epsilon(\vec{r})$ of a photonic crystal, the eigenmodes (of the form in equation 2.12) can be found by solving the master equation (equation 2.5) and each mode can be labeled by its eigenfrequency $\omega$ and a reciprocal wave vector $\vec{K}_x$ from the irreducible Brillouin zone. This leads to the dispersion relation $\omega(\vec{K}_x)$ for a photonic crystal. A consequence of the periodic nature of $u_{\vec{K}_x}(x_i, ..)$ (and hence $\vec{H}(\vec{r})$) is that the spectrum of eigenvalues of the Hermitian operator, $\Theta$, is discontinuous. That is, at each given $\vec{K}_x$ point, the set of eigenvalues form a discrete set. At the same time $\vec{K}_x$ enters into equation (2.12), and hence in the master equation (equation 2.5), in a continuous sense (within the irreducible Brilluoin zone), which, along with the previous observation, leads to discrete bands of eigenfrequencies in the dispersion relation, and the "folding" of bands at

the edges of the Brilluoin zone.

An important property of photonic crystals, the photonic band-gap, can now be explained. The time-averaged electric field energy

$$U_E = \frac{1}{4} \int \epsilon(\vec{r}) |\vec{E}(\vec{r})|^2 d^3 r \qquad (2.15)$$

is minimized[3] when most of the electric field is concentrated in a region of high $\epsilon(\vec{r})$. Further, as a mode in a particular band approaches an edge of the Brillouin zone with increasing $\left|\vec{K}_x\right|$, it gets folded and creates a second band. As noted previously, modes (and hence bands) with different eigenvalues are orthogonal. As a result of all the above, at an edge of the Brillouin zone, orthogonality between the two bands can only be maintained if the two bands differ in frequency. The mode in the lower band (called the dielectric band) concentrates its energy in regions of high $\epsilon(\vec{r})$, while remaining orthogonal to the mode in the higher band (called the air band), which concentrates its energy in the regions of lower $\epsilon(\vec{r})$. It is this splitting in frequency that creates a photonic band-gap: a spectral region that does not contain any eigenmodes of the system. The width of this band-gap is correlated with the dielectric contrast ($\epsilon_{max}/\epsilon_{min}$) in the structure.

The presence of a photonic band-gap in one or more dimensions makes photonic crystals very elegant structures for constructing resonators. Such resonators, called photonic crystal cavities, are based on the principle that if an electromagnetic excitation (light) within the band-gap can be excited in the crystal, its propagation within the crystal is inhibited, and it remains spatially localized in the neighborhood of the excitation. The following sections will delve into resonator considerations and designs.

### 2.1.1  Practical Considerations

At this point, it is instructive to consider practically feasible devices. Planar devices have the great advantage that they are amenable to electron-beam/photo lithography, and all the mature tools and techniques from the semiconductor processing industry can be taken advantage of. While it would be ideal to have a 3-dimensional photonic band-gap, a planar fabrication sequence lends itself most naturally to 1D or 2D photonic crystal cavities, and other mechanisms such as index confinement [28] (via total-internal-reflection [TIR]) must be used to confine light in the remaining dimension(s)[4].

As mentioned previously, the extent of the band-gap depends on the dielectric contrast in the structure. A larger band-gap results in a tighter confinement of light to the resonator, and allows room for some device imperfections that are inevitable during fabrication. A maximum dielectric contrast is possible when a high index material is surrounded by air ($\epsilon_r = 1$).

---

[3]This heuristic idea is formalized in the electromagnetic variational theorem.
[4]This mechanism is behind the confinement of light to the core of a fiber optic cable.

Keeping in mind the above two considerations, leads to photonic crystal slabs. Such structures have periodic permittivity in one or two dimensions in-plane, and uniform permittivity (within the slab) in the remaining dimension. The technique of creating free-standing semiconductor slabs by selective wet etching methods will be discussed in Chapter 3.

## 2.2   Computational Electrodynamics

For all the elegance of photonic crystals, a completely analytical description is elusive, and these devices must be analyzed numerically. Powerful numerical programs, such as the open-source applications developed by the MIT Ab-Initio group[5] are employed. A plane-wave basis for the eigenmodes is used to solve the master equation (equation 2.5) in the eigensolver program MPB [29].
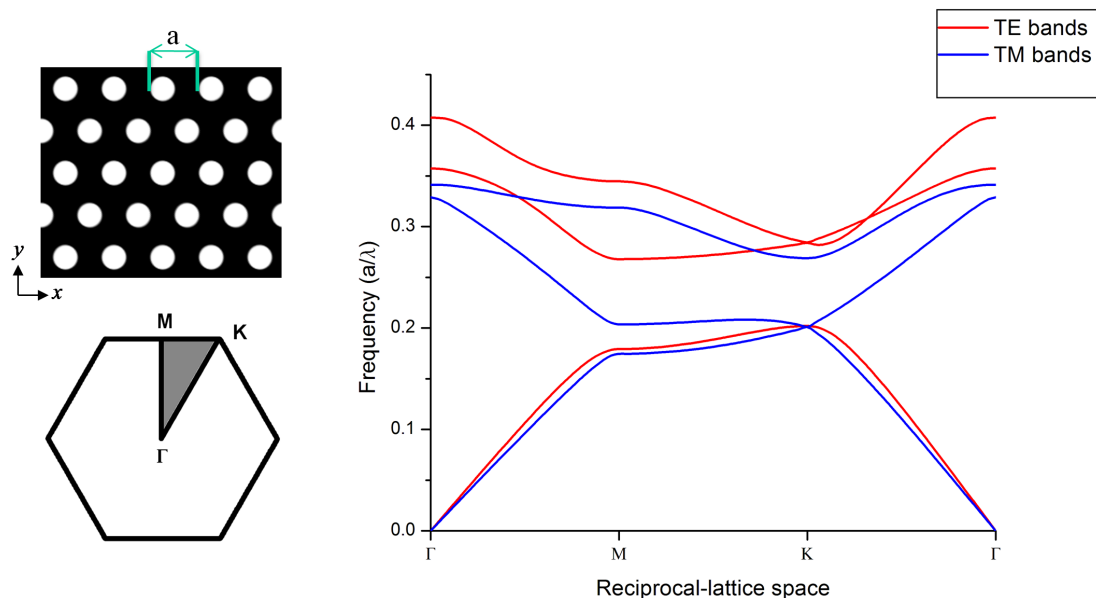


Figure 2.1: (Left) Real-space and reciprocal-space representation of triangular lattice of air holes (radius $r = 0.30\ a$) in an infinitely thick structure ($\epsilon_r = 12.605$). (Right) Corresponding dispersion relation showing TE and TM eigenmodes.

To make matters that have been discussed so far more concrete, an example of a 2D photonic crystal is discussed. Such an ideal structure is infinite in the $z$ direction, and has periodic permittivity in the $x$-$y$ plane, generated by drilling a triangular lattice (lattice constant $a$) of air holes (radius $r$) in an infinite bulk medium of relative permittivity $\epsilon_r$. It must be noted that since Maxwell's equations are scale-invariant, the choice of a length scale is arbitrary, and it is convenient to express all quantities in terms of the lattice constant. The left pane of Figure 2.1 illustrates the top view of such a structure along with the (shaded) irreducible Brillouin zone. Due to the infinite extent of the structure in the $z$ direction, there are two possible polarizations: transverse-magnetic (TM),

where $H_z(\vec{r}) \equiv 0$, and transverse-electric (TE), where $E_z(\vec{r}) \equiv 0$. Figure 2.1 shows the dispersion relation, $\omega(k)$, of the structure for both polarizations[6]. Note the presence of a photonic band-gap for only the TE polarization (for $\omega/2\pi = a/\lambda \approx 0.20 - 0.27$). The group velocity at any $(\omega, k)$ point is $\partial\omega/\partial k$, and as can be seen in the dispersion relation (for the first few bands), takes on values close to zero at high-symmetry reciprocal-lattice points such as the $M, K$ points. The velocity of light in a medium corresponds to its group velocity[7] at a particular frequency, and thus the unusual group velocity in photonic crystals can be exploited for dramatic light slow-down [30, 31].
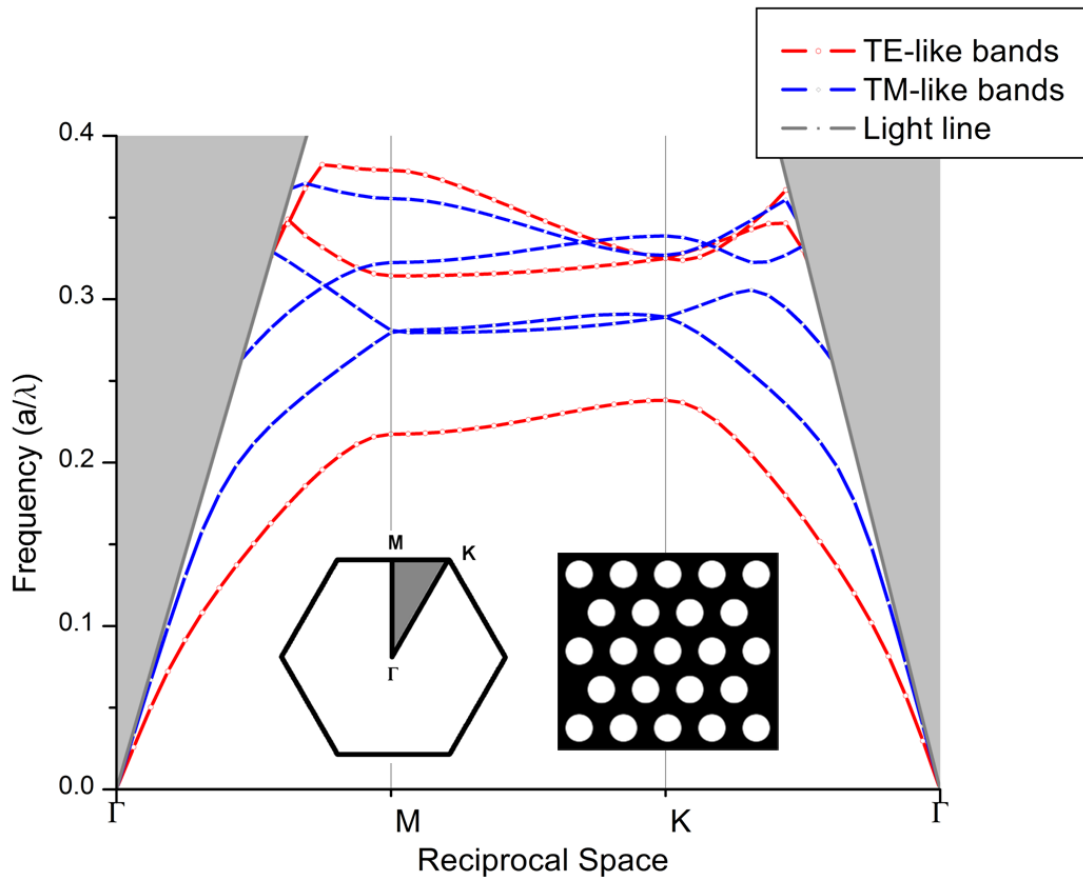


Figure 2.2: Dispersion relation showing TE-like and TM-like eigenmodes for a triangular lattice photonic crystal slab (thickness $d = 0.75\,a$, radius $r = 0.30\,a$, $\epsilon_r = 12.605$). Insets show real-space and reciprocal-space representation of the photonic crystal.

To make matters more realistic, the case of a structure with finite extent in the $z$ direction is now considered. Frequency domain simulations of a photonic crystal slab consisting of a triangular lattice of air holes reveal the extent of the photonic band-gap as a function of the in-plane Bloch wave vectors, as seen in Figure 2.2. A subtlety must be mentioned at this point: Since the structure only has 2D periodicity, light is (incompletely) confined in the vertical direction by TIR. Therefore,

---

[6]The simulations and dispersion relations use natural units, i.e., speed of light, $c \equiv 1$.

[7]The group velocity of light in a bulk medium is given by, $v_g = c/n$, where $n$ is the refractive index.

any mode (designated by $[\omega, k]$) lying above the light line (defined as, $\omega = c\,k$) will always couple to the continuum of electromagnetic modes (called radiation modes). Thus, the photonic band-gap in this case is defined as the frequency range that is devoid of any *guided* modes [32] below the light line (i.e., for $\omega < ck$). Radiation modes, of course, exist at all frequencies.

It should be noted that all guided bands can be divided into two groups depending on the E-field symmetry with respect to the plane in the middle of the slab; even and odd (or equivalently, transverse electric [TE]-like or transverse magnetic [TM]-like, to invoke the similarities to their 2D counterparts). In case of the triangular lattice of air holes, it is well known that a band-gap exists only for TE-like modes, and this can be seen in Figure 2.2.

The spectral location of the photonic band-gap is a function of the slab thickness (see Figure 2.3). Qualitatively, one can imagine starting from an infinitely thick slab and "squeezing" the slab (and thus the confined mode) to a finite thickness. Thus, as the slab thickness is decreased, so is the mode wavelength, and the mode frequency increases as a result. The slab thickness is chosen such that only the lowest-order mode in the vertical direction is supported, thereby keeping the mode volume at a minimum and suppressing the coupling to the higher-order slab modes. Therefore, the slab thickness tends to be approximately close to half the wavelength of light in the material for optimal confinement.
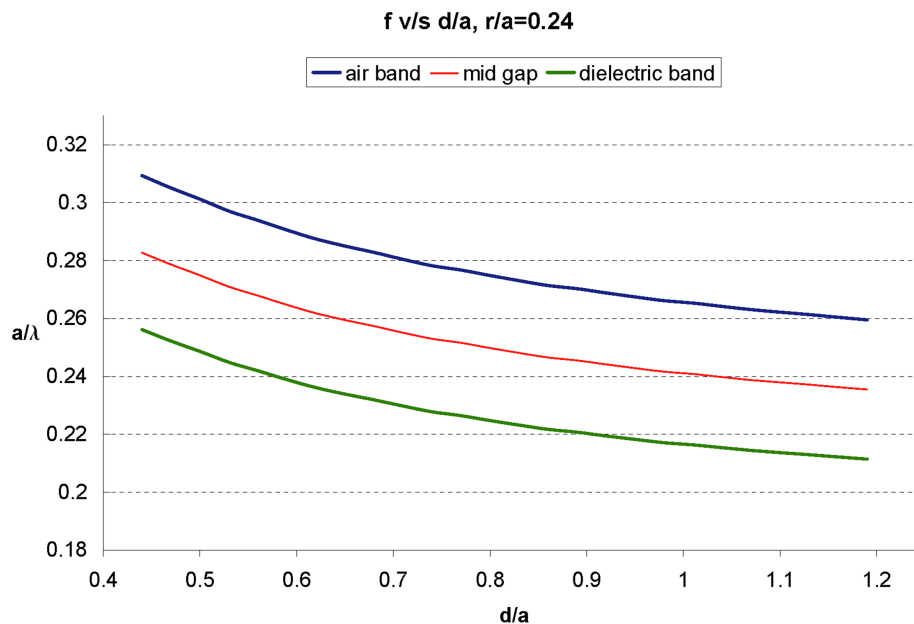


Figure 2.3: Photonic band-gap variation as a function of normalized slab thickness ($d/a$).

As alluded to previously, the presence of a photonic band-gap can be exploited for resonator/cavity formation by simply creating a "defect" (such as a missing/modified hole[s]) in the photonic crystal. Strictly speaking, a defect makes the structure lose its crystalline property, but if the defect is small enough, the situation can be handled perturbatively. Physically this means that if light with a

frequency within the band-gap is excited inside the defect, it propagates some finite distance away from the defect before experiencing the band-gap, i.e., it evanescently decays away from the defect.

The defect also presents a computational challenge for frequency domain calculations which is overcome by defining a "super cell"—a photonic crystal containing the defect and a sufficiently large number of periods around it such that the mode excited in the defect region becomes negligible at the super cell boundaries. Not only does this require greater computer memory because of the larger size of the computational cell, many more bands must be computed because the original bands get folded many times over due to the introduction of an artificial periodicity by the super cell. As an illustration, Figure 2.4 depicts the electric field energy density for different modes within the band-gap of an infinitely-thick 2D triangular lattice of air holes. Note that the cavity structure has four-fold symmetry which shows in the mode profiles.
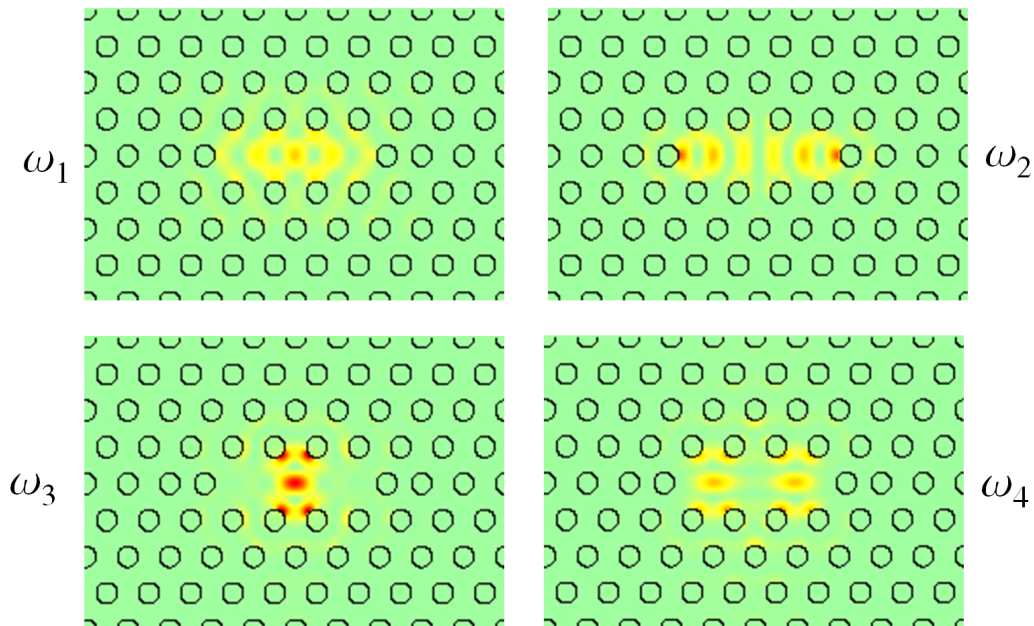


Figure 2.4: Frequency-domain simulations showing electric field energy density profiles of defect modes in a 2D triangular-lattice photonic crystal cavity with radius $r = 0.24\,a$

In practice, frequency domain simulations are performed for the defect-free case to reveal the spectral extent and location of the photonic band-gap. Finite-difference time-domain (FDTD) simulation methods [33] are then employed to launch a mode within this band-gap to find the exact resonant wavelength, $Q$ (by computing the inverse Fourier transform of the cavity field), and mode profiles. This brute-force technique[8] discretizes the dielectric structure (in what is known as the Yee lattice [35]) and time-steps the electromagnetic fields according to equations 2.1–2.4.

---

[8]MEEP [34], one of the open-source applications developed by the MIT Ab-initio group for performing FDTD simulations is primarily used in this thesis.

*Aside* - The choice of a triangular lattice is interesting. It is a curious geometrical property that for a planar crystal lattice, only 2-, 3-, 4-, and 6-fold symmetries can exist. Structures with 5-, 7-, 8-fold (and higher) symmetries were thought to not exist in nature for a long time, till their relatively recent experimental discovery [36] in 1984. These structures are called quasi crystals. Though strictly not periodic, they have a long-range order. Long before this, however, expressions of 5-fold symmetric structures were found in 15$^{\text{th}}$ century Islamic art [37], five centuries before Roger Penrose formally studied and explained them. Photonic quasi crystal cavities have been fabricated by several research groups [38], and while they are very elegant structures, no real advantage over regular photonic crystal cavities has been found. The latter are mathematically more tractable in both design and analysis, and are thus the devices of choice.

## 2.3 Photonic Crystal Cavities
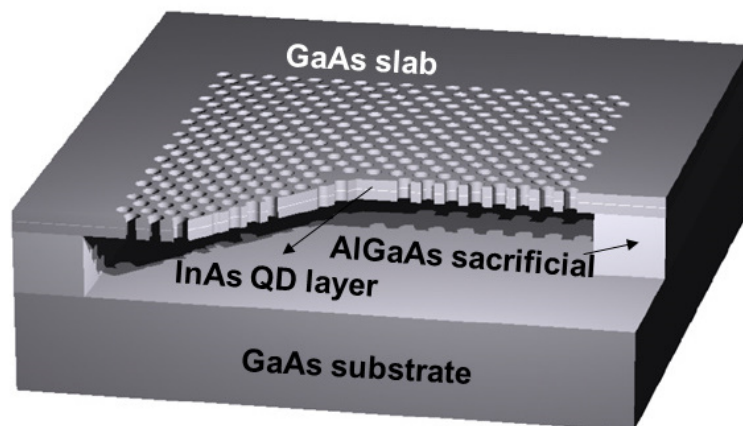


Figure 2.5: Cut-away of an air-suspended L3 photonic crystal cavity showing layer composition. (Credit: Se-Heon Kim.)

Having sketched the basic methods for analyzing photonic crystal cavities, a description and analysis of the cavities designed and fabricated for this thesis is presented. With the constraint of planar fabrication, it is natural to consider cavity geometries that inhibit propagation in-plane. This idea finds expression in a 2D lattice of air holes. Device composition is elaborated in Chapter 3, but for now it suffices to note the presence of internal light sources in the middle of the slab in the form of InAs quantum dots (QDs). Typical QD dimensions are $20-30$ nm in-plane, and $\approx 5$ nm in height; as a result, QD electric field polarization tends to be dominantly in-plane, and is the chief reason for the choice of the triangular lattice—the QDs couple well with the TE-like polarization (electric field is entirely in-plane in the $z = 0$ symmetry plane of the slab) of the cavity *and* as noted in the previous section, such a structure shows a band-gap (also see Figure 2.2) for TE-like polarizations.

A cut-away section of an L3 cavity structure (elaborated later) showing the mid-plane QD layer and the 2D photonic crystal is seen in Figure 2.5.

### 2.3.1  Fabry-Perot Etalon Model

To understand light confinement in photonic crystal cavities, it is physically insightful to model these resonators as symmetric Fabry-Perot etalons. Such an etalon is simply composed of a waveguide sandwiched between identical mirrors, as depicted schematically in Figure 2.6. In the geometries that will be explored here, the mirror is a distributed, not "lumped" element.
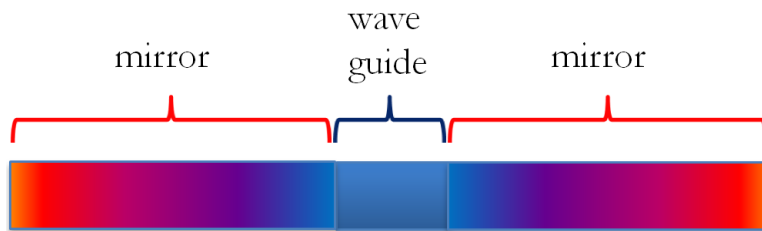


Figure 2.6: Schematic showing cavity modeled as a waveguide sandwiched between mirrors.

Photonic crystals provide a very elegant method of implementing both waveguides as well as mirrors. This beautiful property can be seen in Figures 2.7–2.8, where the dispersion relation for a rib waveguide is compared with that of a rib perforated by a periodic array of air holes (i.e., a 1D photonic crystal). In these dispersion relations, modes below the light line are guided modes, whereas modes with $\omega > ck$ are radiation modes. Note two very significant differences between these two cases, one, the presence of a photonic band-gap, and two, very low group velocities near the edge of the Brillouin zone, both in the case of the 1D photonic crystal (analogous to a 1D Bragg mirror). Thus, by choosing an appropriate frequency, one obtains a mirror (if within the band-gap), or a waveguide with very low group velocity (just above or below the band-gap), both of which are elusive in a rib waveguide. Inside the band-gap, modes become evanescent and instead of the form seen previously in equation 2.12, the magnetic field takes on a form

$$H_z(r) = e^{jkz}\, u(z)\, e^{-\kappa z} \tag{2.16}$$

corresponding to a complex wavevector $k + j\kappa$. The importance of low group velocities will become apparent subsequently.

To make matters concrete, consider a waveguide of length $l$ that supports a waveguide mode with a group index $n_g$ ($\equiv c/v_g$, $v_g$ being the group velocity) at a wavelength $\lambda_0$. Let the (complex) mirror reflectivity be $|r(\lambda)| e^{j\psi_r(\lambda)}$ where $|r(\lambda)|$, $\psi_r$, represent the reflection amplitude and phase, respectively. For such a system, the quality factor at a wavelength $\lambda_0$ is [39]
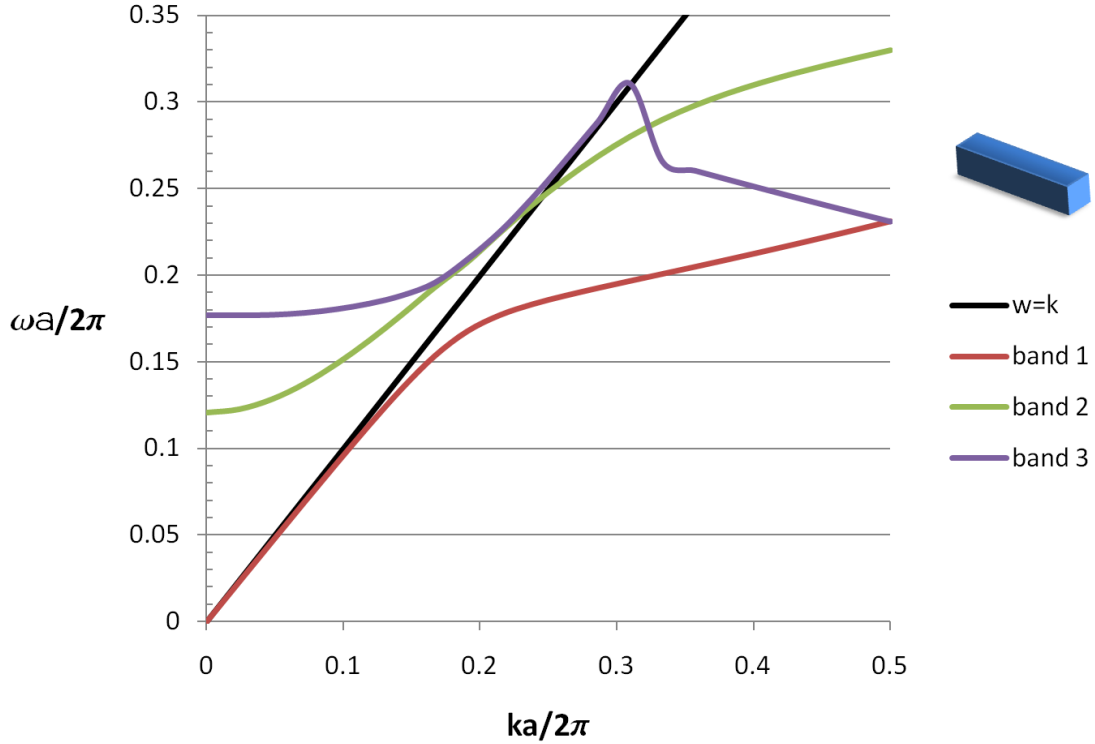
Figure 2.7: Dispersion profile for rib waveguide (width=$a$, height=$0.75a$) with $\epsilon_r = 12.605$. Only TE-like modes are considered here.

$$Q = \frac{\pi}{1 - |r(\lambda_0)|^2} \left[ \frac{2\,l\,n_g(\lambda_0)}{\lambda_0} - \frac{\lambda_0}{\pi} \left( \frac{\delta\psi_r}{\delta\lambda} \right)_{\lambda_0} \right] \tag{2.17}$$

Three immediate factors impacting cavity-$Q$ positively can be identified by examining the above equation: high mirror reflectivity, slow group velocity, and low $\left( \frac{\delta\psi_r}{\delta\lambda} \right)_{\lambda_0}$. These factors are now investigated, and for sake of simplicity (particularly computational), a 2D geometry of collinear air holes in a rectangular waveguide is explored. This helps illustrate the physical principles of light confinement, while circumventing the need for time-consuming 3D calculations.

### 2.3.1.1  Resonator Construction

The first issue is of resonator construction. To implement the schematic in Figure 2.6, starting with a rectangular strip of width $a$, a section of air holes with radius $r = 0.30\,a$ is chosen as the mirror, and a section of air holes with a smaller radius $r = 0.15\,a$ is chosen as the waveguide. It is important to scale (reduce, in this case) the lattice constant of the waveguide section with respect to the mirror section in order to position a waveguide mode inside the photonic band-gap of the mirror section. Figure 2.9 shows the appropriately scaled dispersion relations for periodic versions of each of these sections. For sake of comparison, the dispersion relation for a homogeneous waveguide is also shown.
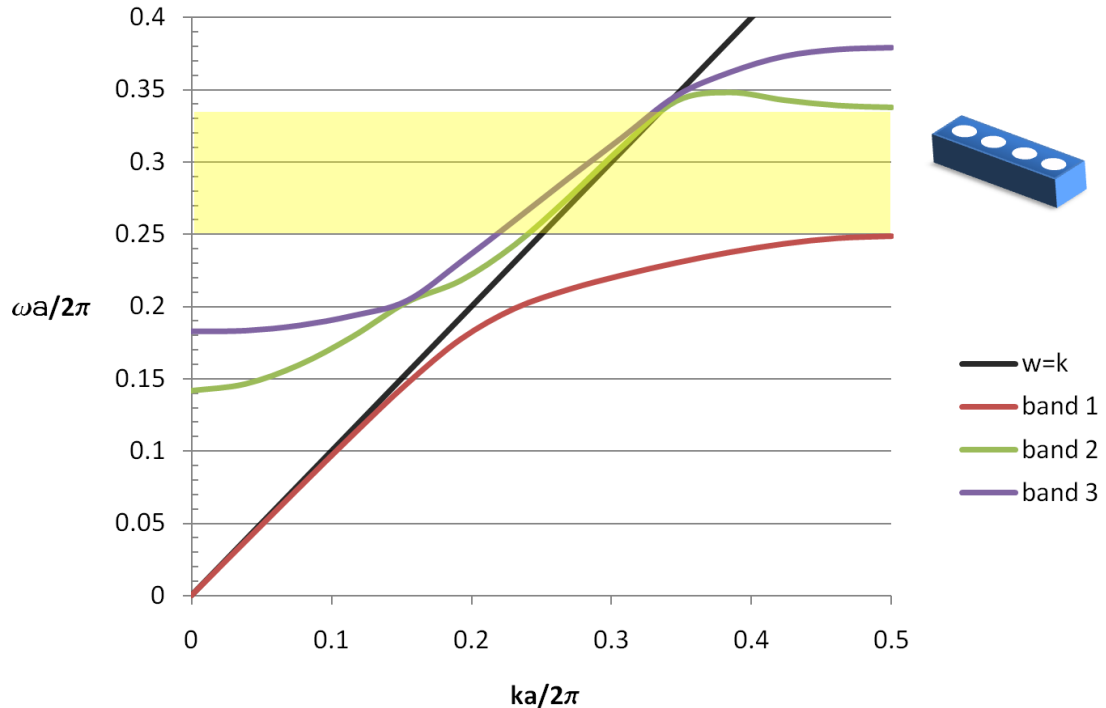
Figure 2.8: Dispersion profile for air holes (radius $r = 0.30\,a$) in a beam (width=$a$, height=0.75$a$) with $\epsilon_r = 12.605$. Yellow shading reveals photonic band-gap. Only TE-like modes are considered here.

Finally, a four-hole waveguide section is sandwiched between twelve-hole mirror sections on either side, and a resonant mode within the mirror band-gap is found at $\omega a/2\pi = a/\lambda = 0.219$, with $Q = 6,330$.

### 2.3.1.2   Mirror Reflectivity

The second issue is of mirror reflectivity. By setting up the cavity as above, light in the waveguide section is a guided mode, where it takes an evanescent form in the mirror section, inevitably leading to a mode mismatch. By implementing a "taper" section between the waveguide and mirror sections, an increase in reflectivity has been proposed and demonstrated [39, 40, 41] in various geometries. The purpose of the taper is to minimize mode-mismatch by gradually increasing the (imaginary) wavevector $\kappa$ (see equation 2.16) in the mirror section.

In the mirror-waveguide-mirror geometry discussed above, a taper is now introduced in the twelve-hole mirror section by linearly decreasing (in steps of 2%) the radius of the six mirror-section holes nearest to the waveguide section (as well as a corresponding shrinkage of the pitch by the same amount), i.e., the first mirror-section hole has a radius equal to 88% of the end holes. It is found that the cavity blue-shifts to $a/\lambda = 0.223$, with a significant $Q$ increase to $Q = 15,934$. The cavity blue-shift is expected because of a slight reduction in the cavity length by the shrinkage of
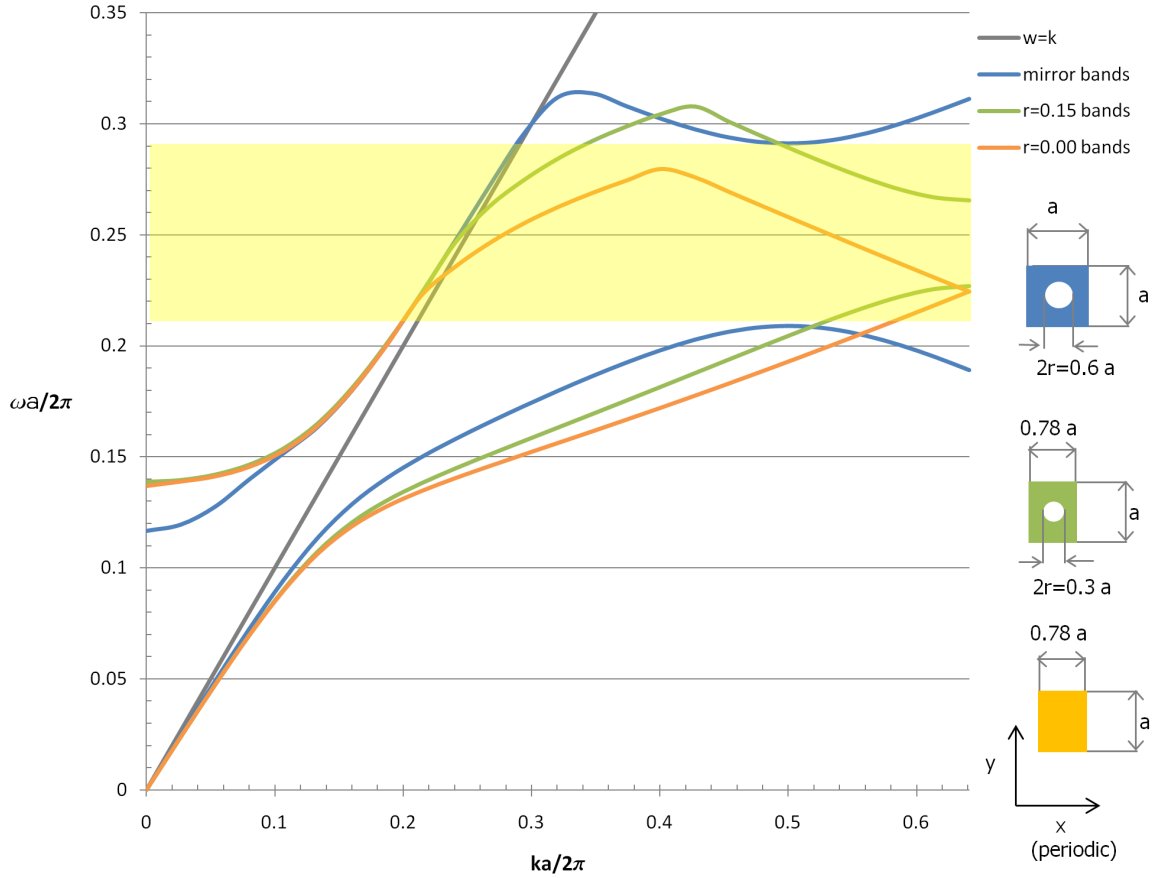
Figure 2.9: Scaled dispersion relation for (2D) mirror and waveguide sections. Right side shows the "unit" cell of each section. Yellow shading shows the band-gap for the mirror section ($r = 0.30a$). Rectangular strip width=$a$, $\epsilon_r = 12.605$. Only TE modes are considered here.

the mirror-section holes nearest to the waveguide.

To quantify the change in reflectivity due to tapering, numerical calculations using FDTD were performed on a waveguide-mirror geometry, schematically depicted in Figure 2.10. In this case the waveguide is simply a homogeneous rectangular strip, while the mirror section is as discussed earlier. A line source is placed in the waveguide and the Poynting-vector flux through the end of the waveguide section is computed with and without the taper, and is normalized by the flux in the case without a mirror section[9]. It is clear from Figure 2.11 that tapering increases reflectivity. All other things held constant, equation 2.17 suggests that $Q \propto 1/(1 - R^2)$ and using the computed values for reflectivity ($R$), tapering predicts an increase in $Q$ from 6,330 to 13,578, close to the actual value of 15,934.

It might be argued that the increase in cavity-$Q$ could also stem from a decrease in the group velocity, as the dispersion relation for the waveguide mode reveals a decrease in group velocity

---

[9]A technical point must be noted: flux (through the plane) is first calculated without the mirror, and is subtracted from the flux in the presence of the mirror. This is to remove the contribution of incident power in the reflected flux calculation.
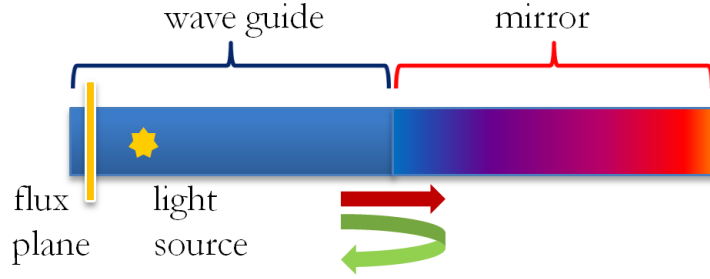
Figure 2.10: Schematic showing reflectivity computational cell of a waveguide adjacent to a mirrors.
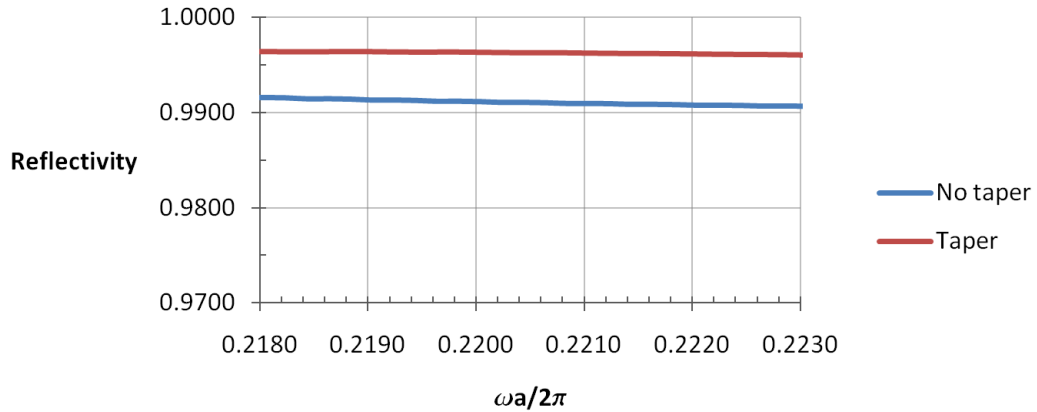


Figure 2.11: Reflectivity as a function of normalized frequency for the waveguide-mirror schematic shown in Figure 2.10.

(see slope of lower green curve for $\omega a/2\pi > 0.210$ in Figure 2.9). To verify the contribution of the taper in the reflectivity increase, a waveguide with nearly-constant dispersion in this frequency range is substituted, and the role of the taper investigated. Such a waveguide is implemented by a homogeneous strip, and its dispersion is shown by the orange curve in Figure 2.9. FDTD computations (summarized in Table 2.1) indicate a change of $(a/\lambda, Q)$ from (0.217, 3,845) to (0.222, 10,490) by implementing the same taper as above, thus confirming the increase in reflectivity by tapering. Using the computed reflectivities at these frequencies, tapering should increase the $Q$ from 3,845 to 8,605, again slightly short of the actual value of 10,490. Since slow-light effects are ruled out in this case, the difference in $Q$ is attributed to a change in the phase term in equation 2.17, arising from a tapering-induced decrease in effective cavity-length. As noted previously, the slight decrease in effective cavity-length shows up in a blue-shift of the cavity wavelength.

| | No taper | Taper |
|---|---|---|
| $r_{wg}/a = 0.00$ | (0.217, 3,845) | (0.222, 10,490) |
| $r_{wg}/a = 0.15$ | (0.219, 6,330) | (0.223, 15,934) |

Table 2.1: Table of $(a/\lambda, Q)$ values for different waveguide and taper implementations.

## 2.3.1.3 Group Velocity

The third issue is of low group velocity. By examining the dispersion diagrams in Figure 2.9 and locating the resonant cavity frequencies on them, it is evident that that the modes mentioned previously do not lie at the edge of the Brillouin zone, and hence do not make full use of the low group velocities available near the edge. With this consideration noted, the waveguide section was perturbed by replacing the holes with rectangles. The transverse dimension of the rectangle was varied continuously, and a dramatic improvement in cavity-$Q$ was observed, reaching a peak of $604,944$. As seen in Figure 2.12 and in all tunings considered, the $Q$ exceeded the $Q$s of the waveguide of holes. To investigate whether the 37-fold increase in $Q$ is related to low group velocity, the dispersion relations and group velocities for the two different waveguide implementations are considered. In the first implementation, four holes with radius $r = 0.15\,a$ and pitch $0.78\,a$ are used, while in the second, four rectangular slits with the same pitch are used (transverse size$=1.475\,a$, axial size$=2 \times 0.15\,a$). In the former case, FDTD calculations show $(a/\lambda, Q) = (0.223, 15{,}934)$, while in the latter case $(a/\lambda, Q) = (0.227, 604{,}944)$. Using the dispersion plots as seen in Figure 2.13, mode frequencies are used to find the corresponding wavevectors and group velocities (marked by arrows in Figure 2.13). Surprisingly, the reduction in group velocity is very small and can't explain the dramatic $Q$ enhancement.
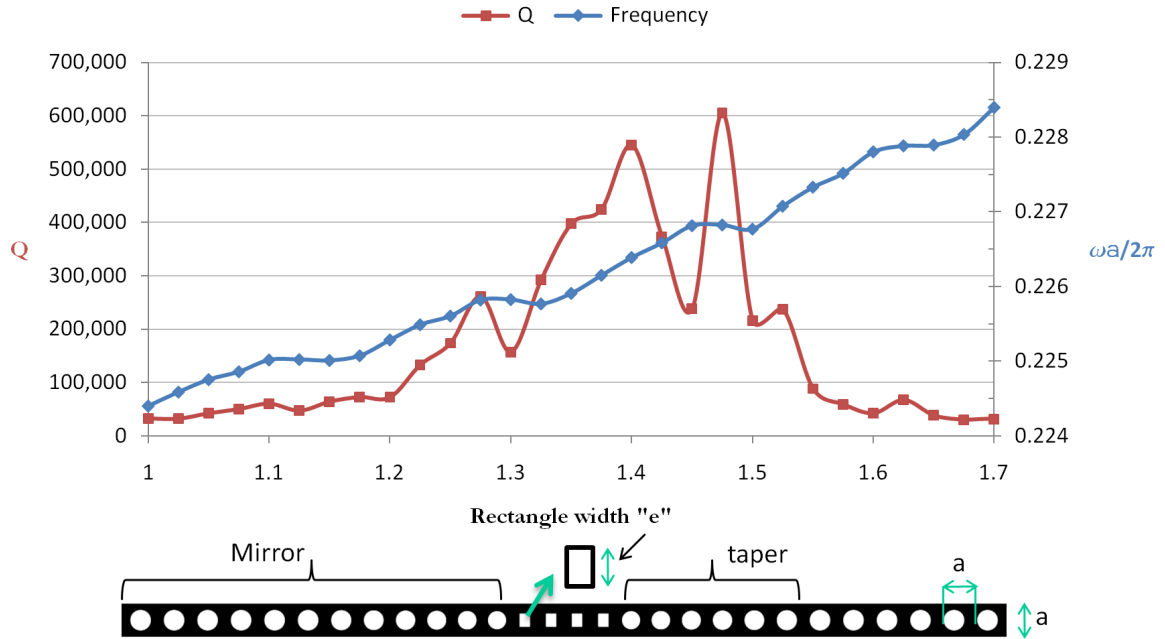


Figure 2.12: Cavity-$Q$ (left axis) and frequency (right axis) as a function of transverse rectangular size (e, in units of axial rectangular size). The axial rectangular size is kept constant at $2 \times 0.15\,a$, and (tapered) mirror implementation is described in the text. Bottom pane shows the cavity in a rectangular strip of width $a$ in a material with $\epsilon_r = 12.605$.

These results highlight the weaknesses of the Fabry-Perot model. Photonic crystal-based mirrors
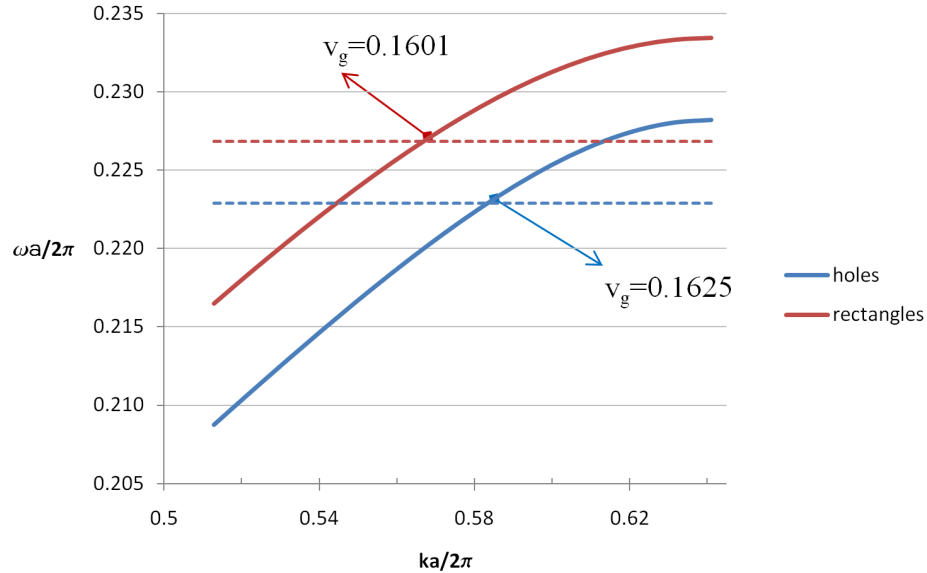
Figure 2.13: Dispersion profiles for periodic waveguides formed out of holes(blue) and rectangles(red). Dashed lines show the cavity frequencies in the respective cases. Arrows show group velocity at cavity frequencies. Note that speed of light $c \equiv 1$.

are not "lumped" elements and the mirroring action happens over several periods of the photonic crystal holes. Furthermore, the reflection-phase term in equation 2.17 is not well defined because there is no distinct waveguide-mirror boundary. All the dispersion relations shown so far assume an infinitely periodic structure, and it is expected that there will be deviations when considering short waveguide sections. Taken together, these tools are of intuitive use in cavity design, but as seen in the case of the rectangular tuning, inadequate in predicting or fully explaining $Q$-enhancing mechanisms. A few other ideas useful in guiding cavity design will be elaborated upon in the context of 2D photonic crystal cavities, taken up in the next sub-section.

Having sketched the physics of optical confinement in computationally tractable 2D geometries, a description of practically realizable devices is in order. The majority of devices fabricated in this thesis are 2D photonic crystal cavities. The relatively recent [42, 43] discovery of high-$Q$ cavities in 1D nanobeam structures is taken up after that.

## 2.3.2    2D Cavities - L3 and L1

L$x$ cavities are formed by removing $x$ adjacent, collinear holes in a triangular lattice, forming a "spacer" region. Additionally, some holes in the immediate neighborhood of the holes are modified to increase the cavity-$Q$. L3 and L1 cavities are discussed here as they form the bulk of devices fabricated for this thesis.

The general design philosophy [44] in these devices is to engineer the region around the spacer such that a mode is "gently" confined within the spacer. Qualitatively, this means that the neighborhood

around the spacer is adjusted such that the spatial envelope of the field in the cavity doesn't get abruptly terminated, but instead is smoothly terminated. To give an illustration of the dramatic improvement in cavity-$Q$, consider the following sequence of cavity pertubations. First, a "plain" L3 cavity is created by removing three air holes. Next, the holes on either end of the spacer are modified [44]. Finally, three holes on either side of the spacer are modified [45] to give a $Q$ that is much higher than the plain L3 design (see Table 2.2). The cavity mode volume [46], $V$, defined in the following way

$$V \equiv \frac{\left[ \int_V \epsilon(\vec{r}) |\vec{E}(\vec{r})|^2 d^3 r \right]}{\max \left[ \epsilon(\vec{r}) |\vec{E}(\vec{r})|^2 \right]}$$

(2.18)

does not increase significantly in this tuning process, resulting in an overall improvement in $Q/V$.



| Design# | 1 | 2 | 3 |
|---|---|---|---|
| $r'/a$ | 0.30 | 0.30 | 0.30 |
| $s_a/a$ | 0.00 | 0.17 | 0.17 |
| $s_b/a$ | 0.00 | 0.00 | 0.025 |
| $s_c/a$ | 0.00 | 0.00 | 0.17 |
| $Q$ | 6,045 | 77,899 | 108,754 |
| $a/\lambda$ | 0.251 | 0.249 | 0.249 |
| $V/(\lambda/n)^3$ | 0.302 | 0.368 | 0.367 |
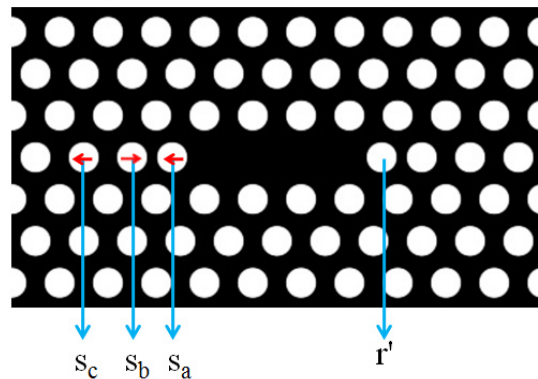
Table 2.2: Improvement in $Q$ by hole-tuning process for L3 cavity. In all, $r/a = 0.3$, $d/a = 0.75$, $n^2 = 12.605$. Schematic on right shows the tuning parameters.

By increasing the number of photonic crystal periods surrounding the spacer region, in-plane photon loss can be virtually eliminated, and coupling to radiation modes (corresponding to wavevectors in the light cone: see gray-shaded region of Figure 2.2) in the vertical dimension is essentially the source of photon loss (apart from material and processing-induced losses). The particular high $Q$ mode chosen in Table 2.2 has the following electric field symmetries about the principal symmetry-planes of the cavity: $(x = 0, y = 0, z = 0$ : even, odd, even); as a result the $y$-component of the electric field is dominant. Taking the spatial Fourier transform of the dominant cavity fields $(E_y)$ reveals the wavevector composition, and sheds light on the success of the tuning mechanism described above. The transformed fields for design #1 and #3 are shown in Figure 2.14, and it is very evident that the wavevector components within the light cone are severely reduced in the case of design #3. This quantifies the idea of "gentle" confinement alluded to earlier—abrupt cavity terminations tend to generate wavevectors within the light cone, and thus, by modifying this termination suitably, the $Q$ can be greatly increased. A corresponding (slight) increase in the mode volume and wavelength is indicative of an increase in the effective cavity length and or a larger penetration into
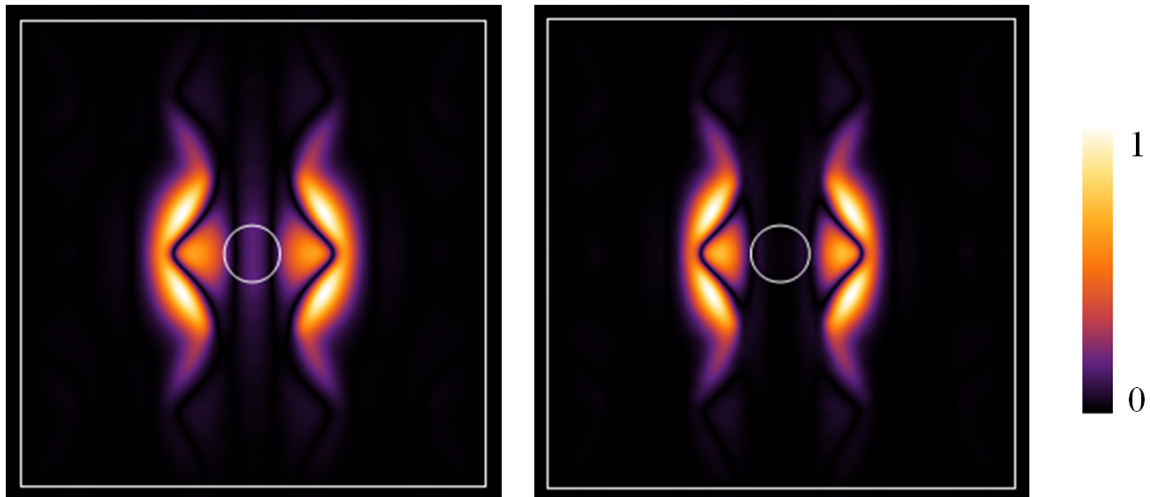
Figure 2.14: Absolute value (normalized) of spatial Fourier transforms of $E_y$ fields in a plane just above (and parallel to) the slab surface for design #1 (left) and design #3 (right). Inner circle denotes the light cone, center of the circle is the origin of the $k_x - k_y$ plane, and bounding box denotes wavevectors $k_{x,y} = \pm 2\pi/a$.

the surrounding photonic crystal.

An alternative explanation [39] of the $Q$ improvement by end-hole tuning, as mentioned earlier in the chapter, comes from the modeling of the L3 cavity as a Fabry-Perot cavity. Modification of the spacer neighborhood increases the reflectivity of the end mirrors of the cavity, thus increasing the $Q$. While the mirror tapering can be implemented by a combination of end-hole radius shrinkage and hole-shifts, from a fabrication point of view lattice shifts are more precisely implemented than individual hole-size shrinkage, and this empirical fact guides cavity-design selection.

A similar tuning process can be done in the case of L1 cavities by shrinking and shifting the holes nearest to the spacer. Table 2.3 shows the $\vec{H}_z(\vec{r})$ fields, and the electric-field energy densities $\epsilon(\vec{r})|\vec{E}(\vec{r})|^2$ in the principle symmetry planes of the cavities, along with a summary of the cavity parameters for L3 and L1 cavities.

### 2.3.3   1D Nanobeam Cavities

Extending the collinear-hole geometries considered earlier in the chapter (see Figure 2.12) to have a finite extent in the $z$-direction leads to "air-bridge" or 1D nanobeam cavities. As demonstrated earlier, tapering the mirror section increases reflectivity. Further, by smoothly tapering the hole radius and corresponding lattice-constant from the mirror to the waveguide section results in a very high $Q$, in excess of $1,000,000$. As an example [43], reducing the radius and pitch in steps of 2% in a beam(width $a$ and height $0.7\,a$) from a value of radius$= 0.30\,a$, lattice-constant$= a$ to a value of radius $= 0.86 \times 0.30\,a$, lattice-constant $= 0.86 \times a$, gave an ultrahigh-$Q$ of 1,142,268, and a mode

|  | L1 | L3 |
|---|---|---|
| $H_z(r)$ |  |  |
| $\epsilon_0\epsilon_r(r)|E(r)|^2$ |  |  |
| $\left(\frac{d}{a}, \frac{r}{a}, \frac{s}{a}, \frac{r'}{a}\right)$ | $(0.50, 0.35, 0.10, 0.25)$ | $(0.75, 0.30, 0.17, 0.30)$ |
| $\left(Q, \frac{a}{\lambda}, \frac{V}{(\lambda/n)^3}\right)$ | $(323740, 0.300, 0.422)$ | $(77899, 0.249, 0.368)$ |

Table 2.3: 3D FDTD simulations of L1 & L3 cavities. In all, $\epsilon_r = 12.605$.

volume of $0.27(\lambda/n)^3$ at a frequency $a/\lambda = 0.263$. The simulated cavity fields and intensities are shown in Figure 2.15.

There are several useful qualities of these cavities that will now be listed.

- **Lithography** - The inherent simplicity of these cavities over their 2D and 3D photonic crystal counterparts translates into a greater robustness against lithography errors. Since the number of holes required to define a 1D nanobeam is roughly the square root of the number in the 2D case, the lithography-errors also scale similarly, leading to a greater fabrication robustness. Another immediate consequence is a reduction in electron-beam (e-beam) lithography time[10].

- **Presence of a TM band-gap** - As recently discovered [47], increasing the slab thickness to be greater than the width leads to the creation of a TM band-gap, which has an overlap with

---

[10]The use of negative e-beam resists (exposed areas don't get developed away) might be advantageous in this case.
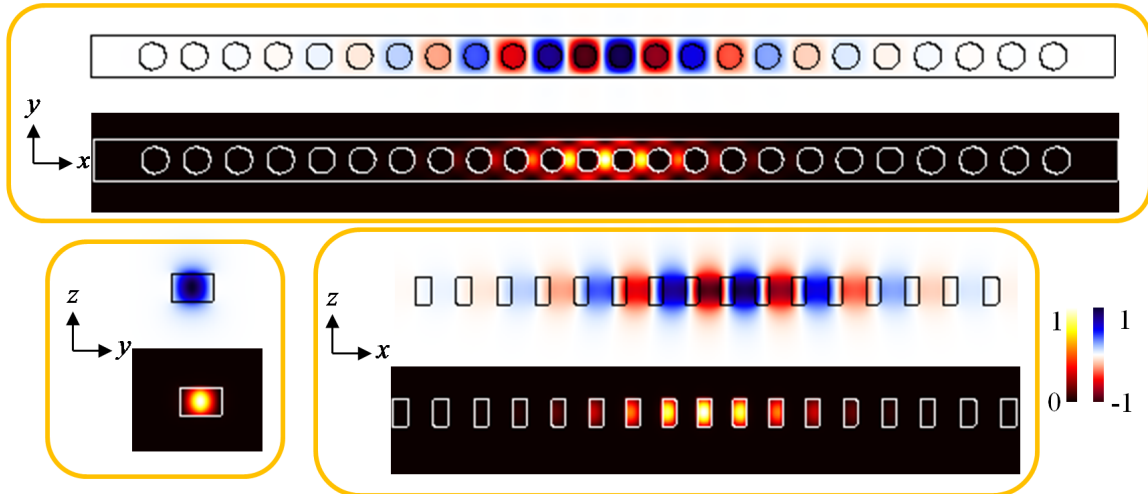
Figure 2.15: 3D FDTD simulations of a 1D nanobeam cavity (width $a$, height $0.7\,a$, $\epsilon_r = 12.605$). In each pane, the top half shows $H_z(r)$, and bottom half $\epsilon_0\epsilon_r(r)|E(r)|^2$.

the TE band-gap. Based on this principle, it was demonstrated that the same structure can have a TE *and* TM polarized mode, each of which has a $Q$ in excess of a million. This presence of an overlapping TE-TM band-gap is not found in the (2D) case of a triangular lattice of air holes. The practical consequences of this can be quite profound, as any non-verticality in the hole or beam sidewalls can lead to a coupling between TE and TM polarized modes, and a confinement of the TM mode can mitigate the drop in $Q$ due to this TE-TM coupling. This issue is revisited in Chapter 4.2.3.

- **High $Q$ with substrate** - These cavities retain a high $Q$ even when supported on a low-index substrate. Typical configurations involve GaAs-on-sapphire or silicon-on-insulator (SOI). Simulations indicate that $Q$s in excess of $50,000$ can be expected in these configurations. In our experiments, $Q$s as high as $75,000$ around $\lambda = 1.5\mu m$ in SOI have been experimentally observed. Further details are provided in Chapter 6.2.2.

- **High $Q$ with substrate & metal** - Simulations reveal that the cavities show modestly high $Q$s ($\approx 58,000$) when the beam top surface is coated with thin ($\approx 100$ nm) gold films on either side of the cavity region. The immediate application of such a result is in the electrical tuning of QD transitions (Stark shifting), and the construction of electrically-pumped lasers (taken up in Chapter 6.1).

- **Applications to opto-mechanics** - Given the picogram mass scale of these devices, it has become possible to probe [48] the opto-mechanical coupling effects of these cavities in the quantum regime, allowing the study of fundamental questions in quantum mechanics previously confined to gedanken experiments.

To summarize, given all the excellent properties offered by such cavities it is very likely that they will become the cavity-of-choice for a variety of applications, ranging from cavity QED to electrically-pumped lasers.

# Chapter 3

# Light Trapping Structures - Fabrication

## 3.1 Device Stack

Gallium arsenide (GaAs) wafers are typically grown by molecular-beam-epitaxy (MBE) or metal-organic-chemical-vapor-deposition (MOCVD). In MBE, epitaxial growth happens in ultra-high ($\approx$ $10^{-8}$ Pa) vacuum, where pure sources of the constituent alloy-elements are heated in effusion cells, allowing their sublimation and eventual condensation on the wafer surface where they react. In contrast, MOCVD growth happens not in vacuum, but in a gas phase at higher pressures ($<$ 100 kPa), and epitaxial growth happens due to chemical reactions between metalorganics and metal hydrides that contain the elements of the alloy. The crystal quality is fairly comparable between the two methods.
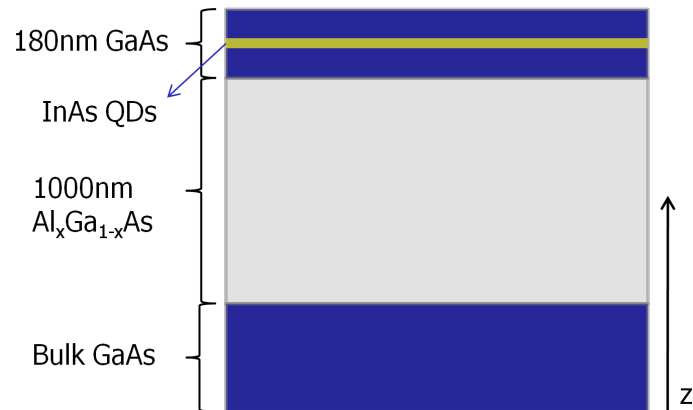


Figure 3.1: Schematic showing wafer cross-section, and typical layer compositions and thicknesses.

The GaAs devices fabricated in this thesis were grown by MBE[1]. Starting with a blank (001)

---

[1] Most samples used in this thesis were grown using a Riber 32 MBE machine by Hyatt Gibbs and Galina Khitrova at the University of Arizona.

oriented GaAs wafer, a 300 nm GaAs buffer is grown, followed by a 1-$\mu m$-thick sacrificial layer of the type $Al_xGa_{1-x}As$ (with $0.7 \leq x \leq 0.94$), a 90 nm GaAs bottom slab, an atomic monolayer thick InAs wetting layer on which InAs QDs are formed (induced by strain), and finally a 90 nm GaAs top slab. See Figure 3.1 for the wafer cross-section.
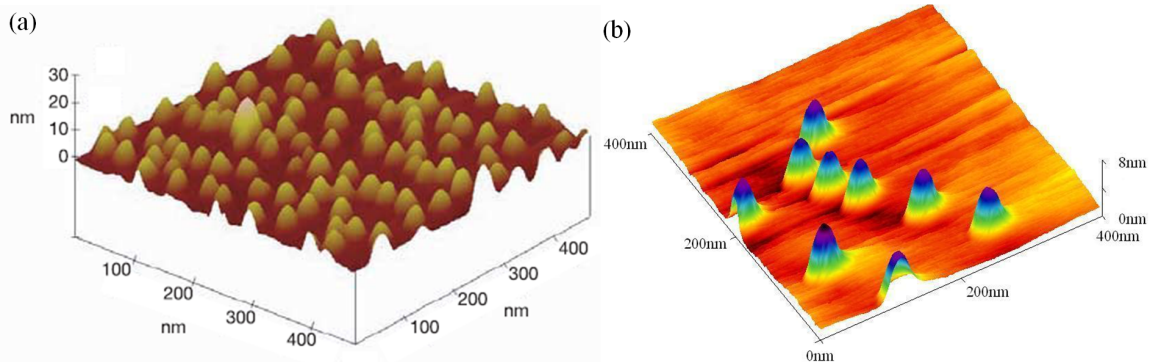


Figure 3.2: Atomic force microscope images of QD layers: (a) high density, and (b) low density. (Credits: Benjamin Richards.)

In Chapter 1.3, it was briefly mentioned that the QD transition frequencies are size dependent. This notion is now elaborated upon. It must be noted that in the above described wafer growth scheme, QD formation is strain induced and happens in the Stranski-Krastonow mode (strain $\approx$ 7%) [49], where 3D islands grow on a 2D wetting layer. The resulting InAs QDs have a spatially probabilistic distribution, i.e., they are scattered randomly over the wafer surface. Figure 3.2 shows atomic force microscope (AFM) scans of samples whose growth was stopped after QD formation (i.e. , without the top GaAs slab). Further, minute variations in QD dimensions across the wafer give rise to a spectral distribution of emission wavelengths, typically a 5% spread about a 1 $\mu m$ central wavelength. This can be seen by the spread of the QD ensemble in the photoluminescence (PL) spectrum, evident in Figure 3.3, that is obtained by above-band optical excitation of the QD layer.

## 3.2 Device Fabrication

Fabrication of photonic crystal cavities in GaAs involves the following steps: cleaning of the top of the grown GaAs wafer surface, spinning and baking of an electron-beam (e-beam) resist, e-beam lithography and subsequent resist development, pattern transfer into the substrate using a dry etch, removal of the underlying sacrificial layer by a suitable wet etch, and a final strip of the remnant resist. Reproducible device fabrication requires careful adherence to fabrication recipes (once established), and well maintained equipment. The fabrication sequence is shown schematically in Figure 3.4, and elaborated on subsequently.
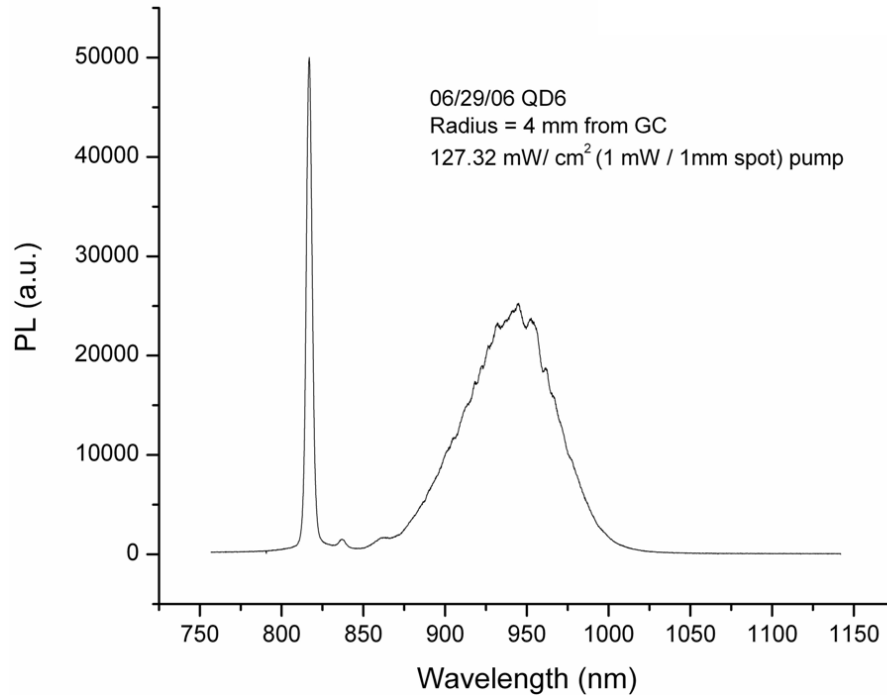
Figure 3.3: Ensemble QD photoluminescence (PL). The sharp peak around 820 nm corresponds to the GaAs band edge. Red-shifted from it is the QD ensemble centered at 950 nm with a width of $\approx$ 56 nm. (Credit: Joshua Hendrickson.)

### 3.2.1 Wafer Preparation

The very first step is the removal of any organic material that may have deposited on the top surface. A 5-minute agitated rinse in a solution containing equal amounts (by volume) of isopropyl alcohol (IPA), acetone, and trichloroethylene (TCE), followed by a rinse in pure IPA accomplishes this task. In addition, all semiconductor wafers tend to form a native oxide layer when exposed to the atmosphere. Removing this layer is important for resist adhesion, as well as ensuring a repeatable etch. In the case of GaAs, a 10-minute rinse in diluted hydrochloric acid (HCl) (1:1 = HCl:deionized water (DI) by volume) suffices for native oxide removal. After blow drying with $N_2$ gas and heating on a hot plate at 170°C for at least 10 minutes, the wafer is ready for the spinning on of a thin layer of resist.

### 3.2.2 Resist Application

Considerations of high resolution and ease of handling prompt the use of polymethyl meth-acrylate (PMMA) as the e-beam resist of choice. The disadvantage of this resist lies in its poor etch resistance, making it unsuitable for use in plasma etching machines. That said, the etch resistance in an ion beam etcher is good enough for its use as an etch mask. PMMA can withstand an aspect ratio of 3:1 (height:width) before becoming unstable. This trade-off between etch resistance (translating to
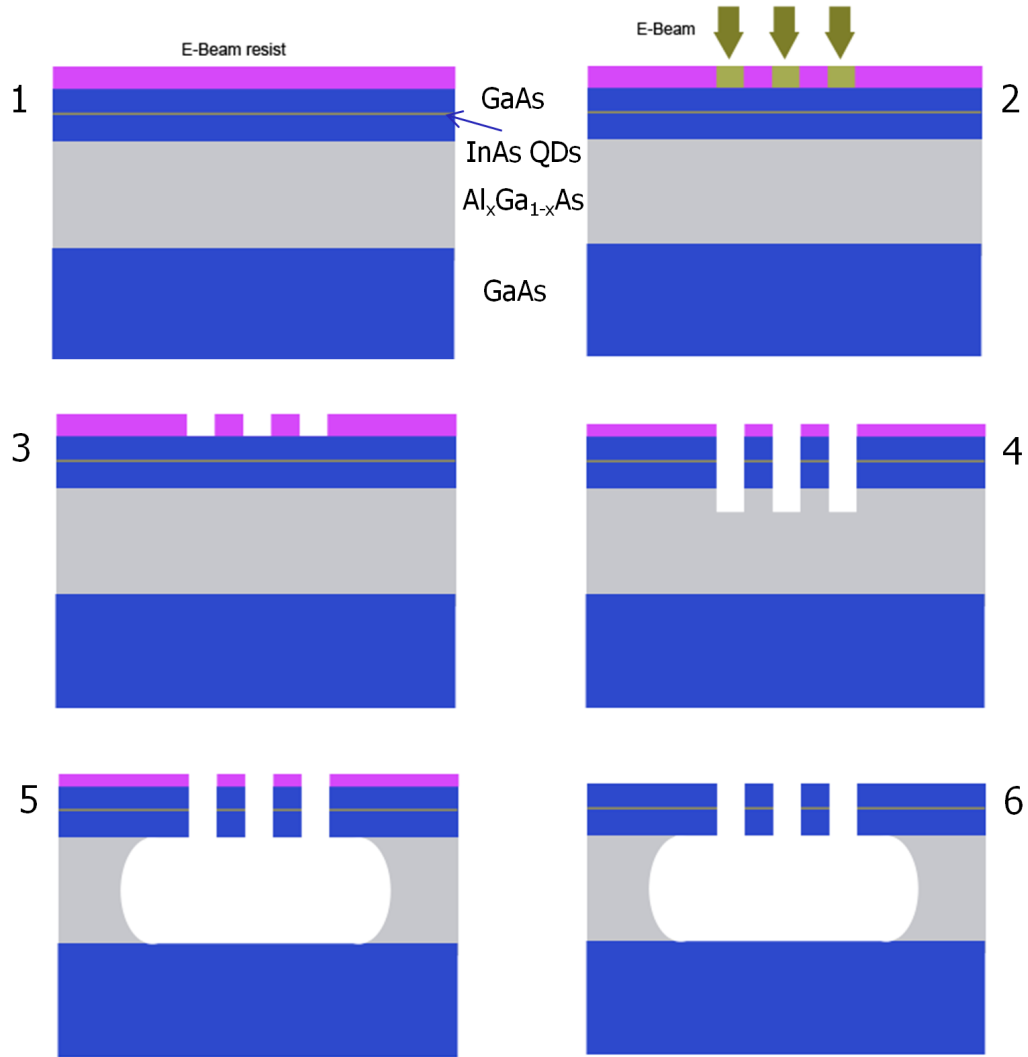
Figure 3.4: Fabrication sequence: (1) resist spinning, (2) e-beam exposure, (3) resist development, (4) dry etching, (5) wet etching to remove sacrificial layer, and (6) resist removal.

a thicker resist) and aspect ratio (translating to a thinner resist) leads to an optimal resist thickness of $\approx 150$ nm. High molecular weight PMMA (PMMA 950kA3) is put on a GaAs wafer (cooled to room temperature) and spun for 1 minute at 3500 rpm to get a resist thickness $\approx$ 140-150 nm.

The resist-coated wafer is immediately placed on a hot plate at $170°$C and baked for 30 minutes. While it is possible to bake at a higher temperature for shorter time periods[2], it is empirically found that longer bakes result in more uniform pattern transfer to wafer.

---

[2]For instance, the manufacturer's notes recommend baking at $180°$C for 2 minutes.

### 3.2.3 Lithography

Electron-beam lithography is then performed using a Vistec Electron-Beam-Pattern-Generator (EBPG)-5000+ 100 keV machine that is able to expose the device masks at a resolution of 2.5 nm. Employing a low beam-current in the region of 600–800 pA and an e-beam dose of 850–950 $\mu$C/cm$^2$ accomplishes the proper exposure of the device masks. Of all the steps in the fabrication sequence, this step has presented the maximum degree of variability and, as a result, considerable effort was invested in identifying and addressing the issues. These are now highlighted.

1. **Height reading** - The EBPG uses a laser to reflect off the wafer surface in order to register the surface height. For small wafer sizes ( $<$ 1 cm on a side), it often happens that the laser does not register a height. As a result, the e-beam focus is improper and exposed features can deviate significantly from intended feature sizes. Figure 3.5 shows this effect in an etched structure, where larger features in the form of trenches around a cavity have received a sufficient dose to be defined, but the photonic crystal region is very poorly defined[3].

   There are two methods to overcome this problem. In the first method, height meter readings from a few points on the wafer surface are used to create an interpolation table for the complete wafer (using the "height-map" utility in the EBPG). At the time of actual e-beam exposure, the laser is not used to read the height, instead, the interpolation table is looked up. This method relies on that fact that there are at least three points on the wafer over which an actual height reading registers. In the event that this doesn't work, the evaporation of a thin ($\approx$ 10 nm) gold layer on top of the e-beam resist layer usually helps the laser to register a height. After lithography, the gold layer can be easily removed by rinsing the wafer in a potassium-iodide (KI) solution for 30 seconds. A recent hardware upgrade has resolved this issue, and height is measured without taking recourse to an interpolation table, or a thin gold film.

2. **Proximity Effect and Feature Overlap** - During lithography, an e-beam isn't contained within an area intended for exposure. Forward scattering (due to electron-electron interactions within the beam) and backward scattering (by the substrate below the resist) widens the e-beam, and as a result proximate features tend to get an additional e-beam exposure. In the worst case, this leads to the merging of relatively close features (see Figure 3.7). This effect is compounded by an e-beam that is defocused. Proximity-effect-correction (PEC) is accomplished by employing Monte Carlo simulation methods that compute electron trajectories (for several million electrons at a time) for a given accelerating voltage and wafer stack, and can be used to adjust dosing for proper exposure. Empirically, it is found that for photonic crystal lattice constants less than 250 nm (and for $r/a$ $<$0.35), it is necessary to apply PEC

---

[3]Also, as seen in Figure 3.6, the EBPG occasionally produces completely random errors.
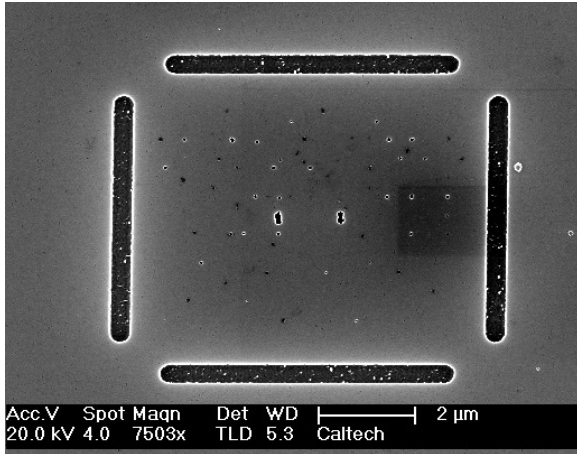
Figure 3.5: Scanning electron microscope image showing effects of a defocussed e-beam. Larger features are developed, but the photonic crystal intended to be inside the larger features is barely defined.
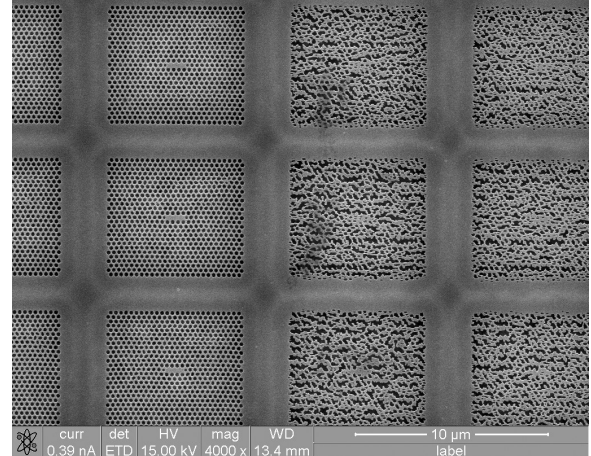


Figure 3.6: Scanning electron microscope image showing random EBPG errors: compare devices on left and right.

when using a 100 keV e-beam on a 150 nm PMMA/GaAs wafer. For larger lattice constants, it suffices to shrink mask features by a small amount to get optimal exposure[4].
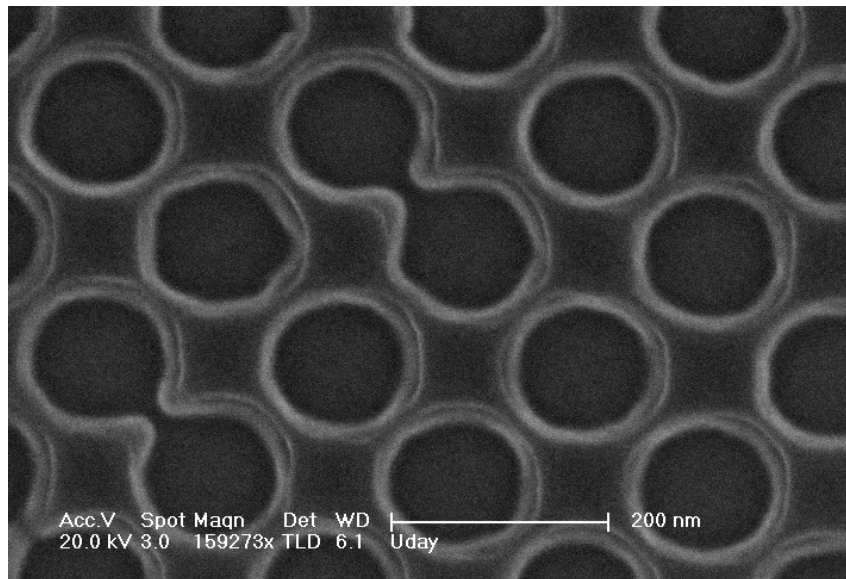


Figure 3.7: Scanning electron microscope image showing proximity effects leading to merged holes.

---

[4]This shrinkage amount is empirically determined, and depends on the resist type, thickness, and preparation method.

### 3.2.4  Resist Development

For proper pattern-transfer to substrate, it is crucial that the developed resist sidewalls be vertical. Non-vertical resist sidewalls arise from a combination of excess e-beam dose, and inadequate/excess resist development time. Figure 3.8 shows a SEM image of non-vertical resist sidewalls. Two different resist developers that were used for developing 950K PMMA A3 resist are:

1. 3:7=2-ethoxy-ethanone:methanol (by volume) for 12 s, followed by a rinse in IPA for 30 s, and a gentle $N_2$ blow dry. Care must be taken to prepare a fresh batch each time[5].

2. 1:3=methyl-iso-butyl-ketone(MIBK):IPA for 1 min, followed by a rinse in IPA for 30 s, and a gentle $N_2$ blow dry.
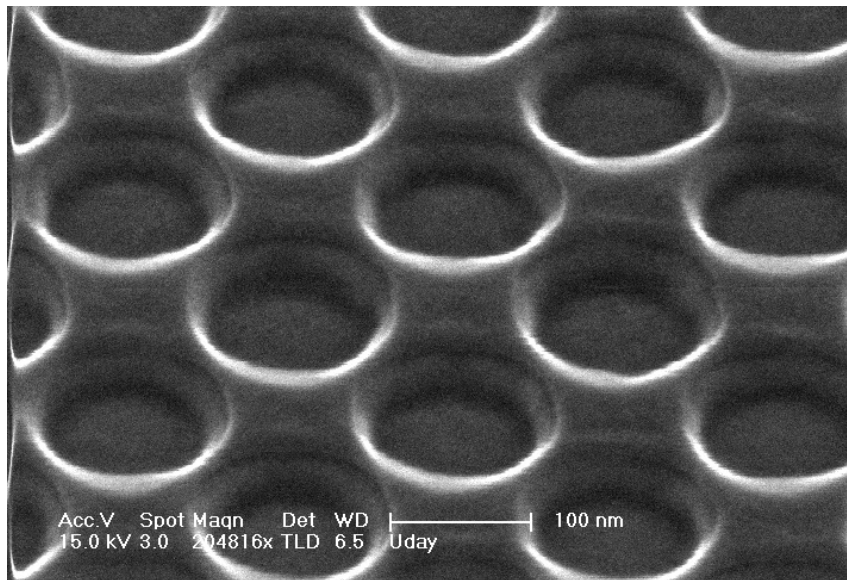


Figure 3.8: Non-vertical resist sidewalls (developed using 2-ethoxy-ethanone-based developer), as seen in a tilted SEM image.

Repeatability and uniformity was found to be much better with the MIBK-based developer.

### 3.2.5  Dry Etching

Gallium aresenide is dry etched in a chemically-assisted-ion-beam-etching (CAIBE) machine. The machine uses a Kaufman ion source that ionizes Ar gas, and then accelerates the ionized Ar atoms toward the sample. This constitutes the physical component of etch. $Cl_2$ gas is injected just above the sample and its chemical reactions with the sample ($Cl_2$ forms volatile chlorides with Ga and As atoms) in the region of ion bombardment increases the etch rate and anisotropy. Figure 3.9 shows the pale blue hue of an Ar ion beam with injected $Cl_2$ gas in the vacuum chamber.

[5]Due to the highly toxic nature of 2-ethoxy-ethanone, a full-face shield and double-gloving must be used while handling this developer.
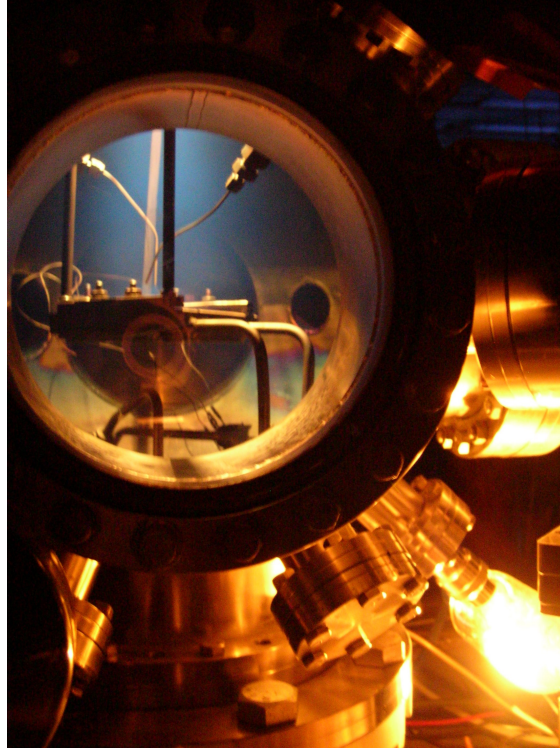
Figure 3.9: View of CAIBE vacuum chamber with Ar ion beam and $Cl_2$ gas (blue haze in image top left).

The $Cl_2$ flow rate and nozzle orientation can greatly alter the etch profile. Polymer beads of diameters $\approx$ 350–500 nm provide the most convenient etch masks for calibration of the GaAs dry etch in the CAIBE. The dynamics of a "bead" etch is different from a "hole" etch, since in the former there are vast areas that are open and etched away, while in the latter only a small exposed area is etched away. The rate of formation of etch by-products will be different in both cases. At the same time, an asymmetric etch with beads is not likely to become symmetric with holes. The issue of symmetry comes in because $Cl_2$ gas is introduced via a jet, and depending on the angle at which the flow impacts the substrate, an asymmetry can be introduced into the etch. Empirically, it is observed that a "hole" etch is less non-vertical than a "bead" etch. Therefore, optimizing the CAIBE conditions for a symmetric, vertical etch with beads provides an efficient technique for improving the etched hole sidewalls (see Figure 3.10). It is found that

1. Control of the angle of $Cl_2$ flow controls etch symmetry;

2. Etch verticality is controlled by adjusting the $Cl_2$ flow rate.

Appendix A.1 contains details of the etch recipe.
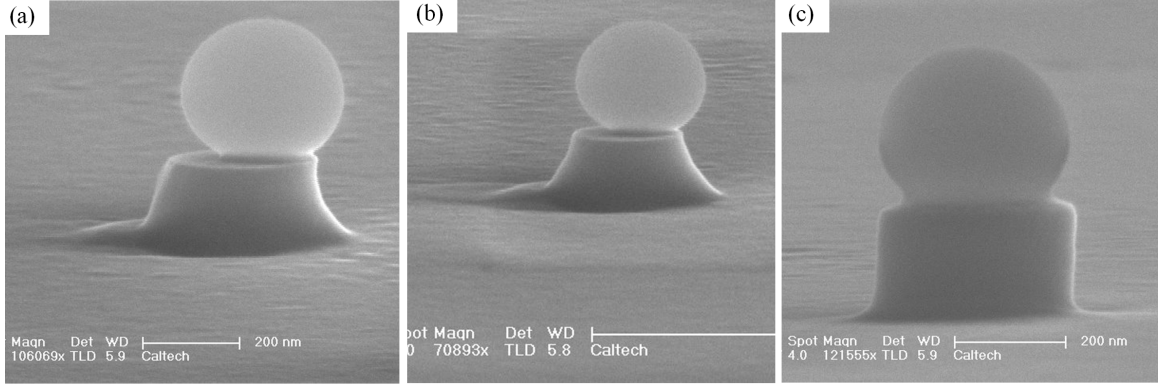
Figure 3.10: Scanning electron microscope images showing: (a) asymmetric CAIBE etch due to non-vertical $Cl_2$ flow, (b) non-vertical CAIBE etch due to insufficient $Cl_2$ flow, and (c) symmetric, vertical CAIBE etch by repositioning $Cl_2$ nozzle and increasing flow.

## 3.2.6 Wet Etching

To make air-suspended structures, it is necessary to remove the sacrificial $Al_xGa_{1-x}As$ layer below the GaAs layer. The method of removal depends on $x$, the AlAs concentration in the alloy. All devices fabricated for this thesis have had one of these two Al concentrations

1. **$x = 0.94$** - In this case, sacrificial layer removal proceeds through the oxidation of Al in a steam furnace, followed by a wet etch in a potassium hydroxide (KOH) solution. The mechanism of oxidation is as follows [50]:

$$
\begin{aligned}
2AlAs + 3H_2O_{(g)} &= Al_2O_3 + 2AsH_3 \\
2AlAs + 4H_2O_{(g)} &= 2AlO(OH) + 2AsH_3 \\
2AsH_3 &= 2As + 3H_2 \\
\underline{2AsH_3 + 3H_2O = As_2O_{3\,l} + 6H_2} & \\
2AlAs + 3H_2O_{(g)} &= Al_2O_3 + 2As + 3H_2 \\
2AlAs + 4H_2O_{(g)} &= 2AlO(OH) + 2As + 3H_2
\end{aligned}
\tag{3.1}
$$
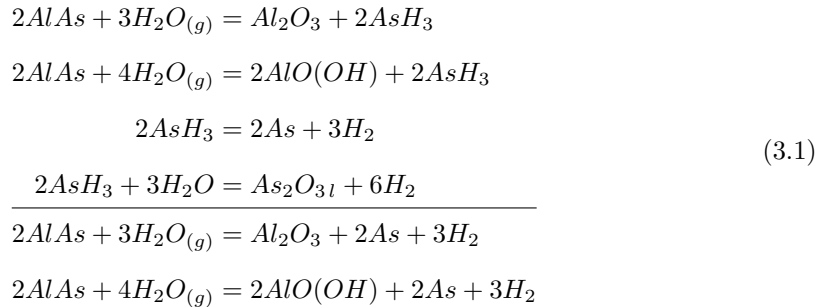
The wafer is placed in a furnace whose temperature is set at $460°C$. Steam is generated from an attached bubbler that contains heated water at $95°C$, and an immersed tube through which $N_2$ gas is passed at a flow rate of 4 sccm. Under these conditions, it is found that Al oxidation occurs at a lateral rate of $\approx 200$ nm/min.

Immediately after the oxidation step, the wafer is wet etched by immersing in a KOH solution[6] (25 g KOH / 100 ml DI water) for 1 min, followed by a rinse in DI water for 1 min, and finally

---

[6]The solution must be prepared several hours before use, to allow for complete dissolution of KOH crystals.

a dip in IPA for 30 s. After the wafer is removed from the IPA solution, it is very important to not blow-dry the wafer, as this can collapse the mechanically fragile slabs. Tilting the wafer slightly, and allowing the IPA to evaporate (within the fume hood), is an effective method of drying the wafer[7]

Figure 3.11 shows steam oxidation and wet etching on a calibration pattern of rectangular slabs inside a larger trench. Translucent regions represent GaAs layers that have been undercut, whereas a central post supporting the slab appears white.
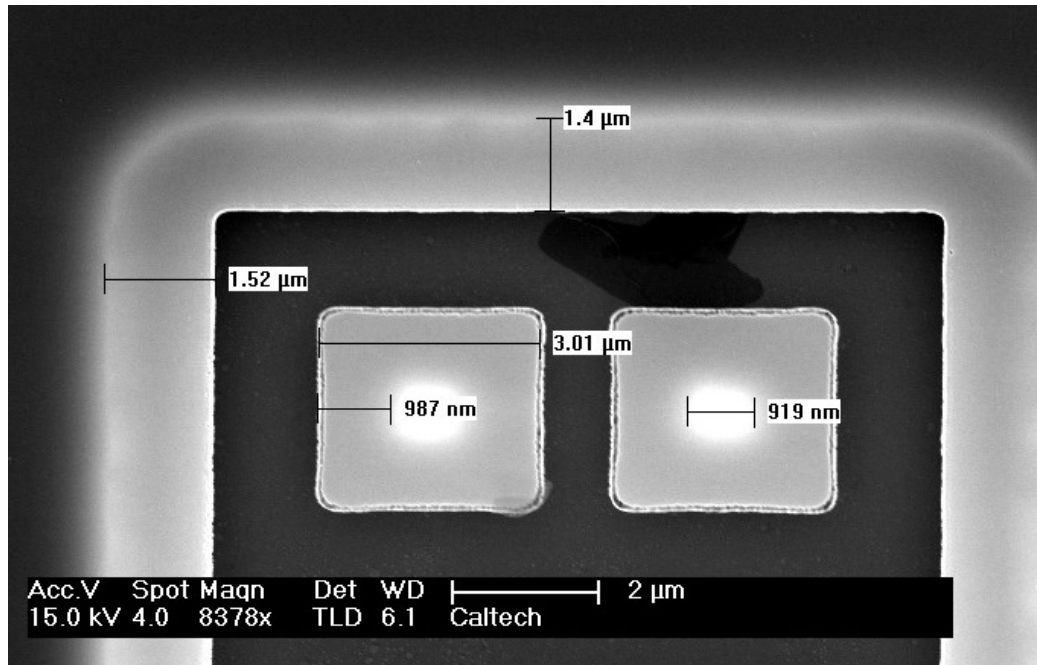


Figure 3.11: Scanning electron microscope image of steam oxidized and wet-etched calibration patterns.

2. $x = 0.70$ - For sacrificial layers with this composition, an intermediate steam-oxidation step is not required, and the wet etch is accomplished by immersing the wafer in a hydrofluoric (HF) acid[8] solution (1:10 = HF:DI water (by volume)) for 1 min, followed by a rinse in DI water for 1 min, and an IPA dip for 30 s. Like before, it is important to not blow-dry the wafer at this point.

Exposure to atmosphere $O_2$ leads to the immediate formation of a native oxide layer, and for reproducible fabrication it is extremely important for there to be as little time lag as possible between the dry- and wet- etching steps.

---

[7]Critical-point drying is a more sophisticated method of accomplishing the same, but was found to be unnecessary in this case.

[8]HF is a very dangerous acid capable of eating away bone material before detection, and extreme care must be exercised in its use and disposal.

### 3.2.7 Resist Removal

Remnant resist is stripped in two steps. In the first step, the sample is immersed (and agitated) in a series of solutions for several minutes. Starting with an equal mixture (by volume) of IPA and acetone, the wafer is transfered to a solution containing equal amounts (by volume) of IPA, acetone, and TCE, before being rinsed in an IPA solution. This step helps remove most of the resist, except for regions near the photonic crystal holes that have been hardened by ion-beam bombardment. Figure 3.12 shows remnant resist that has survived chemical treatment.
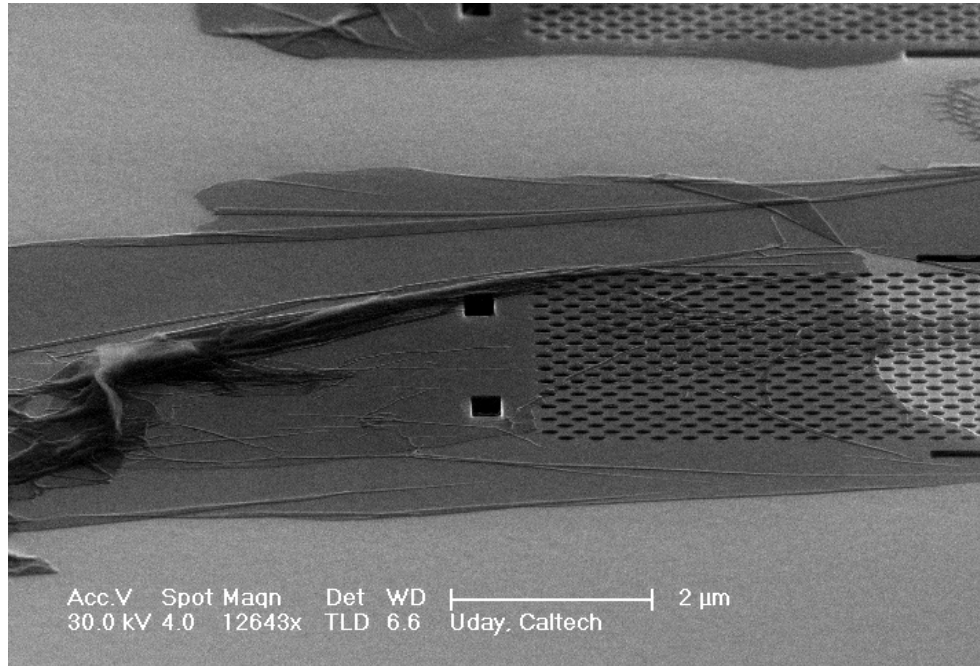


Figure 3.12: Scanning electron microscope image of a tilted L3 cavity showing remnant resist (dark, wrinkled features) after chemical treatment.

The final step, which completely removes the resist, involves using an $O_2$ plasma in an Oxford Instruments inductively coupled plasma – reactive ion etching (ICP-RIE) 180 machine. See Appendix A.2 for details on the etch recipe. Figure 3.13 shows a fully fabricated L1 cavity from which resist has been completely stripped.

### 3.2.8 Subtleties

It might be argued that the steps of wet etching and resist removal are interchangeable, and that given the mechanical fragility of the air-suspended slabs, it might be better for resist removal *before* wet etching. However, two separate physical mechanisms deposit material on top of the resist layer. These are:

1. The by-products of dry etching get deposited on the inside and top of the resist sidewalls.
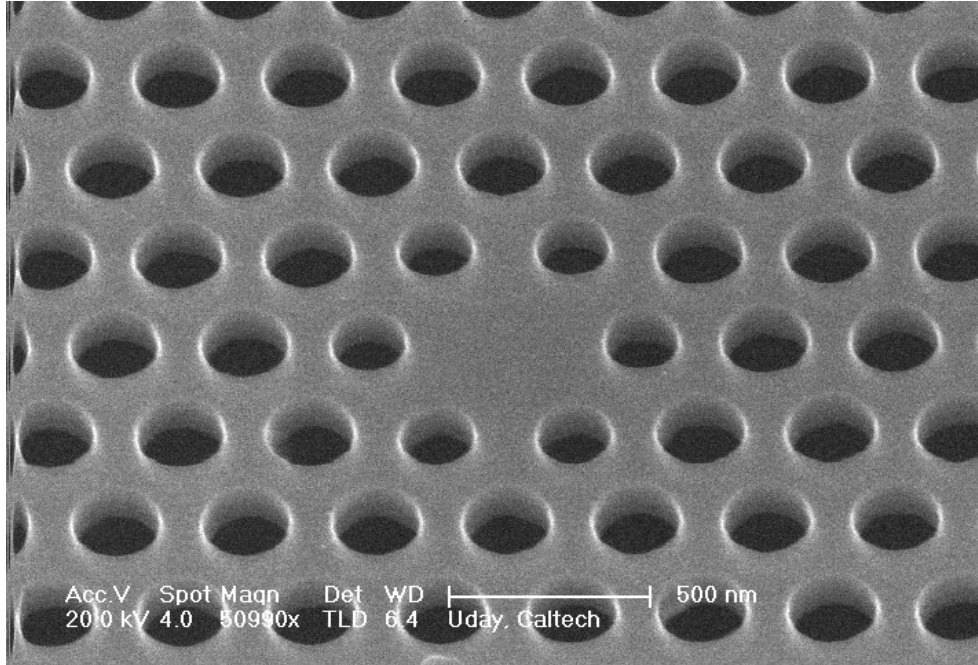
Figure 3.13: Scanning electron microscope image of fully fabricated L1 photonic crystal cavity imaged at a 30° tilt.

2. During the wet etching with HF, hydroxides of Al formed from the AlGaAs layer float in the solution and get deposited on top of the resist.

As is detailed in Chapter 4.2.2, a cleaning process involving rinsing the sample in a KOH solution was found [51] to be effective in removing the latter type of debris. However, this step can be altogether avoided by keeping the resist layer till *after* the wet etching step. In the first step of resist removal, the wafer is agitated in various chemical solutions, and the debris that has deposited on top is removed along with the resist layer. The final resist strip using an oxygen plasma thus leaves a surface free of all debris.

# Chapter 4

# Light Trapping Structures - Experiment

Having illustrated the theory and fabrication of photonic crystal cavities, a description of experimentally determined cavity-$Q$s is presented, followed by an analysis of the various factors that have been found [52] to degrade cavity-$Q$.

## 4.1    Cavity-$Q$ Measurement

Once device fabrication is complete, the measurement setup and sequence is as follows; fabricated devices are placed in an evacuated liquid helium cryostat, cooled down to approximately 10 K and excited non-resonantly by a Ti:sapphire laser operating at 780 nm with an output power in the range of 2-500 $\mu$W. Photoluminescence (PL) from excited cavities is collected by a (36$\times$) microscope objective, passed through a spectrometer, and recorded on either a Si detector (for wavelengths $< 1\mu$m) or an InGaAs detector (for wavelengths $> 1\,\mu$m).

On any given fabrication run, several photonic crystal cavity parameters (lattice constant, air hole radius/shifts) are varied, along with e-beam dosage. These techniques vary the cavity-$Q$ and wavelength, and help scan through the QD ensemble. The photonic band-gap of the device manifests itself in the suppression of the QD ensemble PL. This is seen graphically in Figure 4.1 by comparing the top and bottom panes. The bottom pane shows the QD ensemble PL in the absence of a photonic crystal. With the introduction of the photonic crystal cavities, only the different cavity modes stand out over a relatively flat QD ensemble PL. Figure 4.2 shows a zoomed-in PL spectrum observed from a high $Q$ cavity, where a Lorentzian fit is used to calculate the $Q$ by the following relation, $Q = \lambda_0/\Delta\lambda$, where $\lambda_0$, $\Delta\lambda$ represent the center and full-width-at-half-maximum (FWHM), respectively, of the Lorentzian fit.

| | a (nm) | Q (approx) |
|---|---|---|
| | 250 | 8,400 |
| | 260 | 3,800 |
| | 270 | 9,100 |
| | 280 | 7,800 |
| | 290 | 11,600 |
| | 300 | 13,800 |
| | 310 | 8,800 |
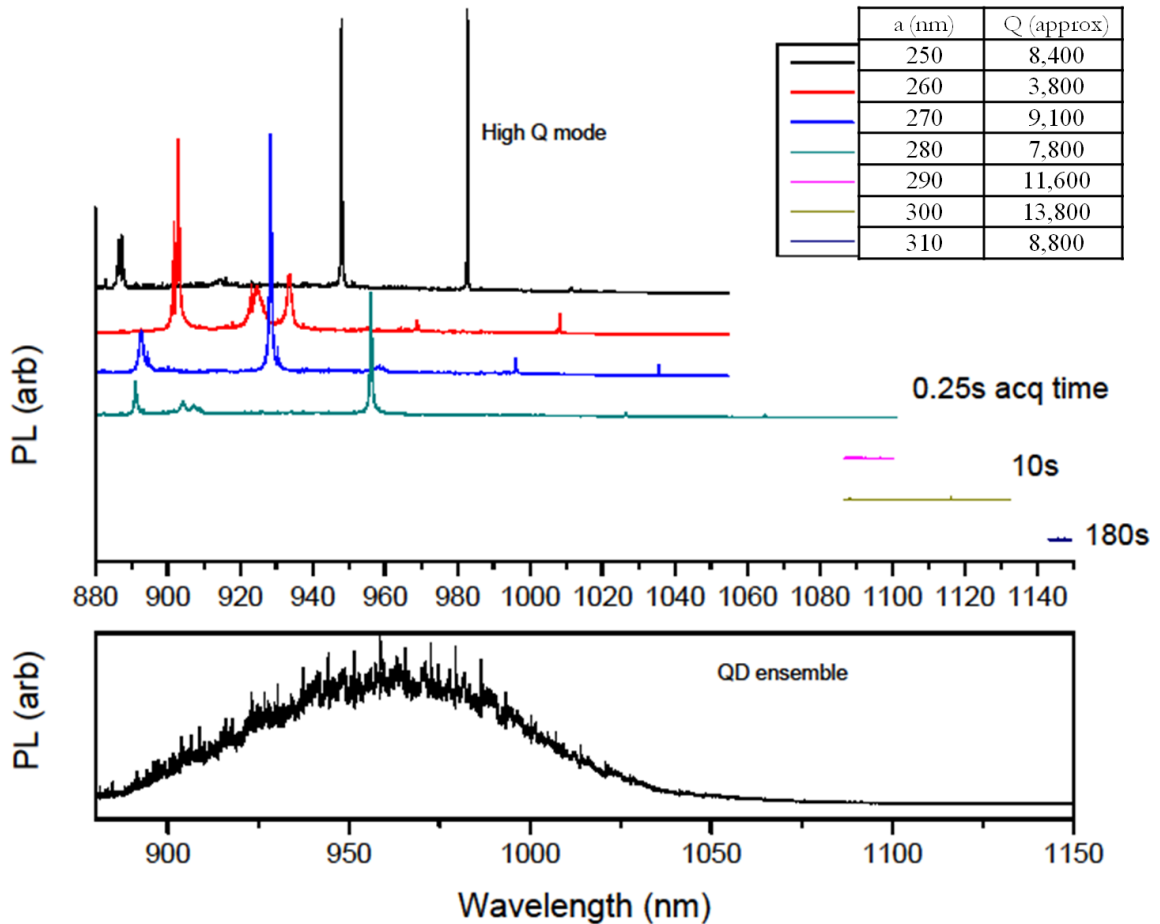
Figure 4.1: (Top) PL spectra showing cavity wavelength tuning by lattice-constant tuning (values shown in top right box). (Bottom) PL spectra showing QD ensemble from a region on the wafer having no photonic crystals.

## 4.2   Q-Degrading Mechanisms

Through careful $Q$ measurements on a large number ($> 10,000$) of fabricated devices, it is found that the measured $Q$s are not as high as computed, even though SEM images of fabricated devices look nearly perfect in many aspects such as sidewall roughness and circularity of holes (see Figure 3.13 for an example). It is therefore important to understand the loss mechanisms that degrade cavity-$Q$.

Cavity-$Q$ can be decomposed in terms of the following loss mechanisms [53]:

$$Q^{-1} = Q_{rad}^{-1} + Q_{mat}^{-1} \tag{4.1}$$

where $Q_{rad}^{-1}$ indicates the optical loss from the cavity by coupling to radiation modes in vacuum/substrate, and $Q_{mat}^{-1}$ represents a combination of the intrinsic loss in the material, the loss
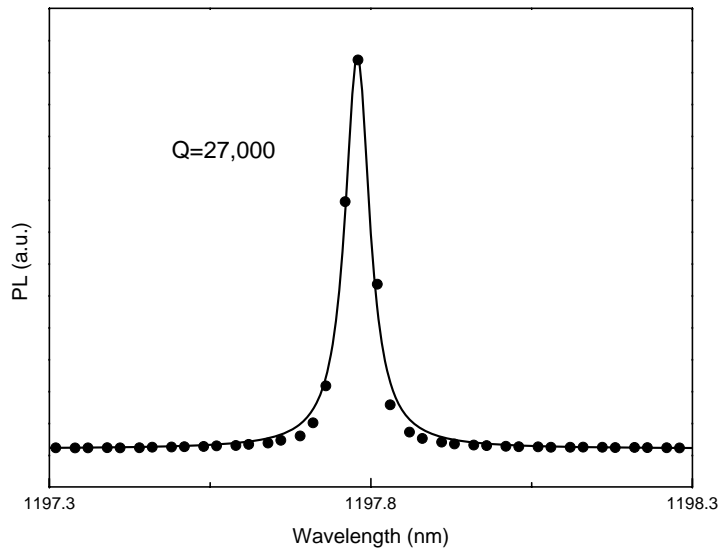
Figure 4.2: Photoluminescence from a photonic crystal cavity showing a Lorentzian fit to the data for the highest cavity-$Q$ (27,000) recorded for devices in this thesis.

due to the formation of surface states that inevitably result from the oxygen termination of broken, dangling GaAs bonds at the etched interfaces, and any gain or loss [54] that might occur due to QD absorption in the cavity's spectral and spatial neighborhood. $Q_{rad}^{-1}$ can be further divided into two terms, $Q_0^{-1}$ and $Q_{scat}^{-1}$, where $Q_0^{-1}$ indicates the intrinsic radiation loss in the absence of any fabrication related errors, while $Q_{scat}^{-1}$ indicates the loss due to (Rayleigh) scattering from surface imperfections introduced during MBE growth and device fabrication.

The loss represented by $Q_{mat}^{-1}$ is strongly wavelength dependent. On one hand, GaAs shows increased loss [53] due to (sub-band-gap) surface states as one approaches the GaAs band edge at $\approx 814$ nm (at 10 K). Simultaneously, at wavelengths close to and lower than the QD ensemble peak (typically between 950-1100 nm), absorption by the QDs and the wetting layer[1] further degrades $Q$ from the "empty" (no QDs) cavity-$Q$ [54]. Both these effects, along with a $1/\lambda^4$ dependence of scattering loss is supported [51] in a cavity-$Q$ versus $\lambda$ plot, as seen in Figure 4.3. While the data is noisy and doesn't uniquely support any particular fit, a general trend of a decrease in $Q$ with wavelength is seen, consistent with the loss mechanisms outlined above. The following subsections will be devoted to discussions of possible factors limiting $Q$ based on practical considerations. To start with, fabrication-related failure modes that are fairly evident are presented, before moving on to $Q$-degrading factors that might not be obvious.

---

[1]As mentioned in Chapter 3.1, this is an atomic monolayer of InAs on which the QDs are formed.
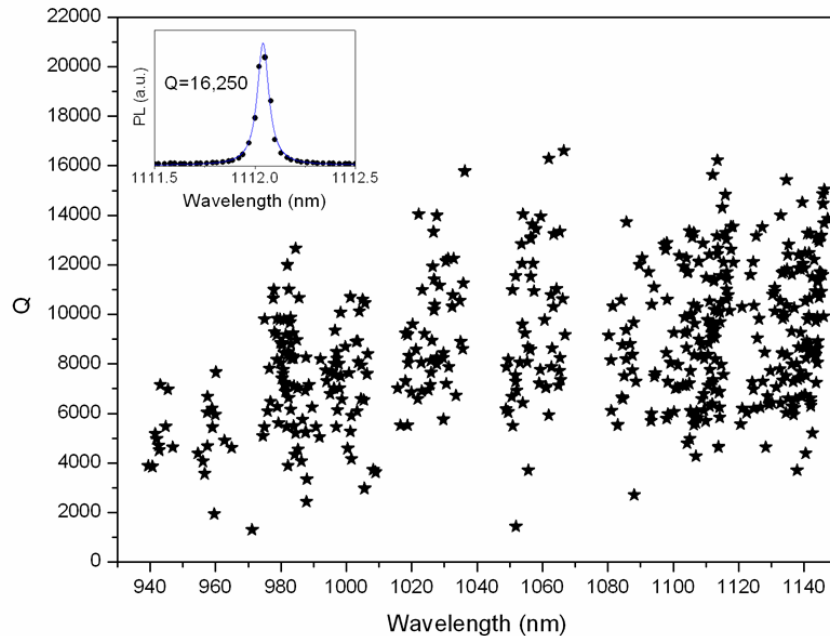
Figure 4.3: Variation of $Q$ as a function of $\lambda$. Inset shows PL spectra from a high-$Q$ cavity along with a Lorentzian fit.

## 4.2.1 Irregular Air Holes and Contour FDTD

The intrinsic radiation loss in the absence of any fabrication-related errors (represented by $Q_0^{-1}$) is minimized by a careful control of the cavity geometry, and in the case of L3 designs can be theoretically as high as 108,754 in GaAs (higher $Q$s have been reported with photonic crystal waveguide type designs [55, 56], but they are not considered here because of their higher mode volumes). Any irregularities in the lithography or etching, such as photonic crystal holes deviating from circular shapes, can severely degrade $Q_{rad}$. Unless carefully controlled, the lithography step[2] can lead to considerable lack of reproducibility.

Although the theoretical cavity-$Q$s can be as high as 108,754, less than a fourth of this number has been experimentally observed (see Figure 4.2). To investigate this discrepancy, 2D contour data extracted from the SEM image of a fabricated device for the purposes of $Q$ estimation is used.

Consider the particular case of a fabricated L3 cavity whose resonant wavelength and $Q$ are measured to be 1144.1 nm and 10,050, respectively. First, all the structural parameters (lattice constant, hole radius and shifts) characterizing the cavity are extracted from the corresponding scanning electron microscope (SEM) image[3]. 3 dimensional (3D) FDTD simulations based on these parameters reveal a resonant wavelength and $Q$ of 1129.7 nm and 31,418, respectively. Clearly, $Q$

---

[2]See Chapter 3.2.3 for further details on lithography.
[3]It should be noted that there can be $\sim \pm 5\%$ error in the SEM scale.

values estimated in this way differ significantly from the measured $Q$.
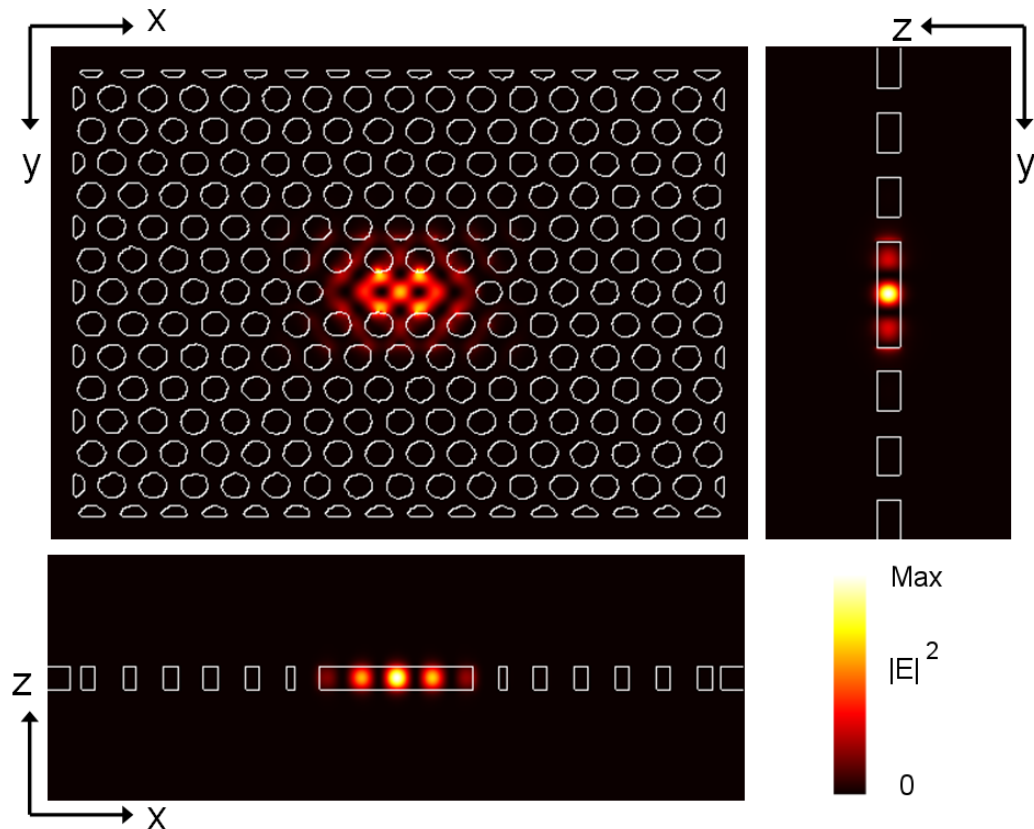


Figure 4.4: Electric field energy density profiles from a contour FDTD simulation (contour data superimposed) for the three symmetry planes of the L3 photonic crystal cavity.

Instead, contour data that faithfully captures all the fabrication-related imperfections (instead of using averaged cavity parameters from the SEM image) can be employed in 3D FDTD simulations [57]. As is evident from Table 2.3, the electric field energy density $(\epsilon_0 \epsilon_r(\vec{r})|\vec{E}(\vec{r})|^2)$ of the L3 mode reveals strongly localized patterns around the four air holes nearest to the cavity center. Recalling the fact that the $Q$ of the L3 mode is highly sensitive to the fine tuning of the nearest air holes [44], even minute deviations from the ideal geometry can severely degrade $Q_{scat}$ and this can be quantified using contour FDTD. The extracted contour plot and simulated $\epsilon_0 \epsilon_r(\vec{r})|\vec{E}(\vec{r})|^2$ for the structure mentioned above are shown in Figure 4.4, in which a grid resolution of $\Delta x = \Delta y = \Delta z \approx 10$ nm is employed [34]. The $Q$ obtained in this way drops to $21,283$, which is still large but becomes closer to the measured value of 10,050. The remaining discrepancy can be attributed to non-vertical sidewalls, sidewall roughness, and material losses that cannot be easily incorporated in a contour FDTD simulation. Finally, for a more realistic $Q$ value, an air gap and GaAs substrate are included. The $Q$ value in the presence of an 800 nm air gap is 23,576, showing about 10% improvement in comparison with the structure without the air gap.

## 4.2.2   Remnant PMMA and Debris

A thin layer of resist, as seen in Figure 3.12, is often left behind even after chemical treatment for removal (Chapter 3.2.7 dealt with the issue of resist removal). Moreover [51], a fine layer of sub-micron-sized micro crystallites is sometimes left behind even after the completion of the wet etch and resist removal. Figure 4.5 shows this debris partially blocking some of the holes in the top left. An AFM scan (see Figure 4.6) confirmed the presence of this debris. On the hypothesis that the debris was composed of hydroxides of Al, the sample was rinsed in a KOH solution[4] (25 g/100 ml DI water) for 60 s, and the debris was found to have noticeably reduced. After rinsing for an additional 80 s in the solution, the debris was found to have completely gone, as seen in Figure 4.7. The effect [51] of the KOH cleaning on one particular cavity[5] was to improve the Q from 5,700 to 8,400, increase PL intensity substantially, and shift the cavity modes to higher energy by about 11 meV, as can be seen graphically in the PL spectra in Figure 4.8.
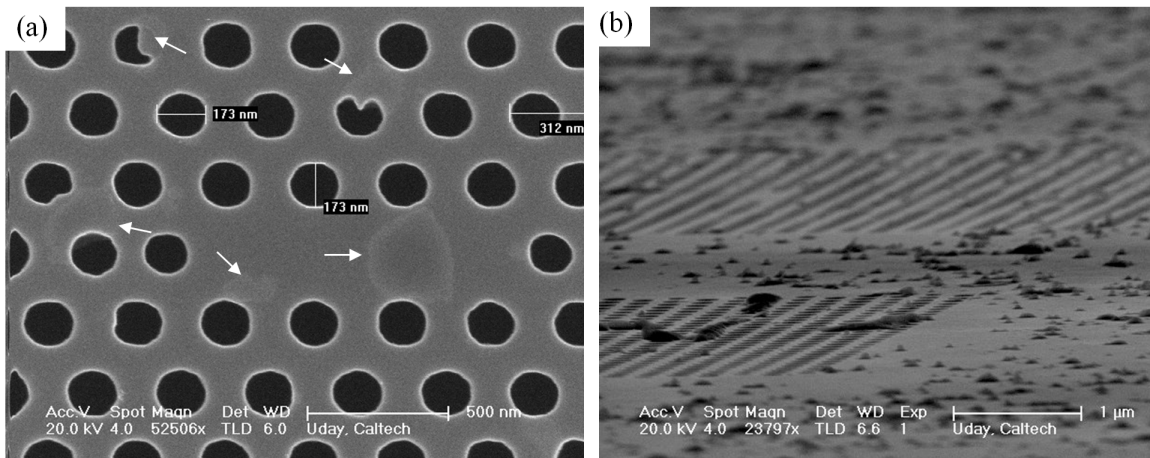


Figure 4.5: Scanning electron microscope images showing debris: (a) partly blocking some photonic crystal holes and cavity region (indicated by white arrows), and (b) in a tilted view. (Credits: Benjamin Richards.)

## 4.2.3   Non-vertical Sidewalls

Maintaining a vertical etch profile in the dry etch is also important. As explained in Chapter 2.2, the presence of mirror symmetry in the case of perfectly vertical sidewalls allows one to classify slab modes into even (TE-like) and odd (TM-like) symmetry modes. However, non-verticality of etched air holes breaks this symmetry, which results in new forms of hybridized modes that can no longer be classified as either TE-like or TM-like. A deviation from a vertical etch by even 2° can cause $Q_{rad}$ to drop by an order of magnitude [58] and this is due to the well known TE-TM coupling loss

---

[4]KOH etches aluminum hydroxide.
[5]Fabrication run A0961-3
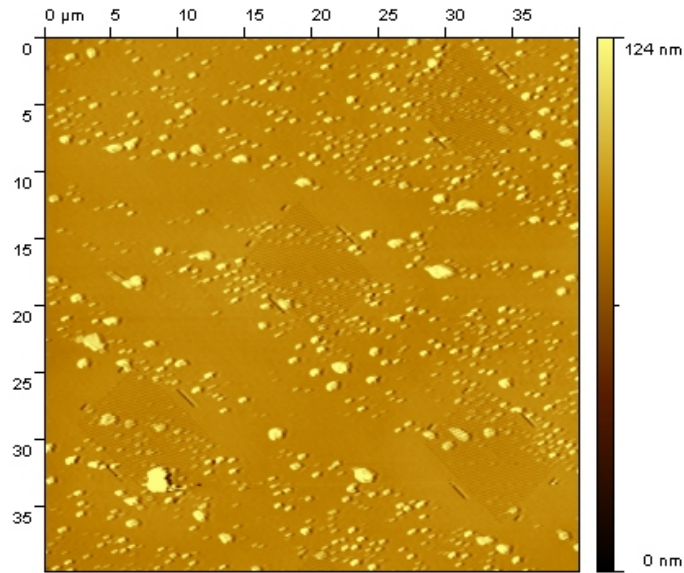
Figure 4.6: Atomic force microscope images confirming debris. The bright spots exceed 50 nm in height.(Credit: Benjamin Richards.)
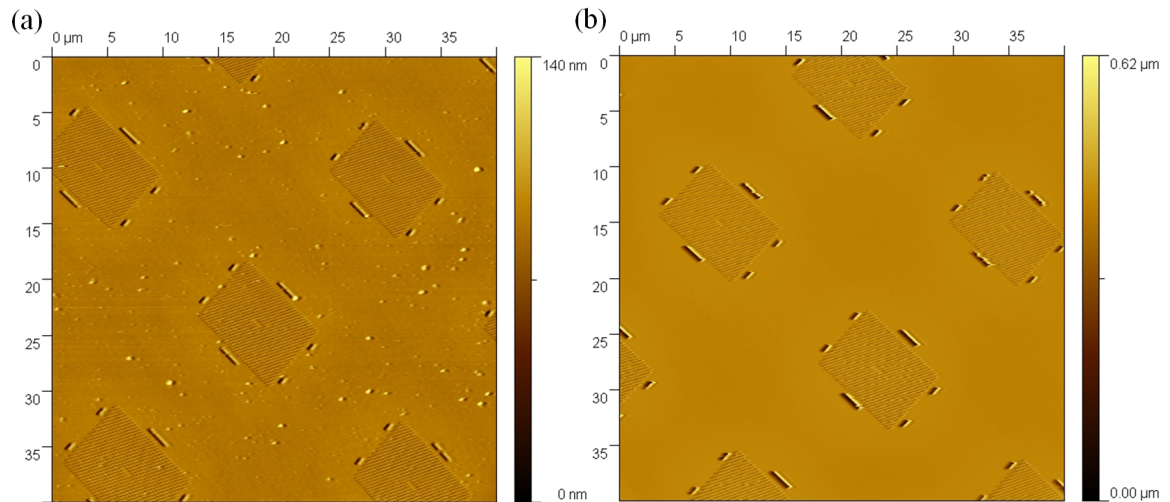


Figure 4.7: Atomic force microscope image showing debris elimination: (a) partially after a 60 s KOH rinse, and (b) completely after an additional 80 s KOH rinse. (Credits: Benjamin Richards.)

[59].

There are at least two factors that can cause non-vertical sidewalls. Firstly, inadequate or excessive resist development can give rise to non-vertical resist sidewalls, which in turn are transferred to non-vertical sidewalls in the GaAs substrate. Secondly, a non-vertical flow of $Cl_2$ gas onto the substrate during the dry etch in the CAIBE can lead to asymmetric and non-vertical sidewalls. Small angle deviations ($\leq 2°$) from the vertical are hard to measure with the available resolution in
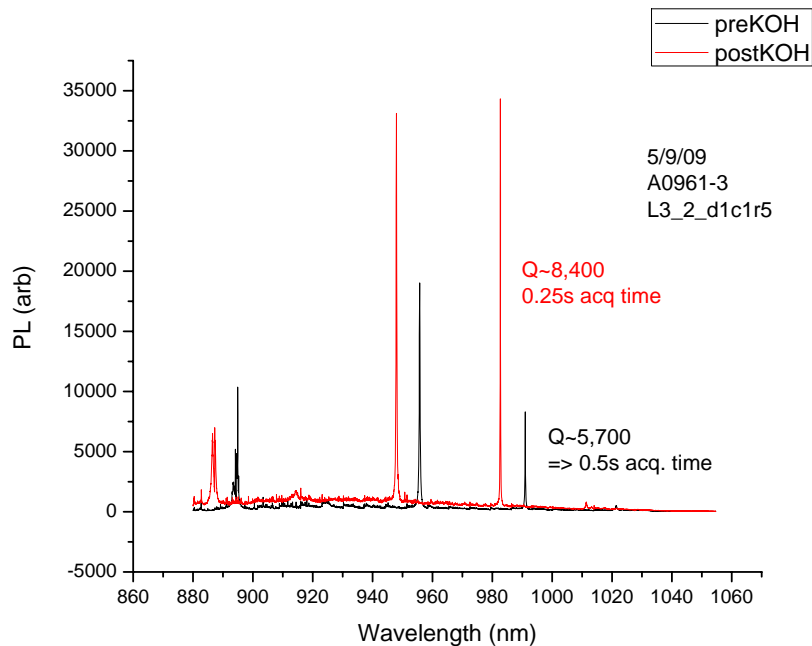
Figure 4.8: Photoluminescence spectra showing improvement in cavity-$Q$ after KOH rinse. Cavity PL before the KOH rinse (black curve) is compared with the PL after KOH rinse (red curve). (Credits: Joshua Hendrickson.)

an SEM, making it difficult to precisely quantify this loss channel.

In general, it is easier to control etch symmetry and verticality using a plasma etch, such as in an ICP-RIE. Additionally, the use of photonic crystals with a complete photonic band-gap for both TE-like and TM-like modes [47] can reduce the severity of a non-vertical etch. Significant results have been achieved using reduced symmetry photonic crystals [60, 61], although in general, the spectral extent of the TM-like band-gap is much less than that of the TE-like counterpart. Additionally, the robustness of the 1D nanobeam cavities against TE/TM coupling loss has been noted in Chapter 2.3.3.

## 4.2.4  Effect of a Bottom Substrate

Removal of the AlGaAs sacrificial layer below the photonic crystal slab creates an air gap, exposing an optically flat GaAs surface below the photonic crystal cavity. It is important for this air gap to be at least greater than half the vacuum wavelength to reduce optical loss into the substrate. Reflectivity at a GaAs surface in contact with air is $\approx 30\%$. Therefore, the effect of a bottom substrate is essentially that of a reflector below the photonic crystal mode. For an air gap size larger than half the vacuum wavelength, there can be multiple non-negligible reflections between the photonic crystal slab and substrate. Thus, a fraction of the originally downward-emitted photons

from the cavity are redirected upward by the bottom reflector to interfere with the originally upward-emitted photons. As a result, the far-field radiation pattern of the cavity mode is modified, changing the total emitted power [62, 63]. This is analogous to the well known cQED example of a point dipole source in front of a mirror [64]. By changing the distance between the dipole source and the mirror, the original decay rate and radiation patterns are modified. Correspondingly, the $Q$ of the cavity mode changes as a function of the air gap size.
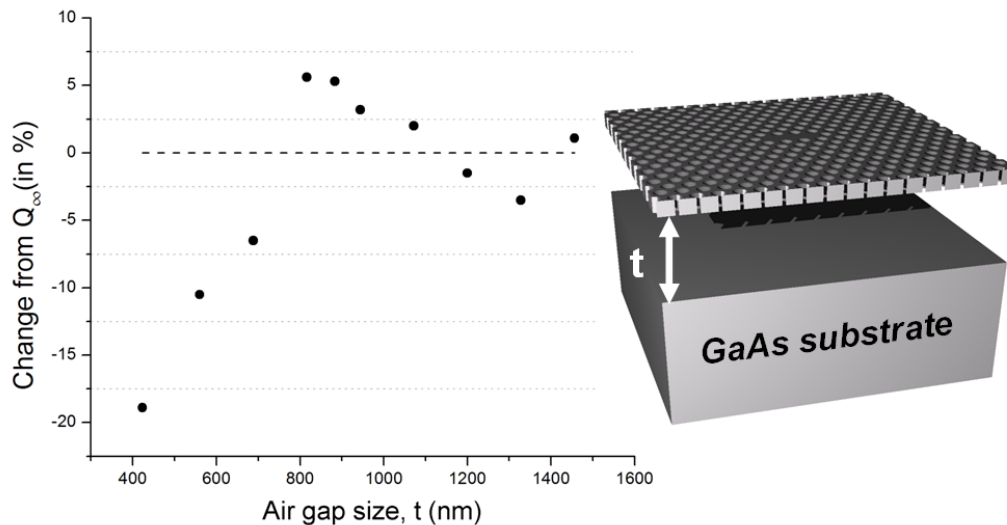


Figure 4.9: Variation of $Q$ with slab-to-substrate air gap for a slab of thickness 190 nm and a cavity mode at 1,026 nm (the other device parameters are the same as the design #2 L3 cavity shown in Table 2.3). The dashed line corresponds to $Q_\infty$ when there is no substrate in the vicinity of the slab.

In Figure 4.9, the $Q$ of the L3 cavity mode is calculated by varying the air gap size, $t$. Even when $t \geq 800$ nm, $Q$ varies by about $\pm 5\%$ around $Q_\infty$ (where $Q_\infty = 67,315$ obtained in the absence of a bottom substrate[6]). A larger variation in $Q$ can be obtained by starting with a cavity mode that has a smaller $Q_\infty$, since more radiative power will contribute to far-field interference. Through additional FDTD simulations, it is found that $Q$ variation larger than $\pm 10\%$ is expected when $Q_\infty \approx 50,000$. Therefore, the AlGaAs sacrificial layer thickness should be chosen carefully if $Q$ is of primary concern in the design of photonic crystal cavities.

## 4.2.5 GaAs-AlGaAs Interface and Crystal-axis Dependent Surface Roughness

As has been recently reported [51], the interface between the bottom of the GaAs slab and the top of the AlGaAs layer can have wavy undulations that show a root-mean-square (RMS) roughness of

---

[6]$Q_\infty$ is slightly smaller than the value reported in design #2 of Table 2.3 because computer memory constraints forced a reduction in the number of defect-surrounding photonic crystal periods, in order to incorporate the bottom substrate in the computational volume.

the order of 25 nm, while maintaining an extremely smooth top surface. By transmission electron microscopy (TEM) it was observed that the magnitude of the roughness was greater along the [110] crystal direction than the $[1\bar{1}0]$ direction. Figure 4.10 shows a TEM image of the GaAs/AlGaAs interface, clearly showing the roughness.
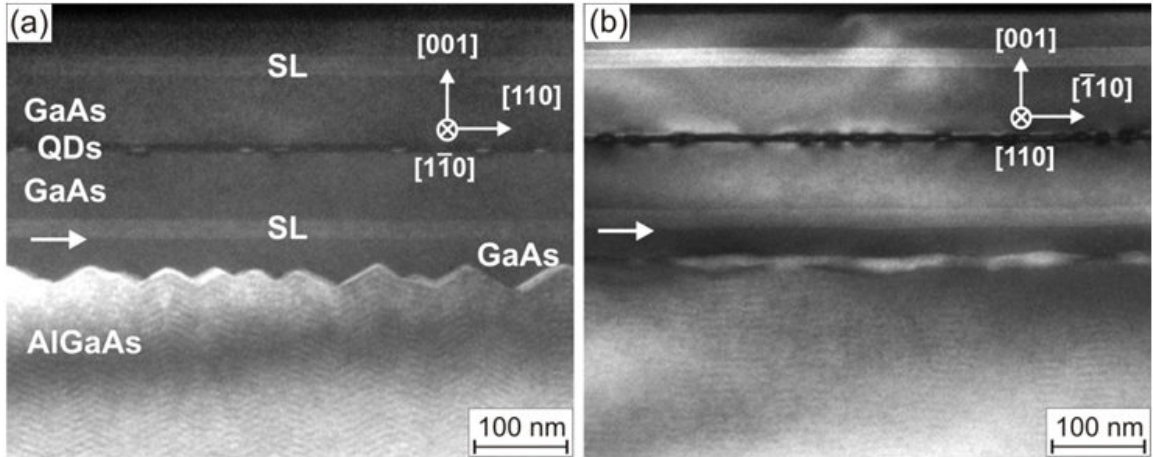


Figure 4.10: (002) dark-field cross-section TEM images of PC sample showing that AlGaAs (light) roughness is greater along (a) [110] than (b) $[1\bar{1}0]$. By the time the first superlattice (SL) is grown, GaAs (dark) growth has almost flattened the surface. (Credits: D. Litvinov & D. Gerthsen.)

Having discovered the roughness issue, the University of Arizona group systematically optimized [51] the MBE growth process by introducing a growth interruption to give time for smoothing under As, growing a thin layer of GaAs, and using a mis-oriented substrate. Most structures can be grown equally well on a flat substrate, as on one polished with surface-normal tilted a few degrees toward a particular crystal axis. However, it is known that the growth of AlGaAs is preferential along step edges lying along $[1\bar{1}0]$. If the surface is perfectly flat, then the surface diffusion may be inadequate to reach such an edge, and island formation and 3D growth can result. This explains the larger roughness along the [110] direction as seen in Figure 4.10. It was found that growth on (001) GaAs substrates mis-oriented by 2° toward the [110] direction (among a few other optimizations outlined in [51]) greatly reduced the interface roughness. See Figure 4.11 for TEM images showing substantially reduced roughness after these optimizations.

To test whether this crystal-axis dependent roughness had any bearing on cavity-$Q$s, several pairs of identical cavities were fabricated with the cavity long axis (the line joining the $s$-shifted holes in the case of the L3 designs) aligned along either of the directions mentioned above. It was found that on average, cavities whose axis was aligned along the lower roughness direction had $Q$s that were 20-32% less (see Figure 4.12[b]) than those aligned along the higher roughness direction. It must be noted that the overall $Q$s recorded in this experiment were low, on account of angled (non-vertical) sidewalls of the photonic crystal holes. Figure 4.12(a) shows the AFM scan of one such low-Q cavity.
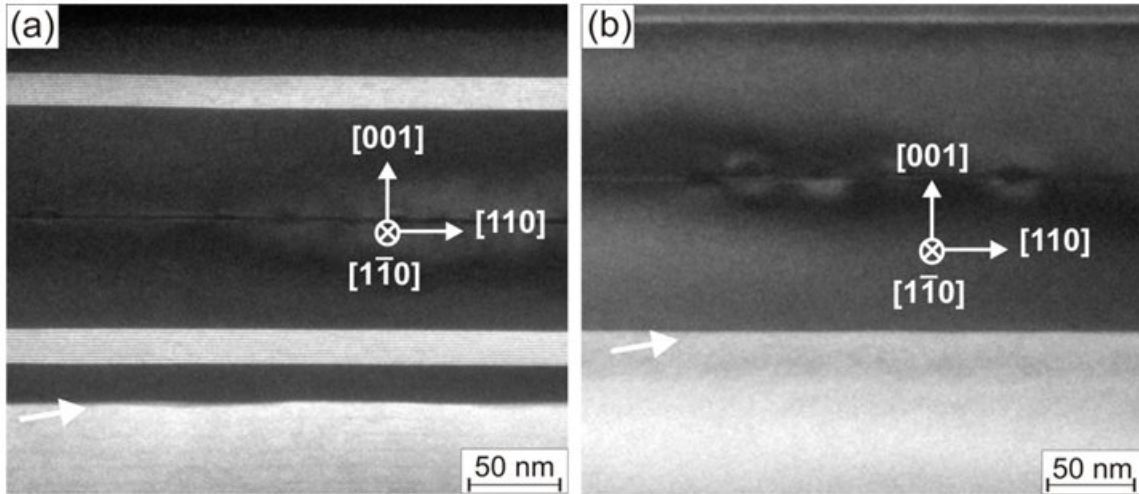
Figure 4.11: (002) dark-field cross section TEM images of (a) QD41 (grown at University of Arizona) and (b) A0961 (grown at University of Karlsruhe) showing successful growth of flatter AlGaAs sacrificial layers (marked by arrows). (Credits: D. Litvinov & D. Gerthsen.)
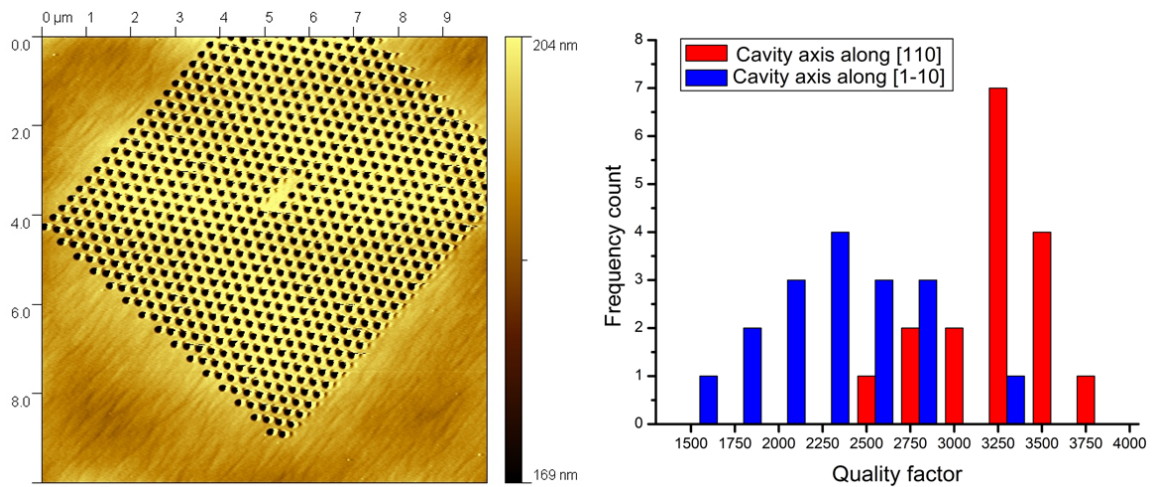


Figure 4.12: (a) AFM scan of a low $Q$ L3 cavity whose axis is aligned along the low-roughness crystal axis $[1\bar{1}0]$ (running from bottom left to top right in the image). (Credit: Benjamin Richards.) (b) Histogram for $Q$ values corresponding to the two different orientations of cavity and crystal axis.

Finally, roughness and ion-induced sidewall damage are introduced to the surfaces during the CAIBE etch, which can further contribute to scattering. It is not possible to quantify the contribution of the latter source of scattering at this point, as the surfaces seem fairly smooth, even in high resolution SEM images.

In conclusion, several factors contributing to photon loss from photonic crystal cavities designed for cQED experiments have been identified and addressed. Among them are irregularities with fabrication, crystal-axis dependent losses, and the presence of a bottom substrate. Lithography issues can be corrected by ensuring a properly focused electron beam; etched sidewalls can be made

vertical by careful control of the Cl$_2$ flow direction during dry etch; crystal-axis-dependent losses can be eliminated by optimized growth that leads to smooth slab-interfaces; remnant resist can be removed by an oxygen plasma, and debris left behind by the HF undercut can be removed by treating with KOH. Careful choice of sacrificial (AlGaAs) layer thickness can enhance cavity-$Q$. Finally, the use of contour FDTD as a diagnostic tool for estimating cavity-$Q$s has been highlighted.

# Chapter 5

# Properties of Trapped Light

In this chapter, quantitative measurements of the quantum nature of light emission from QDs coupled to cavities are presented. The first half examines cavity-induced enhancement of QD light emission by comparing two QDs in the spectral and spatial neighborhood of the cavity: one that couples to the cavity, and the other that doesn't. In the second half, a Hanbury Brown-Twiss interferometer is used to measure photon correlations, using which, the properties of light emission are quantified.

## 5.1 Quantum Dot Enhancement

To see any of the interesting cQED effects discussed in Chapter 1, it is important to maximize the coupling between QD and cavity and, to this end, increasing the spectral and spatial alignment between QD and cavity is imperative. Several experimental methods are available for increasing this alignment.

To increase the spatial alignment between the cavity field anti-node and the QD, broadly two techniques are available. One is to allow random growth of low-density QDs, locate an individual QD, and fabricate a cavity around this QD. In one such experiment [16, 65], several QD layers were stacked on each other up to the top surface of the photonic crystal slab. The QDs in each layer grew preferentially above QDs in the layer below, and by AFM techniques, the top QD was located, and a cavity was fabricated around it. In the second technique QD growth is spatially deterministic, making it easier to align with cavities. In this technique [66], after the bottom half of the device slab has been grown, the wafer is patterned with a periodic array of shallow ($< 10$ nm) pits, which strain-induces the growth of QDs above them when the wafer is put back in to the growth chamber for subsequent QD and top-half-slab growth.

To increase the QD-cavity spectral alignment, many more experimental "tuning" knobs are available. The most routinely used techniques are enumerated below:

1. Temperature - The QD transition frequency can be varied by changing the temperature of the He cryostat [12, 13], or by local laser heating [67].

2. Condensation - By condensing xenon or nitrogen gas on to the photonic crystal surfaces [68], there is a reduction in effective hole radius and an increase in slab thickness. As a result, cavity frequency can be tuned. When the cavity is heated up (by increasing the cryostat temperature), the condensate leaves the surface, thus allowing reversible tuning of the cavity.

3. Wet etching - In this process, the cavity is precisely but irreversibly etched [65] away in small amounts, allowing a one-time tuning of the cavity resonance. Typically, a hydrogen peroxide based solution is used to oxidize the photonic crystal surfaces, and an etchant such as citric acid is used to remove the oxidized surfaces. This increases the hole radius, and decreases the slab thickness, thus changing the cavity frequency.

4. Stark shifting - By applying an AC [69] or DC [70] electric field across a QD, its transition frequency can be altered.

In our experiments [68], (cryostat) temperature tuning between 4-40 K allows a QD wavelength tuning of $\approx 2$ nm, while Xe condensation allows a 4 nm tuning of the cavity wavelength when the cryostat is held at 20 K. So far, a spatially-probabilistic growth mode of the QDs has been relied upon, while work on wafer pre-patterning for spatially deterministic QD growth is in-progress.
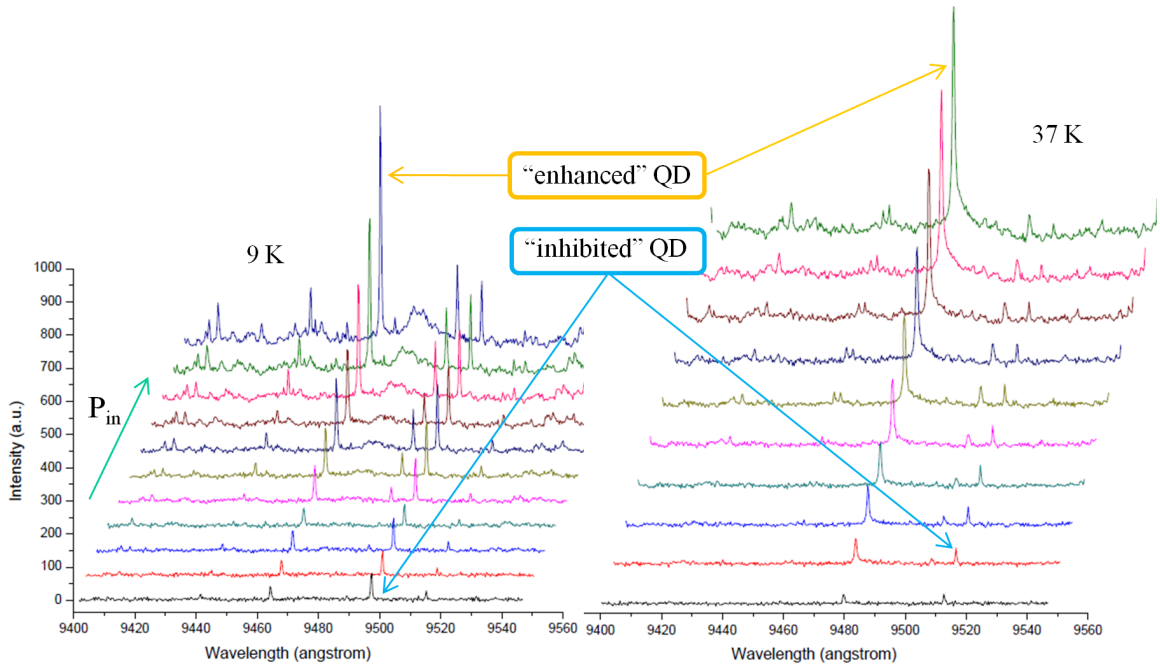


Figure 5.1: Cascaded PL spectra showing QD enhancement/inhibition as a function of incident power (from bottom to top in $\mu$W: $0.35, 0.78, 1.02, 1.34, 1.83, 2.34, 3.2, 4.22, 5.4, 6.85$). Left pane shows spectra at 9 K with enhanced QD detuned from cavity, while right pane shows spectra at 37 K at zero detuning. The $x$-axis is offset to the right by 20% for clarity in each successive cascade. (Credit: Joshua Hendrickson.)

As was graphically depicted in Figure 1.2, when the cavity and QD decay rates exceed the

coupling strength (weak-coupling regime), Purcell enhancement/inhibition of the QD transition is expected. Here, an experimental demonstration of this effect is presented. In a low-$Q$ cavity ($Q \approx$ 4,000, low enough to not be strongly coupled) the emission from a single QD was found to be greatly enhanced by cavity coupling, while a nearby detuned QD showed no such enhancement [71]. Given that the spot-size of the exciting laser extends a few photonic crystal layers beyond the spacer region, the QD experiencing inhibition could either be inside the spacer region (potentially close to a field node), or outside the spacer but within the photonic crystal (where it experiences the photonic band-gap). On the other hand, the response of the enhanced QD to the input excitation power is indicative of a coupling between QD and cavity.
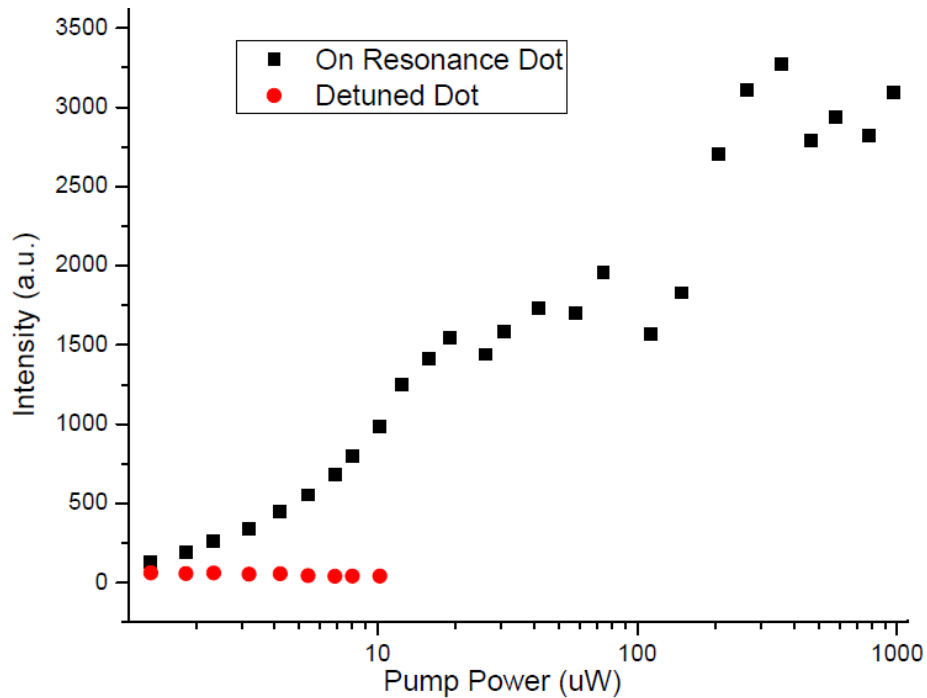


Figure 5.2: Comparison of enhanced and inhibited QD luminosity (output power) as a function of input power at 37 K.

Figure 5.1 shows cascaded PL spectra of this effect. In the left pane, the temperature is kept constant at 9 K, and the two QD peaks of interest are seen at $\lambda_1 = 946.2$ nm and $\lambda_2 = 949.7$ nm, and the cavity peak is somewhere in between. The QD peak at $\lambda_1$ is found to increase in luminosity with increasing input power, while the peak at $\lambda_2$ remains constant at first, and then increases slightly. The QD peaks are then tuned by increasing the temperature to 37 K, moving the QD peaks to longer wavelengths—the first peak from $\lambda_1$ to $\lambda_1' = 948.0$ nm, and into resonance with the cavity (which does not correspondingly change its resonant wavelength), and the second peak from $\lambda_2$ to $\lambda_2' = 951.7$ nm. In this case, the enhancement of the QD luminosity is even more apparent, as indicated in the right pane of Figure 5.1, and seen quantitatively in the plot of output power

versus input power (plotted on a log scale) in Figure 5.2. The output power of the inhibited QD saturates at an input power of approximately $10\,\mu$W, where as the output power of the enhanced QD continues to grow and begins to saturate at an excitation level roughly 100 times higher.

Before concluding this section, the role that QDs play in enhancing cavity-$Q$s by providing gain is discussed. In a sample different from the one discussed above, a cavity with a low $Q$ of $\approx 4,000$ under low-power excitation $(2.4\,\mu$W) began to show a narrowing of the cavity-mode linewidth with increasing excitation power, reaching a $Q$ of $\approx 11,000$ at $500\,\mu$W. The intermediate values are shown in Figure 5.3. The QD ensemble PL for this particular wafer can be seen in the bottom pane of Figure 4.1, and the cavity wavelength of 982.1 nm is clearly at a lower energy (longer wavelength) as compared to the center of the QD ensemble, resulting in gain-narrowing of the cavity linewidth. At a relatively high excitation power of $500\,\mu$W, QD absorption saturates, as does the cavity-$Q$.
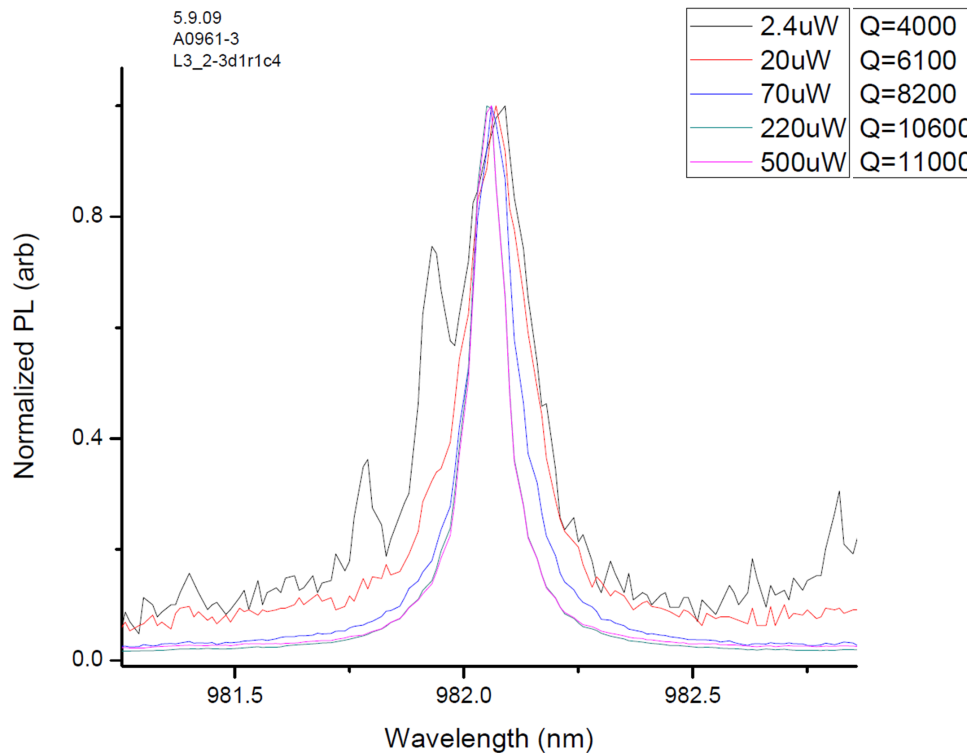


Figure 5.3: Gain-induced enhancement of cavity-$Q$.

## 5.2 Photon Statistics and Correlations

It has been a long-standing concern in the field of quantum optics to measure the statistics of light emission from different sources, and to classify these statistics into useful categories. One such useful classification is in the quantification of the Poissonian nature of the statistics. The probability mass

function[1] of a Poissonian distribution is given by $P(n) = e^{-\overline{n}}\,\overline{n}^n/n!$, where $n$, $\overline{n}$ represent the photon number and statistical mean, respectively. It is a well known property of the Poissonian distribution that the standard deviation (square-root of the variance), $\Delta n$ is equal to the square-root of the mean, $\Delta n = \sqrt{\overline{n}}$. The three useful categories of photon statistics are then [5]

- Super-Poissonian: $\Delta n > \sqrt{\overline{n}}$. eg.,thermal, partially coherent, incoherent light.

- Poissonian: $\Delta n = \sqrt{\overline{n}}$. eg.,perfectly coherent light.

- Sub-Poissonian: $\Delta n < \sqrt{\overline{n}}$. eg.,non-classical light.

As it turns out, the statistical nature of the photon detection process and the intrinsic photon statistics of the light beam get "mixed" up in the measurement process. In a semi-classical model, the light field is treated classically, while the photoelectric effect in the detector is quantized. In such a treatment it is found [5] that Poissonian "photon" statistics can be observed even with a classical light wave that has time-independent intensity, and that the Poissonian statistics can be attributed to the probabilistic nature of photo-electron emission from the detector. Allowing for a time-dependent intensity in the light wave increases the variance, leading to super-Poissonian statistics. Thus, the experimental observation [72] of sub-Poissonian statistics indicated that the classical description of light is inadequate. It must be noted that the observation of sub-Poissonian statistics depends on the availability of detectors with very high quantum efficiency, and in the first experimental report [72] only a 0.16% reduction in variance from the Poissonian value was found.
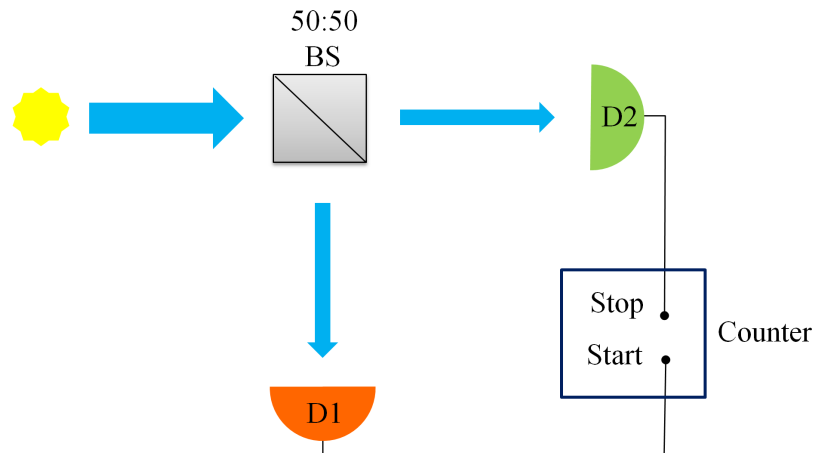


Figure 5.4: Schematic of a Hanbury Brown–Twiss interferometer. BS represents the beam splitter, D1 & D2 are photo detectors.

Instead of computing photon statistics, the (equivalent) use of a second-order correlation function $g^{(2)}(\tau)$ to quantify light is found to produce larger non-classical effects. In this picture, light can be classified as being bunched, coherent, or anti-bunched. A Hanbury Brown–Twiss (HBT)

---

[1]The probability that a discrete random variable is exactly equal to a particular value.

interferometer[2] allows the calculation of this correlation function, and was used to make a quantitative statement about the nature of light emission from the enhanced QD discussed in the previous section. The HBT is shown schematically in Figure 5.4. In it, incident light is partitioned using a 50:50 beam-splitter (BS) and a detector is placed in each path (D1 & D2). The detection of a photon on one of the detectors, say D1, starts a timer, while the detection of a photon on D2 at or after this event stops the timer. This entire process is considered a "count," and a histogram of the number of counts as a function of the time delay $\tau$ between events is built up. Such a histogram is quantified by means of the second-order correlation function $g^{(2)}(\tau)$, which is classically expressed in terms of light intensity $I(t)$. In the quantum picture the intensity is proportional to the photon number[3], $n(t)$, and this leads [5] to

$$g^{(2)}(\tau) \equiv \frac{\langle I(t)\,I(t+\tau)\rangle}{\langle I(t)\rangle\langle I(t+\tau)\rangle} = \frac{\langle n_1(t)\,n_2(t+\tau)\rangle}{\langle n_1(t)\rangle\langle n_2(t+\tau)\rangle} \tag{5.1}$$

where $n_i$ represents the photon count on the $i^{\text{th}}$ detector. Thus, $g^{(2)}(\tau)$ is dependent on the simultaneous probability of a joint detection at D1 and after a time delay $\tau$ at D2, and by examining the HBT schematic in Figure 5.4, it is clear that the interferometer calculates $g^{(2)}(\tau)$.

The case of a zero time-delay merits a special mention; it corresponds to the case of simultaneous photon detection at D1 and D2. Based on this value of $g^{(2)}(0)$, light is classified as

- bunched, $g^{(2)}(0) > 1$,

- coherent, $g^{(2)}(0) = 1$,

- anti-bunched, $g^{(2)}(0) < 1$.

It is found [5] that for any classically described light $g^{(2)}(0) \geq 1$ & $g^{(2)}(0) \geq g^{(2)}(\tau)$, and that anti-bunched light is a purely quantum effect with no classical analogue. The HBT interferometer was used to measure $g^{(2)}(\tau)$ for light emission from the enhanced QD [71], and the un-normalized version of the correlation function $(G^2(\tau))$ is plotted in Figure 5.5. Due to a difference in cabling length between the two detectors, $\tau = 0$ is shifted to $\tau = 34$ ns in the figure, and a clear drop in the coincidence-counts for $\tau = 34$ ns is seen at this value, proving that light emission is anti-bunched. As a consequence of the anti-bunched nature, it can be said that the light emission comes from a *single* QD; once a single QD (cavity-enhanced in this case) is excited, it can emit only a single photon, leading to a very low number of simultaneous detection events. This number is not zero due to finite response-time of the detectors.

A natural extension of anti-bunched QD light-emission is its use as a single-photon source. To demonstrate the working of such a source, the coupled QD-cavity system was excited by means of a

---

[2]Originally used by astronomers Hanbury Brown and Twiss to measure the diameters of stars from the nearby Mt. Wilson observatory in the 1920s.

[3]More precisely, the photon number operator is defined in terms of the photon creation and annihilation operators ($a^\dagger$ and $a$, respectively) as $n \equiv a^\dagger\,a$.
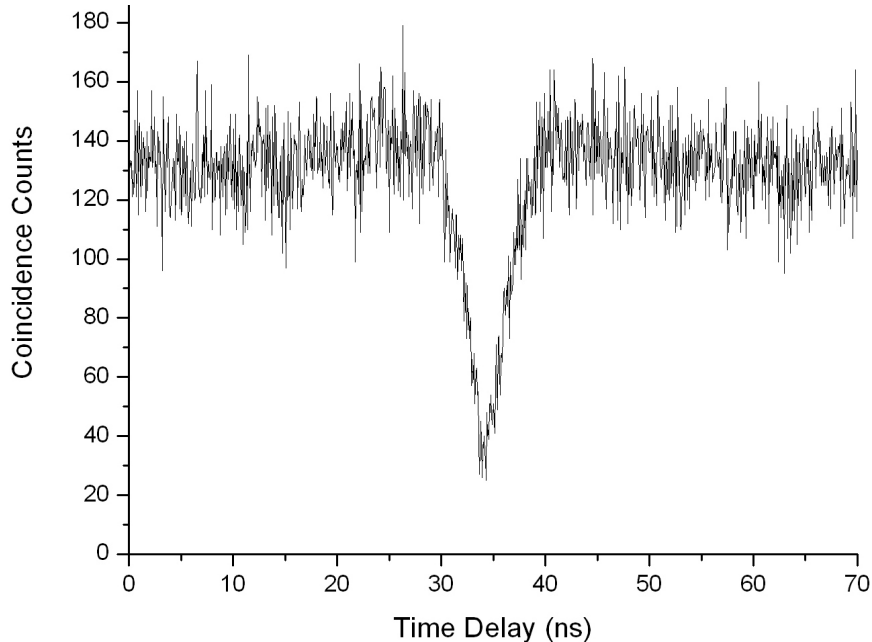
Figure 5.5: $G^2(\tau)$ for light emission from a cavity-enhanced QD. The point on the time axis corresponding to simultaneous detections at D1 and D2 in the HBT (see Figure 5.4) is shifted from $\tau = 0$ to $\tau = 34$ ns due to a difference in cabling length between D1 and D2. The dip seen around $\tau = 34$ ns shows the anti-bunched nature of the light emission. Detectors are Perkin Elmer single-photon modules with less than 100 dark counts/second.

pulsed laser, and the light-emission correlations were measured using the same HBT interferometer. The pulse repetition period was chosen to be greater than radiative lifetime of the QD. As before, the detection of a photon at D1 starts the timer, and the detection of a second photon at D2 increments a counter by one. In this way a histogram of counts is built up as a function of time-delay from the first photon detection. Results are shown in Figure 5.6 where again, due to a cabling-length difference between the two detectors, $\tau = 0$ is shifted to $\tau = 34$ ns. The pulse repetition period is 12.5 ns, and each pulse results in the emission of a single photon from the QD. Again, the number of counts seen at $\tau = 34$ ns is significantly less than the number of counts seen at any integer displacement of 12.5 ns from $\tau = 34$, confirming the single-photon nature of QD light-emission. The deviation from the ideal zero-value at $\tau = 34$ ns can be attributed to the background light generated by the wetting layer or contributions from transitions of other QDs in the vicinity [73].

In conclusion, it must be noted that the stringent conditions for the system to be strongly coupled need not be met in order to see the above effect. In fact, the light emission from a QD is anti-bunched without the need of a cavity [74]. The cavity-induced enhancement of QD luminosity, for which weak coupling is good enough, helps to greatly improve the signal SNR. The use of semiconductor-based QDs embedded inside micro-cavities for implementing single-photon sources has very promising applications to communication and quantum cryptography systems.
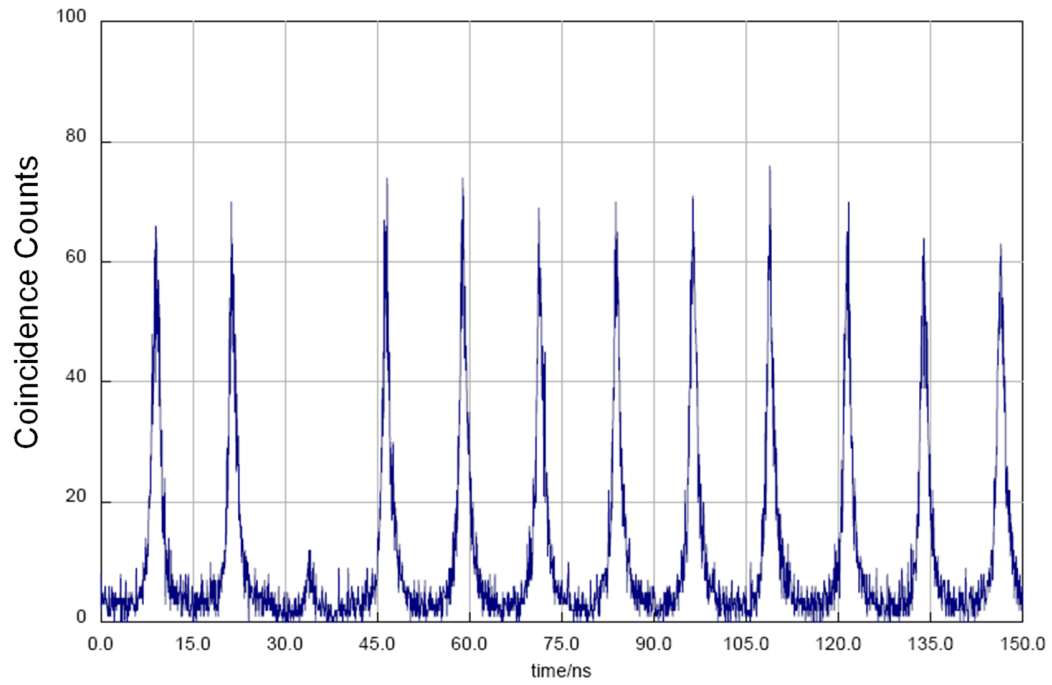
Figure 5.6: Histogram of photon counts as a function of time for pulsed excitation. The point on the time axis corresponding to simultaneous detections at D1 and D2 in the HBT (see Figure 5.4) is shifted from $\tau = 0$ to $\tau = 34$ ns due to a difference in cabling length between D1 and D2. The peaks are separated by the pulse repetition period of 12.5 ns.

# Chapter 6

# Applications

This thesis has explored the motivations behind trapping light, described the theory and construction of devices that trap light and, having investigated the technical issues that affect the efficiency of light confinement, has touched upon the quantum nature of light emission from these devices. The applications of such devices are various and range from the use of single-photon sources in quantum-cryptography and communication systems, to the use of entangled light-matter states[1] in quantum computation schemes, to the use of high-$Q$ cavities in sensing minute changes in the cavity environment, and finally to the use of cavities with active media for creating ultra-small, low-power lasers.

To conclude the thesis, first, a promising application of the 1D nanobeam cavities is presented. This is a proposal [75] of an electrically-pumped laser, the key idea of which is the close proximity of metal to the laser cavity to reduce device resistance, while maintaining a high $Q$. Finally, material system optimizations are proposed in two forms: The first deals with engineering QD growth in III-V-based systems to have light emission at telecommunications (telecom) wavelength range ($\lambda \approx 1.55 \, \mu$m), and the second deals with the incorporation of III-V-based active media in Si cavities. Work on these applications is in progress, and preliminary results are discussed.

## 6.1 Electrically-Pumped Laser

Electrically-pumped lasers have long been sought to demonstrate "practical" applications of photonic crystal devices. The potential of creating an integrated, low mode-volume (less than $(\lambda/n)^3$), low power, electrically-pumped laser has driven the research in this direction, in spite of the complicated fabrication and intricate wafer growth that is involved [76, 77].

Fabrication is complicated because of the multiple lithography steps required to define the cavity region as well as the electrical contacts, along with the necessary alignment between these steps. Additional steps include metal deposition for the contacts and wire bonding to them. There can be

---

[1]As seen in strongly coupled systems.

further fabrication challenges, depending on the device geometry. For instance, one of the successful electrically-pumped lasers [77] required very precise wet-etching control to create a narrow post below the photonic crystal slab that served as a current route and bottom contact. Some other designs [78] involve careful wafer bonding between delicate semiconductor layers and metal films. Wafer compositions tend to be more involved than the types that have been discussed in preceding chapters, since doping has to be incorporated into the device semiconductor layers for a reduction in contact resistance *and* the generation of electron-hole pairs (EHPs). Thus, it is common to have a $\{p^+ - p - i - n - n^+\}$ type doping profile in the current path, where $p$, $n$ refer to $p$-type and $n$-type doping, respectively, the superscript "+" refers to heavier doping for the contact regions, and $i$ refers to the intrinsic region where EHP recombination and light generation occurs. The previously mentioned designs have such a doping profile in the vertical direction, i.e., perpendicular to the photonic crystal lattice.

An additional difficulty is the sensitivity of the cavity $Q$ to the proximity of electrical conductors, such as metals or highly doped semiconductors that lower $Q$ by absorption. Yet, placing the electrodes far from each other in an attempt to preserve the cavity $Q$ results in a large device resistance and high lasing-threshold [79].

The inclusion of metal in FDTD simulations presents an added level of complexity. A metal such as gold has a complex permittivity. In particular, the real part of gold's permittivity is negative [80] in the infra-red wavelength range considered here (0.90-1.35 $\mu$m). Note that in a homogeneous medium with complex permittivity, $\epsilon = \rho\, e^{j\theta}$ ($\rho > 0$), the dispersion relation is simply given by

$$\omega = \pm ck/\sqrt{\epsilon} = \pm(ck/\sqrt{\rho})\, e^{-j\theta/2} = (ck/\sqrt{\rho})\,(\pm\cos(\theta/2) \mp j\sin(\theta/2)) \tag{6.1}$$

Thus, when $\theta \neq 2m\pi$, $m \in \mathbb{Z}$, the frequency contains imaginary components, one of which corresponds to (unphysical) exponentially growing fields, which in turn leads to numerical instability. In a physical medium the permittivity isn't static, and from the Kramers-Kronig relations [81] it follows that any medium with complex $\epsilon$ must be dispersive, i.e., $\epsilon \mapsto \epsilon(\omega)$. By defining a dispersive medium (with appropriate parameters empirically determined), the effect of a complex permittivity can be incorporated in a FDTD simulation.

To investigate which cavity design suffers the least from the introduction of metal, 3D FDTD simulations for L3 and 1D nanobeam cavities (discussed in chapter 2.3) were performed using a 200 nm GaAs slab that has either air or aluminum oxide below it. A 100-nm thick gold film is deposited on top of the GaAs surface before cavity formation. The film is subsequently perforated with air holes in the process of cavity formation. Additionally, the film is discontinuous around the cavity region. In order to simulate realistic gold, its experimentally determined [80, 82] permittivity at $1.060\,\mu$m is used in the FDTD calculations. Figure 6.1 schematically shows the metal-cavity alignment for the
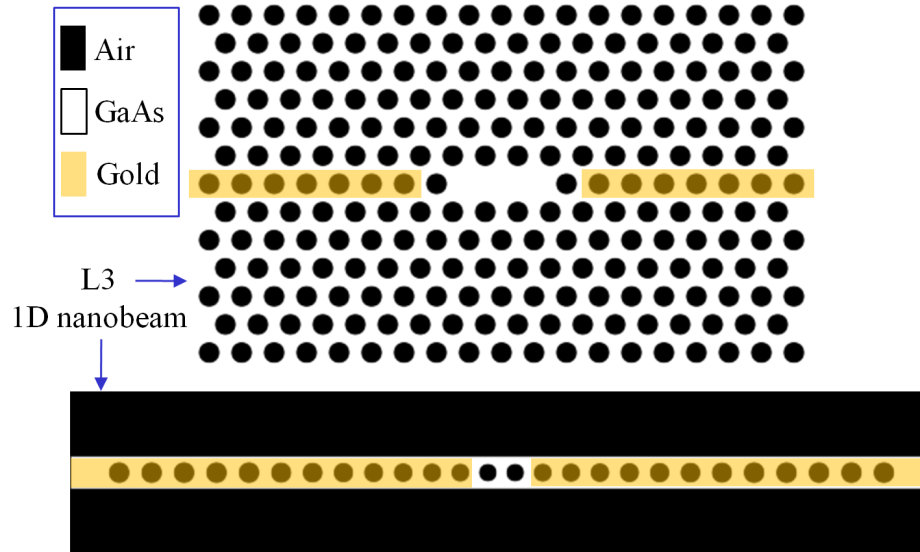
Figure 6.1: Metal-cavity configurations considered for creating an electrically-pumped laser.

two types of cavities. Table 6.1 shows a comparison of $Q$s for different cavity implementations. It can be seen that the 1D nanobeam cavity offers a much higher $Q$ in any configuration, and is robust to changes in surrounding materials; adding an aluminum oxide substrate and top gold electrodes still results in a $Q$ of 58,000.

| Cavity | Substrate | Metal width (nm) | Metal-pad gap (nm) | Lattice constant (nm) | $Q$ | $\lambda$ (nm) |
|---|---|---|---|---|---|---|
| L3 | Air | 261 | 1,506 | 261 | 9,298 | 1,064 |
| L3 | Aluminum oxide | 258 | 1,489 | 258 | 693 | 1,064 |
| 1D-nanobeam | Air | 279 | 150 | 279 | 484,643 | 1,062 |
| 1D-nanobeam | Aluminum oxide | 276 | 150 | 276 | 58,233 | 1,070 |

Table 6.1: Table of cavity-parameters for different cavity-metal configurations. Gold and GaAs thicknesses are fixed at 100 nm and 200 nm, respectively.

Having selected the 1D nanobeam cavity, device fabrication is now described. In contrast to the other device geometries that feature a vertical doping profile by the use of differently doped device layers during crystal growth, here, a lateral doping profile $\{p - i - n\}$ is created by multiple lithography steps and ion implantation. For the sake of concreteness, it is proposed that the device be fabricated in a GaAs wafer that has gain media (either QDs or quantum wells (QWs)) embedded in the middle of the GaAs slab. Six basic fabrication steps are outlined in Figure 6.2 and are now elaborated (each pane of the figure shows a device top view at the *end* of the numbered step):

1. The wafer surface is cleaned to remove any organic contamination and native oxide. A positive-
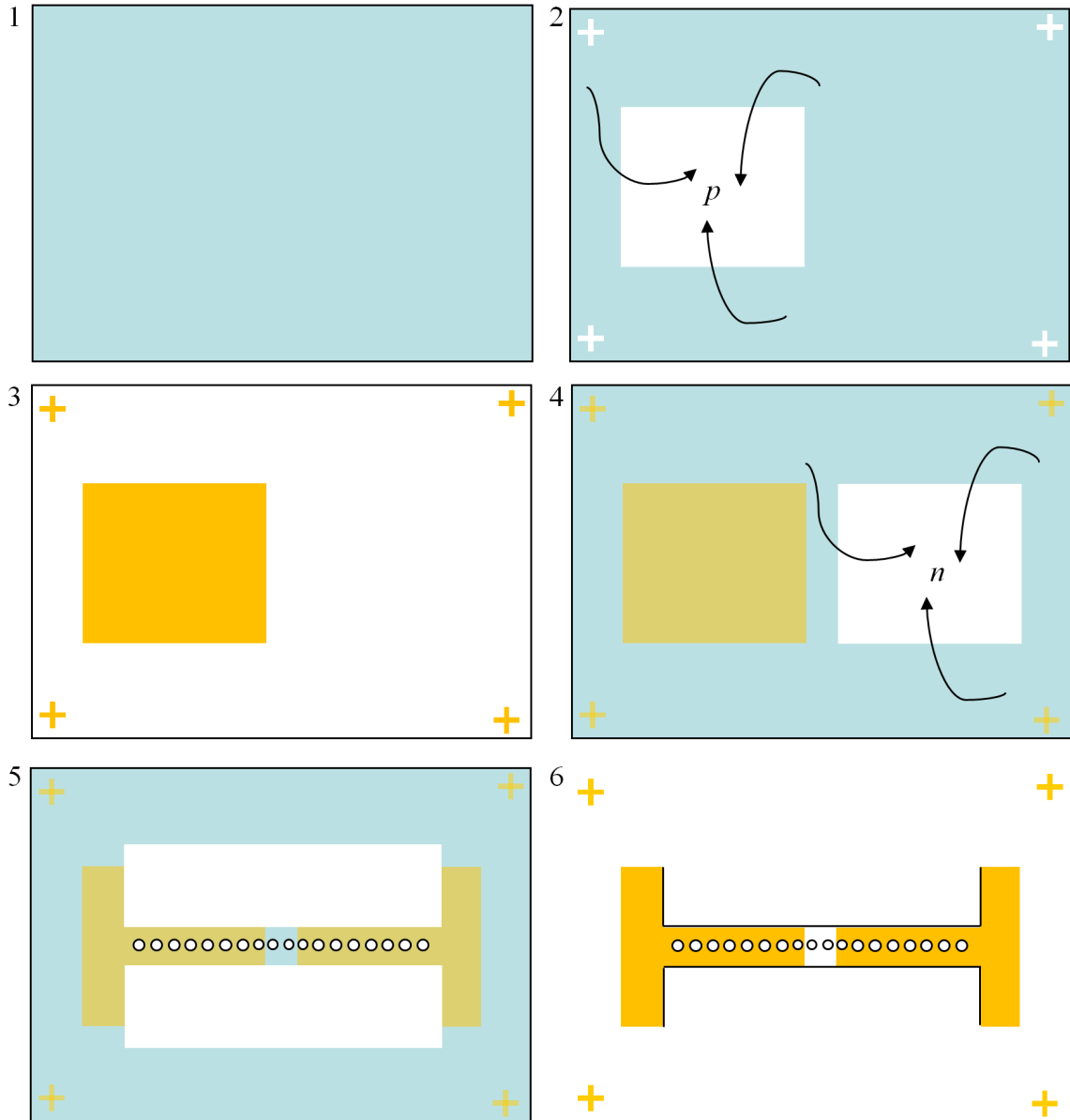
Figure 6.2: Main steps in the fabrication of an electrically-pumped laser using a 1D nanobeam cavity, lateral doping profile and gold contacts (not drawn to scale). Blue corresponds to resist, orange corresponds to gold. See text for further details.

tone electron-beam (e-beam) resist is spun-on.

2. During e-beam lithography, four alignment marks are defined, along with the exposure of a $20\,\mu\text{m} \times 20\,\mu\text{m}$ square in the left half of the outer rectangle. The exposed resist is developed, and $p$-type doping is incorporated in the exposed areas by means of ion implantation, with $p^+$-doping on the top surface to reduce contact resistance.

3. A $0.100 - \mu\text{m}$ layer of gold is evaporated on the wafer surface, followed by a lift-off process,

which removes the resist and leaves behind a gold square and four alignment marks.

4. A new layer of e-beam resist is spun on. Using the alignment marks, a second $20\,\mu$m $\times\,20\,\mu$m square is exposed to the right of the first square, leaving a 0.150-$\mu$m gap between the squares. After resist development, $n$-type doping is incorporated in the exposed areas by means of ion-implantation with, as in step 2, $n^+$-doping on the top surface.

5. Step 3 is repeated, leaving behind two gold squares, which will act as contact pads, between the four alignment marks. A third layer of e-beam resist is spun on, and using the alignment marks, a 1D nanobeam cavity is exposed and developed. The cavity region is placed in the middle of the 0.150-$\mu$m gap between the two gold squares, such that the cavity region does not have gold just above it.

6. Finally, with the resist acting as an etch mask, the wafer is dry etched to leave behind a 1D nanobeam cavity with a perforated gold film on top. Depending on the application, the layer beneath the GaAs slab may be wet etched or oxidized to $Al_xO_y$.

The choice of the 1D nanobeam cavity offers two advantages. First, the aluminum oxide substrate acts as a heat sink for the laser cavity, making it possible to consider CW-operation. Earlier demonstrations of electrically-pumped lasers [77] have suffered from heating dissipation issues, making only pulsed operation possible. Secondly, the device offers low electrical resistance. This is composed of resistance at the gold-GaAs interface and in the $p-i-n$ structure itself, the latter contribution being dominant. The current design allows the two electrodes to be brought to a distance of 150 nm from each other. This largely reduces the distance the charge carriers have to travel in order to radiatively recombine in the cavity, and comparing with similar geometries [83], translates into a sub-k$\Omega$ resistance, enabling low threshold lasing.

## 6.2   Material System Optimization

There is a widespread consensus in the semiconductor industry about the superiority of silicon processing over that of III-V materials such as GaAs, InP, and related alloys. This is seen by way of smoother and near-perfect verticality of etch sidewalls in the case of Si structures. Further, the ease and long-term stability of surface passivation of the Si surface results in surface recombination velocities being orders of magnitude less than the corresponding numbers for GaAs or InP [84]. As a consequence, surface-state-induced losses are lower in Si structures. Surface states absorb light with energies closer to the band-gap more efficiently [53], and so a given resonator will have a lower $Q$ at wavelengths closer to the band-gap.

For these reasons, photonic crystal cavities in Si have shown higher [56, 55] $Q$s at telecom wavelengths ($\approx$ 1.50–1.60 $mu$m) than corresponding cavities in GaAs or InP at lower wavelengths

($\approx$ 0.950–1.35 $mu$m). At the same time, recent experiments have reported [85] high $Q$s ($\approx$ 700,000) in GaAs cavities at longer (telecom) wavelengths, comparable with Si cavities at the same wavelength. A fundamental difference between Si and III-V materials is the capability of incorporating optically active material during wafer growth. While Si is an excellent medium for guiding and trapping light, it is very unsuitable for light generation owing to its indirect band-gap nature. On the other hand, the growth and optical properties of active media (such as QDs in the wavelength range $\approx$ 0.950–1.35 $mu$m) in III-V materials are well characterized. As discussed earlier in the thesis, this attribute of III-V materials has led to novel optical devices such as single-photon sources and lasers, as well as allowing the investigation of fundamental cQED effects. Constrained by active media, these devices have so far been limited to wavelengths less than $1.35\,\mu$m.

It is clear from experimental data that to create such type of active devices with higher $Q$s will require a paradigm shift in device growth and fabrication. To this effect, two parallel directions are being pursued in our experiments, and at the time of writing (April 2010) these experiments are in preliminary phases. The first approach attempts to create gain media in III-V material systems that are optically active at $1.55\,\mu$m. In the second approach, III-V-based gain media are grown on specially prepared Si substrates. Both approaches leverage the fact that photonic crystal cavity designs are scale invariant, and that Si and GaAs have similar permittivity at these wavelengths ($\approx$ 12.5). Thus, the same cavity design can be applied to both material systems at various wavelengths by simple rescaling.

## 6.2.1  InAs Quantum Dots at $\lambda \approx 1.55\,\mu$m

Several attempts have been made over the years to tailor [86, 49, 87] the emission of III-V QDs (InAs or InGaAs) to longer wavelengths. The QD emission wavelength is highly size dependent, and thus by increasing the size of the QD, its emission can be shifted to a longer wavelength. As discussed in chapter 3.1, QD growth is strain induced, and the strain comes from a lattice mismatch. In the case of InAs/GaAs structures, this mismatch [49] is $\approx$ 7%. At least two different techniques have been used to reduce this mismatch, and hence decrease the strain (which in turn increases the QD size). One has been the use of InAs/InP structures [49], which have a mismatch of $\approx$ 3%, while another technique [86] relies on covering the QD layer in a strain relaxing $Ga_xIn_{1-x}As$ layer.

Our approach is based on the latter technique. InAs QDs form on a GaAs layer, and these layers are sandwiched between strain relaxing $Ga_{0.47}In_{0.53}As$ layers. Further, this entire structure is sandwiched between higher band-gap [88] $Ga_{0.32}Al_{0.15}In_{0.53}As$ layers. This QW implementation leads to further carrier confinement. This composite structure is grown on an $Al_{0.48}In_{0.52}As$ layer that is lattice matched to an InP substrate. The detailed structure is presented in table 6.2. Figure 6.3(a) shows PL from the QD ensemble at 10 K for different excitation powers.

Device fabrication in these stacks is more complicated than GaAs fabrication, mainly on account

| Thickness (nm) | Composition | Function |
|---|---|---|
| 4 | $Ga_{0.47}In_{0.53}As$ | Cap layer |
| 135 | $Ga_{0.32}Al_{0.15}In_{0.53}As$ | Slab top half |
| 2 | $Ga_{0.47}In_{0.53}As$ | Strain relaxing/QW layer |
| 3.5 ML* | InAs | QD layer |
| 2 ML* | GaAs | Strain inducing layer |
| 2 | $Ga_{0.47}In_{0.53}As$ | QW layer |
| 135 | $Ga_{0.32}Al_{0.15}In_{0.53}As$ | Slab bottom half |
| 4 | $Ga_{0.47}In_{0.53}As$ | Under cap layer |
| 1500 | $Al_{0.48}In_{0.52}As$ | Sacrificial layer |
| 100 | $Ga_{0.32}Al_{0.15}In_{0.53}As$ | Wet-etch stop layer |
| 100 | $Al_{0.48}In_{0.52}As$ | Lattice matched to substrate |
| - | InP | Substrate |

Table 6.2: Device stack of wafer HSG22 for long wavelengths ($ML^*$: monolayers). MBE growth performed by Hyatt Gibbs and Galina Khitrova.
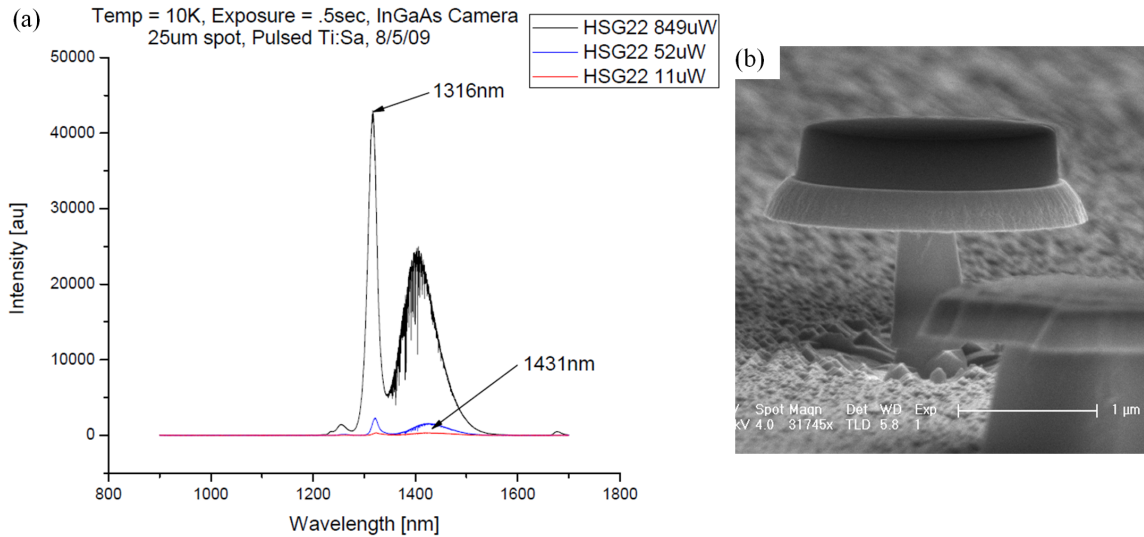


Figure 6.3: (a) QD ensemble PL from a bulk wafer (HSG22) at 10 K for different excitation powers. Ensemble is centered around 1431 nm at $52\,\mu$W. (Credit: Hyatt Gibbs, Galina Khitrova.) (b) Initial fabrication attempts of micro-disks. The darker disk seen on top of the slab is the etch mask. The slab has been undercut using a HCl wet etch.

of the presence of indium in the wafer. If a $Cl_2$ etch chemistry is used (like in the case of GaAs etching), it is important to heat the substrate since the etch by-products (chlorides of In) sublimate at temperatures higher than room temperature. Alternatively, a hydrogen iodide (HI) etch chemistry can be used since the corresponding iodides of In have lower sublimation temperatures. Since the slab layers contain Ga, Al, In, and As, it is crucial to control the relative rates of etch by-product formation for *all* these elements in order to get smooth and vertical side walls. Preliminary fabrication attempts have shown this to be a significant challenge [89], as can be seen in the non-ideal side walls of a fabricated micro-disk in Figure 6.3(b). A selective wet etch of the AlInAs sacrificial

layer is also seen in this figure. This is done using a concentrated HCl solution (HCL:$H_2O$=3:1).

## 6.2.2   InAs Quantum Dots in Si Cavities

This approach seeks to capitalize on the high $Q$s provided by Si cavities while making use of III-V-based gain media as internal light sources. The basic steps are as follows.

1. Using sputtered alumina as a hard mask [90], a periodic array of pillars is fabricated by e-beam lithography and dry etching on a standard Si substrate. These pillars have diameters in the 50-100 nm range, and heights around 200-300 nm.

2. The sample is cleaned in HF (which etches native $SiO_2$) to remove areas damaged by the dry etch. The sample is then oxidized at a high temperature ($\approx 900\,$C). This step is self-limiting, resulting in a pillar with oxidized surfaces and a pure Si core whose diameter depends on the oxidation temperature and initial pillar diameter.

3. The pillars are mechanically cleaved, leaving behind stumps with the Si core now exposed.

4. To prevent native oxide formation, the sample is immediately placed in a MBE/MOCVD growth chamber, and InAs QDs form preferentially over the crystalline Si areas, as seen in Figure 6.4.

5. Finally, a photonic crystal cavity is fabricated around one of the QDs.

It is proposed that 1D nanobeam cavities be fabricated around QDs, since they offer high $Q$s, even on an oxide substrate. To that end, characterization of empty Si/$SiO_2$ cavities is progressing in parallel with QD growth optimization. Figure 6.5(a) shows an SEM image of a cavity, and Figure 6.5(b) shows a high $Q$ (75,000) mode measured using a tapered-fiber loop.
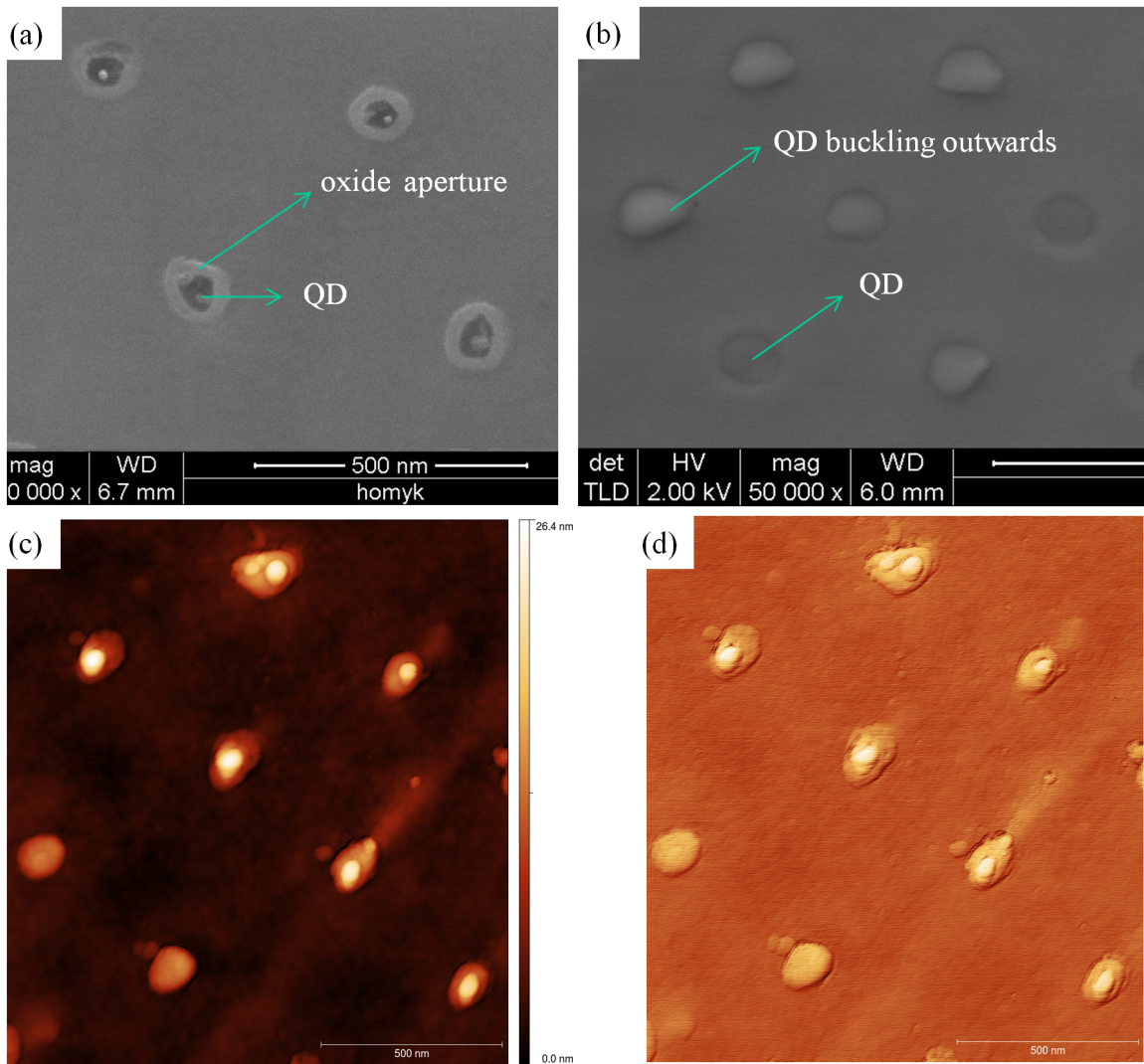
Figure 6.4: (a) & (b) Two different Si substrates imaged after cleavage of pillars and QD growth. Note the difference in QD morphology. (c) AFM scan of sample shown in (a). QD features are $\approx 20$ nm high. (d) Enhanced version of (c) showing texture. (Credits: Andrew Homyk.)
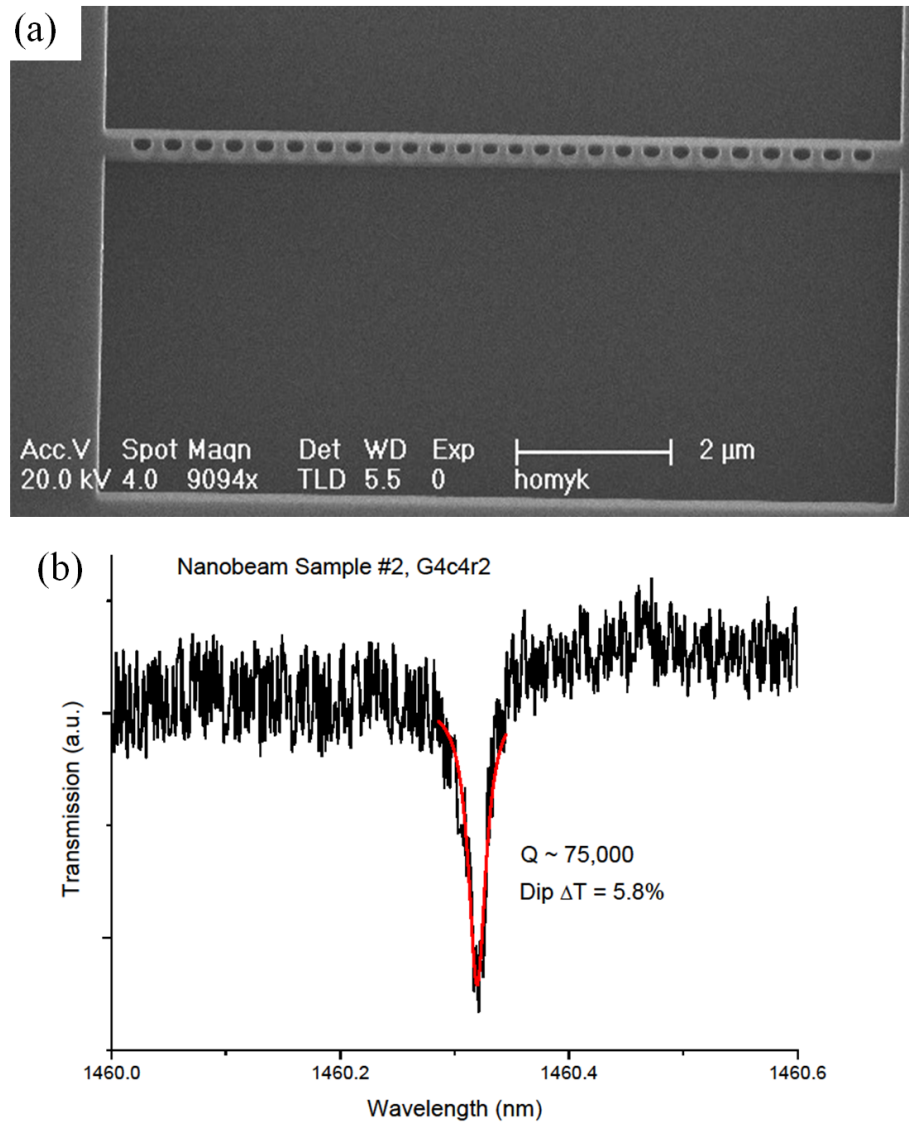
Figure 6.5: (a) 1D nanobeam cavity in Si on $SiO_2$ substrate. (b) Tapered-fiber loop measurement of cavity $Q$ showing fitted Lorentzian. (Credits: (a) Andrew Homyk, (b) Benjamin Richards.)

# Appendix A

# Etching Recipes

## A.1 CAIBE Etching

The following recipe is for etching photonic crystal holes in GaAs with patterned electron-beam resist (PMMA/ZEP) as an etch mask.

- **Chamber preparation**

  Ar, $Cl_2$ lines must be pumped out, and chamber pressure should be in the $5 \times 10^{-7}$–$4 \times 10^{-6}$ torr range. With the flow of Ar gas turned on, the chamber pressure must read $2 \times 10^{-4}$ torr, and this corresponds to an Ar flow rate of 3–4 sccm (standard cubic centimeters per-minute). A $Cl_2$ flow rate of 15 sccm is chosen.

- **Dry etching recipe**

  A typical GaAs etching recipe used in device fabrication has the following parameters.

  Beam voltage (BV): 500–600 V

  Beam current (BC): 10–20 mA

  Discharge voltage (DV): 40 V

  Accelerator voltage (AV): 100 V

  This gives a cathode current (CC) in the 5.7–6.2 A range, a discharge current (DC) of 0.25–0.40 A, an accelerator current (AC) < 0.7 mA, and an etch rate of $\approx 100$ nm/min. It is advisable to run the recipe for 2 minutes without a sample in the chamber for source conditioning. After etching, the gas lines must be pumped out completely, and for the sake of preventing corrosion of the chamber diffusion pump, it is necessary to flow Ar when $Cl_2$ is being purged.

- **CAIBE maintenance**

  It is advisable to refer to the detailed CAIBE manual for troubleshooting. A short summary of important considerations is presented here:

  - A significant deviation of DC or AC from the above listed values usually means that the

source filament needs to be replaced.

– DC and CC should not exceed 3.0 A and 8.0 A, respectively.

– With CC = 1 A, the filament life time expectancy is more than 20 hours.

– When the chamber is opened for filament replacement, it is important to dismantle and clean the ion gun properly. In particular, any dust particles between the narrowly spaced accelerator grids must be carefully removed with the help of a $N_2$ blow-gun for repeatable etching.

## A.2   ICP-RIE Resist Stripping

While the Oxford Instruments inductively coupled plasma–reactive ion etcher (ICP-RIE) 180 is used extensively for etching a wide variety of semiconductors, its use for resist stripping is described here.

- **Chamber preparation**

  The $O_2$/Ar line must be pumped out completely, and the base vacuum should be $< 10^{-5}$ torr.

- **$O_2$ plasma**

  The recipe has the following parameters:

  $O_2$ flow rate: 90 sccm

  Chamber pressure: 10 mTorr

  RF power: 1 W

  ICP power: 600W

  Time: 90 s

  After the actual etch, the gas lines must be pumped out for at least 30 minutes.

- **Operational notes**

  – It is advisable to run this recipe for $\approx$ 5 minutes before loading the sample into the main chamber. Remnant gases sometimes persist in gas lines and can cause undesirable sample etching. A visual indicator of the $O_2$ purity of the plasma is the color—an unchanging pale pink color is indicative of a pure $O_2$ plasma and a conditioned chamber.

  – If difficulty is experienced in striking a plasma, the RF power can be increased in small increments (say, 5 W) till the plasma gets struck. Subsequently, the RF power can be brought down to a lower value. Keeping the RF power low results in a low DC bias. A low DC bias ($< 40$ V) is crucial in preventing surface damage (by means of atomic displacement) in GaAs.

# Appendix B

# Software

## B.1   Computational Electrodynamics

A few operational notes on the use of the eigensolving frequency-domain software (MPB) and the finite-difference time-domain software (MEEP) are presented below.

MPB:

1. It is preferable to have a resolution of the form $2^n$.

2. When simulating 3D structures that have incomplete confinement, i.e.,there are radiation modes, it will happen that guided modes lying close to the light line have errors. Such data is not reliable in its entirety.

3. When computing more than one band, MPB sorts bands in increasing order of frequency at each k-point. This obscures band-crossings, and such bands must be manually re-ordered.

MEEP:

1. Perfectly-matched-layers (PML) layers must be treated most carefully. There should be no structural variation perpendicular to the boundary of the PML. For instance, if the PML layer is applied in the $+x$ direction, $\epsilon(x, y, z)$ must be $x$ independent within the PML. Ideally, there should be no variation in the PML at all.

2. Source location: To successfully find a mode, a source should not be placed at highly symmetric points, rather it should be located near an expected field anti-node. If a particular symmetry is turned on for the simulation, the source must be placed in the negative half space. For instance, if $x$ symmetry is turned on, the source location must have a negative $x$-coordinate.

3. Source Q: Running a broad band source should reveal the different frequencies. From the spacing between the modes, one can calculate the source Q that is needed to excite only a particular mode in a narrow band simulation.

4. The detector need not be confined to the same place as the source location, but should be placed near a field anti-node.

## B.2  Lithography Mask Generation

The process of mask generation for lithography on the EBPG happens in three steps. In the first step, a (self-written) C++ program is used to define individual devices, and control their layout. The program output is fed to a computer-aided-design (CAD) program, which generates a standard-format CAD file. Finally, the CAD file must be fractured at the required EBPG resolution (usually 2.5 nm) and translated to a format that the EBPG can interpret. This program also applies local dose corrections in the form of proximity-error-correction (PEC). In this particular case, a popular semiconductor CAD program called L-EDIT[1] (TannerEDA) is used for the second step, while a program called LayoutBeamer[2] (GenISys) is used for the third step.

---

[1]http://www.tannereda.com/l-edit-pro
[2]http://www.genisys-gmbh.de/index.php?page=products&pro_id=2&pro_type=1

# Bibliography

[1] R. Feynman, *QED: The strange theory of light and matter.* Princeton University Press, 2006.

[2] R. Loudon, *The quantum theory of light.* Oxford University Press, Oxford, 2000.

[3] P. Meystre and M. Sargent, *Elements of Quantum Optics.* Springer Verlag, 2007.

[4] L. Mandel and E. Wolf, *Optical Coherence and Quantum Optics.* Cambridge University Press, 1995.

[5] A. Fox, *Quantum optics: An introduction.* Oxford University Press, USA, 2006.

[6] E. Jaynes and F. Cummings, "Comparison of quantum and semiclassical radiation theories with application to the beam maser," *Proceedings of the IEEE*, vol. 51, no. 1, pp. 89–109, 1963.

[7] E. Purcell, H. Torrey, and R. Pound, "Resonance absorption by nuclear magnetic moments in a solid," *Physical Review*, vol. 69, pp. 37–38, January 1946.

[8] D. Kleppner, "Inhibited spontaneous emission," *Physical Review Letters*, vol. 47, no. 4, pp. 233–236, 1981.

[9] R. Hulet, E. Hilfer, and D. Kleppner, "Inhibited spontaneous emission by a rydberg atom," *Physical Review Letters*, vol. 55, pp. 2137–2140, November 1985.

[10] G. Khitrova, H. M. Gibbs, M. Kira, S. W. Koch, and A. Scherer, "Vacuum Rabi splitting in semiconductors," *Nature Physics*, vol. 2, pp. 81–90, February 2006.

[11] J. P. Reithmaier, G. Sek, A. Löffler, C. Hofmann, S. Kuhn, S. Reitzenstein, L. V. Keldysh, V. D. Kulakovskii, T. L. Reinecke, and A. Forchel, "Strong coupling in a single quantum dot-semiconductor microcavity system," *Nature*, vol. 432, pp. 197–200, November 2004.

[12] E. Peter, P. Senellart, D. Martrou, A. Lemaître, J. Hours, J. Gérard, and J. Bloch, "Exciton-photon strong-coupling regime for a single quantum dot embedded in a microcavity," *Physical Review Letters*, vol. 95, p. 067401, August 2005.

[13] T. Yoshie, A. Scherer, J. Hendrickson, G. Khitrova, H. Gibbs, G. Rupper, C. Ell, O. Shchekin, and D. Deppe, "Vacuum Rabi splitting with a single quantum dot in a photonic crystal nanocavity," *Nature*, vol. 432, no. 7014, pp. 200–203, 2004.

[14] K. Srinivasan and O. Painter, "Linear and nonlinear optical spectroscopy of a strongly coupled microdisk-quantum dot system.," *Nature*, vol. 450, no. 7171, pp. 862–865, 2007.

[15] A. Badolato, K. Hennessy, M. Atature, J. Dreiser, E. Hu, P. Petroff, and A. Imamoglu, "Deterministic coupling of single quantum dots to single nanocavity modes," *Science*, vol. 308, no. 5725, p. 1158, 2005.

[16] K. Hennessy, A. Badolato, M. Winger, D. Gerace, M. Atatüre, S. Gulde, S. Fält, E. L. Hu, and A. Imamolu, "Quantum nature of a strongly coupled single quantum dot-cavity system.," *Nature*, vol. 445, no. 7130, pp. 896–899, 2007.

[17] M. Yamaguchi, T. Asano, K. Kojima, and S. Noda, "Quantum electrodynamics of a nanocavity coupled with exciton complexes in a quantum dot," *Physical Review B*, vol. 80, no. 15, pp. 1–10, 2009.

[18] M. Yamaguchi, T. Asano, and S. Noda, "Photon emission by nanocavity-enhanced quantum anti-Zeno effect in solid-state cavity quantum-electrodynamics.," *Optics Express*, vol. 16, pp. 18067–18081, October 2008.

[19] A. Laucht, N. Hauke, J. Villas-Bôas, F. Hofbauer, G. Böhm, M. Kaniber, and J. Finley, "Dephasing of exciton polaritons in photoexcited InGaAs quantum dots in GaAs nanocavities," *Physical Review Letters*, vol. 103, no. 8, pp. 1–4, 2009.

[20] A. Auffèves, J.-M. Gérard, and J.-P. Poizat, "Pure emitter dephasing: A resource for advanced solid-state single-photon sources," *Physical Review A*, vol. 79, no. 5, pp. 1–5, 2009.

[21] S. Ates, S. Ulrich, A. Ulhaq, S. Reitzenstein, A. Löffler, S. Höfling, A. Forchel, and P. Michler, "Non-resonant dot-cavity coupling and its potential for resonant single-quantum-dot spectroscopy," *Nature Photonics*, vol. 3, no. November, pp. 724–728, 2009.

[22] S. Hughes and P. Yao, "Theory of quantum light emission from a strongly-coupled single quantum dot photonic-crystal cavity system.," *Optics Express*, vol. 17, pp. 3322–3330, March 2009.

[23] F. Laussy, E. del Valle, and C. Tejedor, "Luminescence spectra of quantum dots in microcavities. I. Bosons," *Physical Review B*, vol. 79, no. 23, pp. 1–17, 2009.

[24] M. Winger, T. Volz, G. Tarel, S. Portolan, A. Badolato, K. Hennessy, E. Hu, A. Beveratos, J. Finley, V. Savona, and A. Imamolu, "Explanation of photon correlations in the far-

off-resonance optical emission from a quantum-dot-cavity System," *Physical Review Letters*, vol. 103, no. 20, pp. 11–14, 2009.

[25] J. Joannopoulos, S. Johnson, J. Winn, and R. Meade, *Photonic Crystals: Molding the flow of light.* Princeton Univ Press, 2008.

[26] E. Yablonovitch, "Inhibited spontaneous emission in solid-state physics and electronics," *Physical Review Letters*, vol. 58, no. 20, pp. 2059–2062, 1987.

[27] S. John, "Strong localization of photons in certain disordered dielectric superlattices," *Physical Review Letters*, vol. 58, no. 23, pp. 2486–2489, 1987.

[28] O. Painter, J. Vuckovic, and A. Scherer, "Defect modes of a two-dimensional photonic crystal in an optically thin dielectric slab," *Journal of the Optical Society of America B*, vol. 16, no. 2, pp. 275–285, 1999.

[29] S. Johnson and J. Joannopoulos, "Block-iterative frequency-domain methods for Maxwell's equations in a planewave basis," *Optics Express*, vol. 83, pp. 967–970, 1999.

[30] M. Notomi, K. Yamada, A. Shinya, J. Takahashi, C. Takahashi, and I. Yokohama, "Extremely large group-velocity dispersion of line-defect waveguides in photonic crystal slabs," *Physical Review Letters*, vol. 87, p. 253902, November 2001.

[31] M. Soljacić and J. D. Joannopoulos, "Enhancement of nonlinear effects using photonic crystals," *Nature Materials*, vol. 3, pp. 211–219, April 2004.

[32] S. Johnson, S. Fan, P. Villeneuve, J. Joannopoulos, and L. Kolodziejski, "Guided modes in photonic crystal slabs," *Physical Review B*, vol. 60, no. 8, pp. 5751–5758, 1999.

[33] A. Taflove and S. C. Hagness, *Computational electrodynamics: The finite-difference time-domain method.* Artech House, 2005.

[34] A. Oskooi, D. Roundy, M. Ibanescu, P. Bermel, J. Joannopoulos, and S. Johnson, "MEEP: A flexible free-software package for electromagnetic simulations by the FDTD method," *Computer Physics Communications*, vol. 181, no. 3, pp. 687–702, 2010.

[35] K. S. Yee, "Numerical solution of initial boundary value problems involving Maxwells equations in isotropic media," *IEEE Trans. Antennas Propagat.*, vol. AP-14, no. 5, pp. 302–307, 1966.

[36] D. Shechtman, I. Blech, D. Gratias, and J. Cahn, "Metallic phase with long-range orientational order and no translational symmetry," *Physical Review Letters*, vol. 53, no. 20, pp. 1951–1953, 1984.

[37] P. Lu and P. Steinhardt, "Decagonal and quasi-crystalline tilings in medieval Islamic architecture," *Science*, vol. 315, no. 5815, p. 1106, 2007.

[38] S. Cheng, L. Li, C. Chan, and Z. Zhang, "Defect and transmission properties of two-dimensional quasiperiodic photonic band-gap systems," *Physical Review B*, vol. 59, no. 6, pp. 4091–4099, 1999.

[39] C. Sauvan, P. Lalanne, and J. Hugonin, "Slow-wave effect and mode-profile matching in photonic crystal microcavities," *Physical Review B*, vol. 71, no. 16, pp. 1–4, 2005.

[40] P. Lalanne and J. Hugonin, "Bloch-wave engineering for high-Q, small-V microcavities," *IEEE Journal of Quantum Electronics*, vol. 39, no. 11, pp. 1430–1438, 2003.

[41] C. Sauvan, G. Lecamp, P. Lalanne, and J. Hugonin, "Modal-reflectivity enhancement by geometry tuning in photonic crystal microcavities," *Optics Express*, vol. 13, pp. 245–255, January 2005.

[42] M. Notomi, E. Kuramochi, and H. Taniyama, "Ultrahigh-Q nanocavity with 1D photonic gap.," *Optics Express*, vol. 16, pp. 11095–11102, July 2008.

[43] P. Deotare, M. McCutcheon, I. Frank, M. Khan, and M. Lončar, "High quality factor photonic crystal nanobeam cavities," *Applied Physics Letters*, vol. 94, p. 121106, 2009.

[44] Y. Akahane, T. Asano, B. Song, and S. Noda, "High-Q photonic nanocavity in a two-dimensional photonic crystal," *Nature*, vol. 425, no. 6961, pp. 944–947, 2003.

[45] Y. Akahane, T. Asano, B.-S. Song, and S. Noda, "Fine-tuned high-Q photonic-crystal nanocavity," *Optics Express*, vol. 13, pp. 1202–1214, February 2005.

[46] P. Villeneuve, S. Fan, S. Johnson, and J. Joannopoulos, "Three-dimensional photon confinement in photonic crystals of low-dimensional periodicity," *IEE Proceedings - Optoelectronics*, vol. 145, pp. 384–390, December 1998.

[47] Y. Zhang, M. W. McCutcheon, I. B. Burgess, and M. Loncar, "Ultra-high-Q TE/TM dual-polarized photonic crystal nanocavities," *Optics Letters*, vol. 34, pp. 2694–2696, September 2009.

[48] M. Eichenfield, J. Chan, R. Camacho, K. Vahala, and O. Painter, "Optomechanical crystals," *Nature*, vol. 462, no. 7269, pp. 78–82, 2009.

[49] P. Caroff, C. Platz, O. Dehaese, C. Paranthoen, N. Bertru, A. Lecorre, and S. Loualiche, "Molecular beam epitaxy growth of quantum dot lasers emitting around 1.5 $\mu$m on InP(311)B substrates," *Journal of Crystal Growth*, vol. 278, pp. 329–334, May 2005.

[50] A. Baca and C. Ashby, *Fabrication of GaAs devices.* IET, 2005.

[51] J. Sweet, B. Richards, J. Olitzky, J. Hendrickson, G. Khitrova, H. Gibbs, D. Litvinov, D. Gerthsen, D. Hu, D. Schaadt, M. Wegener, U. Khankhoje, and A. Scherer, "GaAs photonic crystal slab nanocavities: Growth, fabrication, and quality factor," *Photonics and Nanostructures - Fundamentals and Applications*, vol. 8, no. 1, pp. 1–6, 2010.

[52] U. K. Khankhoje, S.-H. Kim, B. C. Richards, J. Hendrickson, J. Sweet, J. D. Olitzky, G. Khitrova, H. M. Gibbs, and A. Scherer, "Modelling and fabrication of GaAs photonic-crystal cavities for cavity quantum electrodynamics," *Nanotechnology*, vol. 21, no. 6, p. 065202, 2010.

[53] C. Michael, K. Srinivasan, T. Johnson, O. Painter, K. Lee, K. Hennessy, H. Kim, and E. Hu, "Wavelength- and material-dependent absorption in GaAs and AlGaAs microcavities," *Applied Physics Letters*, vol. 90, p. 051108, 2007.

[54] J. Hendrickson, B. Richards, J. Sweet, S. Mosor, C. Christenson, D. Lam, G. Khitrova, H. Gibbs, T. Yoshie, A. Scherer, O. Shchekin, and D. Deppe, "Quantum dot photonic-crystal-slab nanocavities: Quality factors and lasing," *Physical Review B*, vol. 72, no. 19, pp. 8–11, 2005.

[55] B. Song, S. Noda, T. Asano, and Y. Akahane, "Ultra-high-Q photonic double-heterostructure nanocavity," *Nature Materials*, vol. 4, no. 3, pp. 207–210, 2005.

[56] E. Kuramochi, M. Notomi, S. Mitsugi, A. Shinya, T. Tanabe, and T. Watanabe, "Ultrahigh-Q photonic crystal nanocavities realized by the local width modulation of a line defect," *Applied Physics Letters*, vol. 88, no. 4, p. 041112, 2006.

[57] D. Englund and J. Vuckovic, "A direct analysis of photonic nanostructures," *Optics Express*, vol. 14, no. 8, pp. 3472–3483, 2006.

[58] M. Kim, J. Yang, Y. Lee, and I. Hwang, "Influence of etching slope on two-dimensional photonic crystal slab resonators," *Korean Physical Society*, vol. 50, no. 4, p. 1027, 2007.

[59] Y. Tanaka, T. Asano, Y. Akahane, B. Song, and S. Noda, "Theoretical investigation of a two-dimensional photonic crystal slab with truncated cone air holes," *Applied Physics Letters*, vol. 82, p. 1661, 2003.

[60] S.-I. Takayama, H. Kitagawa, Y. Tanaka, T. Asano, and S. Noda, "Experimental demonstration of complete photonic band gap in two-dimensional photonic crystal slabs," *Applied Physics Letters*, vol. 87, no. 6, p. 061107, 2005.

[61] F. Wen, S. David, X. Checoury, M. El Kurdi, and P. Boucaud, "Two-dimensional photonic crystals with large complete photonic band gaps in both TE and TM polarizations," *Optics Express*, vol. 16, p. 12278, August 2008.

[62] S. Kim, S. Kim, and Y. Lee, "Vertical beaming of wavelength-scale photonic crystal resonators," *Physical Review B*, vol. 73, no. 23, p. 235117, 2006.

[63] J. Vuckovic, D. Englund, D. Fattal, E. Waks, and Y. Yamamoto, "Generation and manipulation of nonclassical light using photonic crystals," *Physica E: Low-dimensional Systems and Nanostructures*, vol. 32, no. 1-2, pp. 466–470, 2006.

[64] E. A. Hinds, *Cavity quantum electrodynamics, Ed. P. R. Berman.* New York: New York: Academic, 1994.

[65] G. DeSalvo, C. Bozada, J. Ebel, D. Look, J. Barrette, C. Cerny, R. Dettmer, J. Gillespie, C. Havasy, and T. Jenkins, "Wet chemical digital etching of GaAs at room temperature," *Journal of the Electrochemical Society*, vol. 143, no. 11, p. 3652, 1996.

[66] S. Kiravittaya, H. Heidemeyer, and O. Schmidt, "Growth of three-dimensional quantum dot crystals on patterned GaAs (0 0 1) substrates," *Physica E: Low-dimensional Systems and Nanostructures*, vol. 23, no. 3-4, p. 253259, 2004.

[67] A. Faraon, D. Englund, I. Fushman, J. Vuckovic, N. Stoltz, and P. Petroff, "Local quantum dot tuning on photonic crystal chips," *Applied Physics Letters*, vol. 90, no. 21, p. 213110, 2007.

[68] S. Mosor, J. Hendrickson, B. Richards, J. Sweet, G. Khitrova, H. Gibbs, T. Yoshie, A. Scherer, O. Shchekin, and D. Deppe, "Scanning a photonic crystal slab nanocavity by condensation of xenon," *Applied Physics Letters*, vol. 87, p. 141105, 2005.

[69] I. Fushman, D. Englund, A. Faraon, N. Stoltz, P. Petroff, and J. Vuckovic, "Controlled phase shifts with a single quantum dot," *Science*, vol. 320, no. 5877, p. 769, 2008.

[70] A. Högele, S. Seidl, M. Kroner, K. Karrai, R. Warburton, B. Gerardot, and P. Petroff, "Voltage-controlled optics of a quantum dot," *Physical Review Letters*, vol. 93, no. 21, p. 217401, 2004.

[71] B. Richards, J. Hendrickson, J. Sweet, C. Christenson, M. Pajor, D. Lam, G. Khitrova, H. M. Gibbs, A. Scherer, and U. Khankhoje, "Emission characteristics of quantum dots in photonic crystal nanocavities," in *Montana Meeting on Fundamental Optical Processes in Semiconductors*, (Big Sky, Montana), 2007.

[72] M. C. Teich and B. E. A. Saleh, "Observation of sub-Poisson Franck-Hertz light at 2537 nm," *Journal of the Optical Society of America B*, vol. 2, p. 275, February 1985.

[73] P. Michler, A. Kiraz, C. Becher, W. Schoenfeld, P. Petroff, L. Zhang, E. Hu, and A. Imamoglu, "A quantum dot single-photon turnstile device," *Science*, vol. 290, no. 5500, p. 2282, 2000.

[74] Z. Yuan, B. Kardynal, R. Stevenson, A. Shields, C. Lobo, K. Cooper, N. Beattie, D. Ritchie, and M. Pepper, "Electrically driven single-photon source," *Science*, vol. 295, no. 5552, p. 102, 2002.

[75] U. K. Khankhoje, J. Huang, and A. Scherer, "Design and fabrication of an electrically pumped 1D nanobeam laser in GaAs," in *Photonics in Switching*, p. (to appear), Optical Society of America, 2010.

[76] O. Painter, R. Lee, A. Scherer, A. Yariv, J. O'Brien, P. Dapkus, and I. Kim, "Two-dimensional photonic band-gap defect mode laser," *Science*, vol. 284, pp. 1819–1821, June 1999.

[77] H.-G. Park, S.-H. Kim, S.-H. Kwon, Y.-G. Ju, J.-K. Yang, J.-H. Baek, S.-B. Kim, and Y.-H. Lee, "Electrically driven single-cell photonic crystal laser," *Science (New York, N.Y.)*, vol. 305, pp. 1444–1447, September 2004.

[78] S. Kim, Y. Lee, J. Huang, and A. Scherer, "Highly directional emission from ultra-small photonic crystal resonators," in *Proceedings of SPIE* (E. A. Dobisz and L. A. Eldada, eds.), vol. 7402, p. 74020G, 2009.

[79] T. Okumura, M. Kurokawa, M. Shirao, D. Kondo, H. Ito, N. Nishiyama, T. Maruyama, and S. Arai, "Lateral current injection GaInAsP/InP laser on semi-insulating substrate for membrane-based photonic circuits," *Optics Express*, vol. 17, pp. 12564–12570, July 2009.

[80] P. G. Etchegoin, E. C. Le Ru, and M. Meyer, "An analytic model for the optical properties of gold.," *The Journal of Chemical Physics*, vol. 125, no. 16, p. 164705, 2006.

[81] A. Yariv, *Optical Electronics in Modern Communications*. Oxford University Press, USA, 5th ed., 1997.

[82] P. G. Etchegoin, E. C. Le Ru, and M. Meyer, "Erratum: An analytic model for the optical properties of gold [J. Chem. Phys. 125, 164705 (2006)]," *The Journal of Chemical Physics*, vol. 127, no. 18, p. 189901, 2007.

[83] D. Englund, B. Ellis, E. Edwards, T. Sarmiento, J. S. Harris, D. A. B. Miller, and J. Vuckovic, "Electrically controlled modulation in a photonic crystal nanocavity," *Optics Express*, vol. 17, pp. 15409–15419, August 2009.

[84] D. Aspnes, "Recombination at semiconductor surfaces and interfaces," *Surface Science*, vol. 132, no. 1-3, pp. 406–421, 1983.

[85] S. Combrié, A. De Rossi, Q. V. Tran, and H. Benisty, "GaAs photonic crystal cavity with ultrahigh Q: microwatt nonlinearity at 1.55 microm.," *Optics Letters*, vol. 33, pp. 1908–1910, August 2008.

[86] J. Tatebayashi, M. Nishioka, and Y. Arakawa, "Over 1.5 $\mu$m light emission from InAs quantum dots embedded in InGaAs strain-reducing layer grown by metalorganic chemical vapor deposition," *Applied Physics Letters*, vol. 78, no. 22, p. 3469, 2001.

[87] H. Saito, K. Nishi, and S. Sugou, "Influence of GaAs capping on the optical properties of InGaAs/GaAs surface quantum dots with 1.5 $\mu$m emission," *Applied Physics Letters*, vol. 73, no. 19, p. 2742, 1998.

[88] J. I. Davies, A. C. Marshall, M. D. Scott, and R. J. M. Griffiths, "Structural and optical properties of GaAlInAs lattice matched to InP grown by low-pressure metalorganic vapor phase epitaxy," *Applied Physics Letters*, vol. 53, no. 4, p. 276, 1988.

[89] U. Khankhoje, A. Scherer, D. Litvinov, D. Gerthsen, M. Wegener, G. Khitrova, J. Sweet, B. C. Richards, J. Hendrickson, and H. M. Gibbs, "Fabrication and characterization of slab microcavities," in *The 39th Winter Colloquium on the Physics of Quantum Electronics*, (Snowbird, Utah), 2009.

[90] M. Henry, S. Walavalkar, A. Homyk, and A. Scherer, "Alumina etch masks for fabrication of high-aspect-ratio silicon micropillars and nanopillars," *Nanotechnology*, vol. 20, p. 255305, June 2009.